AN INVESTIGATION OF THE REACTING VORTEX STRUCTURES ASSOCIATED WITH PULSE COMBUSTION

Thesis by

Thomas William Zsak

In Partial Fulfillment of the Requirements

for the Degree of

Doctor of Philosophy

California Institute of Technology

Pasadena, California

1993

(Submitted April 13, 1993)

ACKNOWLEDGMENTS

A number of individuals have influenced and assisted the author over the many years that this study has been conducted, and he wishes to express his deep gratitude to them for their support.

First, the author would like to thank Professor Edward Zukoski, his thesis adviser and chairman of his thesis examination committee. The enthusiasm for experimentation which Professor Zukoski possesses along with his unwavering support have aided tremendously to the research program and academic life of the author.

This program would not have been completed had it not been for the efforts of Professor Frank Marble. Numerous discussions with Professor Marble, not only about the present investigation but also on a broad range of topics, proved invigorating and reinstilled an enthusiasm for research which had nearly been lost.

Next, the author wishes to acknowledge the efforts of the other members of his thesis committee, namely Professor Toshi Kubota, Professor Rolf Sabersky, and Professor Gerald Whitham. Their guidance and suggestions are genuinely appreciated and have greatly improved the quality of this work.

A number of fellow students, both past and present, have assisted the author throughout the course of this investigation. Mr. Donald Kendrick and Dr. Richard Chan provided a great deal of assistance in both the experimental and computational efforts of this investigation. Discussions with them as well as with Dr. Michael Chobotov and Dr. Ian Waitz proved to be insightful and beneficial. Dr. James Sterling, who instructed the author on the operation of the laboratory facility, has remained in close contact. The laboratory assistance of Mr. Pierre Jaffre cannot be forgotten.

The faculty members of the Department of Mechanical Engineering and of GALCIT have provided a great deal of insight and influence over the course of this project. The staff members, including Ms. Dorothy Eckerman, Ms. Connie Yehle, and

Ms. Marionne Kirk, have given the author both assistance and support over the years. The author would like to thank the staff of the Aeronautics Shop, especially Mr. George Lundgren and Mr. George Willson, for their much needed expertise and assistance in the construction of the experimental apparatus. Mr. Alan Goudey and Mr. Fred Barnum aided tremendously in the construction of the electronic circuits used in this study. Other staff members of the Caltech campus who deserve recognition are Mr. Nils Asplund and Mr. Don Thomas.

Quite a few people outside of the Caltech community have been supportive as well. Fortunately, there are too many to mention; however, the author would like to acknowledge Ms. Debbie Georgen and Mr. Isaac Curtis, Ms. Monica Venti and Mr. Tracy Ellis, Ms. Lucille Braden and Dr. Gary Gibbs, M.D., Ms. Jacqui Klein and Mr. Bruce Klein, Mr. Jeffrey Mitchell, Mr. Walter Nishikawa, Mr. David Roswell, and Mr. Gene Ursua for their encouragement and patience. The author is also indebted to Professor Norman Chigier and Ms. Eunice Hench of the Mechanical Engineering Department of Carnegie-Mellon University.

Finally, the author wishes to thank his family, especially Mr. Nicholas Olen.

This work was funded by the Air Force Office of Scientific Research, Grant Number 89-0413, under the direction of Dr. Julian Tishkoff.

ABSTRACT

An investigation of the reacting vortex structures associated with pulsating combustion is performed using a laboratory dump combustor in order to gain an understanding of the controlling physical and chemical processes present during the burning of the vortex structures. Stabilized on the lip of a rearward-facing step flame holder, the vortices are shed at acoustic longitudinal modes of the apparatus. In all cases examined, a fuel-rich mixture of methane and air is used, 30% greater than stoichiometric, and the velocity at the dump plane is 21 m/sec. Results are presented for the expansion ratios of 4.0 and 12.0.

A linearized one-dimensional acoustic model is developed to predict the resonant acoustic modes and mode shapes of the system for the two configurations. Heat addition is modeled as a sinusoidally varying volumetric mass source which can be placed at any location within the combustion chamber. Good agreement is found between the natural frequencies predicted by the model and those obtained experimentally under both hot- and cold-flow conditions. The effects of different combustion chamber temperatures on the pressure and velocity responses are revealed as are the effects of placing the heat addition at different axial locations downstream of the dump plane. It is shown that the pressure amplitude spectra for each expansion ratio can be successfully predicted given the relationship between heat release in the chamber and frequency.

The ignition mechanisms of the vortex structures are found to be different for the two chamber configurations, and the bulk of the heat release is shown to occur much closer to the dump plane for the chamber with the smaller expansion ratio. The influence of the lower wall of the combustor on the burning of the structures is shown to be weaker for the chamber with the larger expansion ratio.

The additions of ionization probes and an intensified, charge-injection-device (CID) camera to the experimental program have allowed the burning histories of the shed

vortex structures to be recorded. Capturing an image of the chemiluminescence from the burning of the vortices at nearly the same instant as a shadowgraph image of the density gradients within the chamber completely describes the reacting flow field. Temperature measurements made with fine-wire thermocouples complete the experimental investigation and complement the results obtained above.

TABLE OF CONTENTS

ACKNOWLEDGMENTS	iii
ABSTRACT	v
TABLE OF CONTENTS	vii
LIST OF FIGURES	x
LIST OF TABLES	xv
NOMENCLATURE	xvi
CHAPTER ONE INTRODUCTION	1
1.1 An Introduction to Pulse Combustion	1
1.2 Previous Research	2
1.3 Objectives of Present Study	4
CHAPTER TWO DIAGNOSTICS	6
2.1 Experimental Apparatus	6
2.2 Data Acquisition	8
2.3 Pressure Instrumentation	8
2.4 Hot-Wire Anemometry	9
2.5 Fine-Wire Thermocouples	9
2.5.1 Thermocouple Energy Balance	10
2.5.2 Adiabatic Flame Temperature	11
2.6 Ionization Probes	11
2.7 Intensified Camera/Shadowgraphy	13
2.8 Photomultiplier Tube	16

CHAPTER THREE ONE-DIMENSIONAL ACOUSTIC MODEL 25

3.1 Development of One-Dimensional Model 25

3.2 Effects of Varying the Combustion Chamber Temperature 33

3.2.1 Expansion Ratio of 4.0 33

3.2.2 Expansion Ratio of 12.0 36

3.3 Shapes of Primary Resonant Modes 36

3.3.1 Expansion Ratio of 4.0 36

3.3.2 Expansion Ratio of 12.0 37

3.4 Effects of Varying the Location of Heat Addition 37

3.4.1 Expansion Ratio of 4.0 38

3.4.2 Expansion Ratio of 12.0 38

3.5 Effects of Varying the Temperature Upstream of the Location of Heat Addition 39

3.5.1 Expansion Ratio of 4.0 40

3.5.2 Expansion Ratio of 12.0 40

CHAPTER FOUR EXPERIMENTAL RESULTS 57

4.1 Examination of Pressure and Velocity Data for the Two Expansion Ratios 57

4.2 Comparison of Experimental Spectra with Those Predicted by Acoustic Model 58

4.2.1 Expansion Ratio of 12.0 58

4.2.2 Expansion Ratio of 4.0 64

4.3 Shadowgraph Images 67

4.3.1 Expansion Ratio of 4.0 67

4.3.2 Expansion Ratio of 12.0 68

4.4 Ionization Probe Measurements 71

4.4.1 Expansion Ratio of 4.0 72

4.4.2 Expansion Ratio of 12.0 75

4.5 Chemiluminescence Images 78

4.5.1 Expansion Ratio of 4.0, Short Exposure Images 79

4.5.2 Expansion Ratio of 12.0, Short Exposure Images 82

4.5.3 Expansion Ratio of 4.0, Long Exposure Images 85

4.5.4 Expansion Ratio of 12.0, Long Exposure Images 85

4.6 Temperature Measurements 86

4.6.1 Expansion Ratio of 4.0 87

4.6.2 Expansion Ratio of 12.0 89

CHAPTER FIVE CONCLUDING REMARKS 139

REFERENCES 144

LIST OF FIGURES

Figure 2.1	Overall view of laboratory dump combustor facility.	17
Figure 2.2	Diagram of experimental apparatus.	18
Figure 2.3	Diagram of siren.	19
Figure 2.4	Diagram of hot-wire anemometry circuit.	19
Figure 2.5	Diagram of fine-wire thermocouple probe.	20
Figure 2.6	Fine-wire thermocouple time response curve.	20
Figure 2.7	Adiabatic flame temperature as a function of stoichiometric ratio for methane-air mixtures.	21
Figure 2.8	Diagram of ionization probe and circuit.	21
Figure 2.9	Diagram of charge-injection-device (CID) camera.	22
Figure 2.10	Spectral response of CID camera.	22
Figure 2.11	Circuitry for simultaneous acquisition of shadowgraph/ chemiluminescence images.	23
Figure 2.12	Optical arrangement for simultaneous acquisition of shadowgraph/ chemiluminescence images.	24
Figure 3.1	Schematic of experimental apparatus as used for the one-dimensional acoustic model.	42
Figure 3.2	Pressure amplitude spectra for chamber with expansion ratio of 4.0 under cold- and hot-flow conditions with unit driving at dump plane.	43
Figure 3.3	Pressure amplitude spectra for chamber with expansion ratio of 4.0 with unit driving at dump plane and $0 \leq \omega \leq 600$ Hz for various combustor sonic speeds (*a*) 335 m/sec$\leq a_5 \leq$488 m/sec and (*b*) 549 m/sec$\leq a_5 \leq$750 m/sec.	44
Figure 3.4	Pressure amplitude spectra for chamber with expansion ratio of	

	4.0 with unit driving at dump plane and 100 Hz $\leq \omega \leq$ 300 Hz for various combustor sonic speeds (*a*) 335 m/sec$\leq a_5 \leq$488 m/sec and (*b*) 549 m/sec$\leq a_5 \leq$750 m/sec.	45
Figure 3.5	Velocity amplitude spectrum for chamber with expansion ratio of 4.0 with unit driving at dump plane for hot-flow conditions.	46
Figure 3.6	Pressure amplitude spectra for chamber with expansion ratio of 12.0 under cold- and hot-flow conditions with unit driving at dump plane.	47
Figure 3.7	(*a*) Pressure and (*b*) velocity amplitude spectra for chamber with expansion ratio of 12.0 with unit driving at dump plane for hot-conditions.	48
Figure 3.8	(*a*) Pressure and (*b*) velocity mode shapes of primary acoustic modes of chamber with expansion ratio of 4.0.	49
Figure 3.9	(*a*) Pressure and (*b*) velocity mode shapes of primary acoustic modes of chamber with expansion ratio of 12.0.	50
Figure 3.10	(*a*) Pressure and (*b*) velocity amplitude spectra for chamber with expansion ratio of 4.0 with unit driving at various locations $0 \leq x = LH \leq LC$.	51
Figure 3.11	(*a*) Pressure and (*b*) velocity amplitude spectra for chamber with expansion ratio of 12.0 with unit driving at various locations $0 \leq x = LH \leq LC$.	52
Figure 3.12	(*a*) Pressure and (*b*) velocity amplitudes of primary acoustic modes of chamber with expansion ratio of 4.0 as a function of unit driving location.	53
Figure 3.13	(*a*) Pressure and (*b*) velocity amplitudes of primary acoustic modes of chamber with expansion ratio of 12.0 as a function of unit driving location.	54

Figure 3.14	(*a*) Pressure and (*b*) velocity amplitude spectra for chamber with expansion ratio of 4.0 with unit driving at $LH = 0.2LC$ and various sonic speeds between $0 \le x \le LH$.	55
Figure 3.15	(*a*) Pressure and (*b*) velocity amplitude spectra for chamber with expansion ratio of 12.0 with unit driving at $LH = 0.2LC$ and various sonic speeds between $0 \le x \le LH$.	56
Figure 4.1	Sample raw data traces for (*a*) chamber with expansion ratio of 4.0 and (*b*) chamber with expansion ratio of 12.0.	91
Figure 4.2	Experimental pressure amplitude spectra for (*a*) chamber with expansion ratio of 4.0 and (*b*) chamber with expansion ratio of 12.0.	92
Figure 4.3	Experimental (*a*) velocity and (*b*) total light intensity spectra for chamber with expansion ratio of 12.0.	93
Figure 4.4	Optical arrangement for total light intensity measurement.	94
Figure 4.5	Comparison of (*a*) experimental and (*b*) predicted pressure amplitude spectra for chamber with expansion ratio of 12.0.	95
Figure 4.6	Comparison of (*a*) actual experimental and (*b*) frequency-shifted driving amplitude spectra for chamber with expansion ratio of 12.0.	96
Figure 4.7	Comparison of (*a*) experimental and (*b*) predicted velocity amplitude spectra for chamber with expansion ratio of 12.0.	97
Figure 4.8	Experimental (*a*) velocity and (*b*) total light intensity spectra for chamber with expansion ratio of 4.0.	98
Figure 4.9	Comparison of (*a*) experimental and (*b*) predicted pressure amplitude spectra for chamber with expansion ratio of 4.0.	99
Figure 4.10	Comparison of (*a*) experimental and (*b*) predicted velocity amplitude spectra for chamber with expansion ratio of 4.0.	100

Figure 4.11	High-speed motion picture shadowgraph sequence for chamber with expansion ratio of 4.0.	101
Figure 4.12	High-speed motion picture shadowgraph sequence for chamber with expansion ratio of 12.0	107
Figure 4.13	Schematic diagram of vortex structure.	113
Figure 4.14	Raw data traces of five vortex cycles for chamber with expansion ratio of 12.0.	113
Figure 4.15	Vortex dimensions (*a*) X_w, (*b*) X_l, and (*c*) X_t as functions of time for chamber with expansion ratio of 12.0.	114
Figure 4.16	Shadowgraph and ionization probe data for chamber with expansion ratio of 4.0.	116
Figure 4.17	Data record containing two ionization probe traces for chamber with expansion ratio of 4.0.	117
Figure 4.18.	Shadowgraph and ionization probe data for chamber with expansion ratio of 12.0.	118
Figure 4.19	Ionization probe profiles at various axial positions for chamber with expansion ratio of 12.0 at (*a*) 7 cm, (*b*) 5.7 cm, (*c*) 4.4 cm, (*d*) 3.2 cm, (*e*) 1.9 cm, and (*f*) 0.6 cm above combustor floor.	119
Figure 4.20	Simultaneous shadowgraph/chemiluminescence images at 81 degrees in pressure cycle for chamber with expansion ratio of 4.0.	122
Figure 4.21	Simultaneous shadowgraph/chemiluminescence images at 142 degrees in pressure cycle for chamber with expansion ratio of 4.0.	122
Figure 4.22	Sequence of chemiluminescence images for chamber with expansion ratio of 4.0.	123
Figure 4.23	Average light intensity as a function of axial position for chamber with expansion ratio of 4.0 at various phases of cycle.	124
Figure 4.24	Simultaneous shadowgraph/chemiluminescence images at 203	

	degrees in pressure cycle for chamber with expansion ratio of 12.0.	126
Figure 4.25	Simultaneous shadowgraph/chemiluminescence images at 345 degrees in pressure cycle for chamber with expansion ratio of 12.0.	127
Figure 4.26	Sequence of chemiluminescence images for chamber with expansion ratio of 12.0.	128
Figure 4.27	Average light intensity as a function of axial position for chamber with expansion ratio of 12.0 at various phases of cycle.	129
Figure 4.28	Contour plots of long-time exposure chemiluminescence images for chamber with expansion ratio of 4.0.	132
Figure 4.29	Contour plots of long-time exposure chemiluminescence images for chamber with expansion ratio of 12.0.	133
Figure 4.30	Average light intensity as a function of axial position for the long-time exposure chemiluminescence images for chambers with expansion ratios of 4.0 and 12.0.	134
Figure 4.31	Temperature measurements at various elevations within chamber with expansion ratio of 4.0 at axial positions (*a*) 5 cm and (*b*) 10 cmdownstream of dump plane.	135
Figure 4.32	Temperature measurements at various elevations within chamber with expansion ratio of 12.0 at axial positions (*a*) near dump plane and (*b*) 5 cm,(*c*) 10 cm, (*d*) 15 cm, (*e*) 20 cm, and (*f*) 25 cm downstream of dump plane.	136

LIST OF TABLES

Table 3.1	Comparison of predicted and measured cold-flow resonant modes of chamber with expansion ratio of 4.0 and 100 Hz $\leq \omega \leq$ 600 Hz.	33
Table 4.1	Phase relationships for chamber with expansion ratio of 12.0.	63
Table 4.2	Phase relationships for chamber with expansion ratio of 4.0.	66
Table 5.1	Acoustic resonant modes for chambers with expansion ratios of 4.0 and 12.0.	140

NOMENCLATURE

a_o	Non-perturbed, steady value of sonic speed of gas
$\bar{a}$	Total sonic speed of gas
c	Specific heat of thermocouple material
$D(\omega)$	Magnitude of volumetric mass source at frequency ω
h	Heat transfer coefficient
$I(\omega)$	Amplitude of radiation intensity at frequency ω
LC	Length of combustion chamber
LE	Length of flame holder
LH	Distance from dump plane to location of heat addition
LI	Length of inlet section
LP	Sum of lengths of inlet section and plenum chamber
M_o	Local Mach number, equal to u_o/a_o
$\vec{n}$	Outward-going unit normal vector
p	Pressure perturbation of gas as a function of x and t
p_o	Non-perturbed, steady value of pressure of gas as a function of x and t
$\bar{p}$	Total pressure of gas as a function of x and t, equal to sum of p_o and p
$P(x)$	Pressure of gas as a function of x only
$P^+(\omega)$	Complex coefficient denoting downstream-traveling wave at frequency ω
$P^-(\omega)$	Complex coefficient denoting upstream-traveling wave at frequency ω
R	Radius of thermocouple junction
t	Time
T_g	Temperature of gas
T_w	Temperature of thermocouple wire
u	Velocity perturbation of gas as a function of x and t
u_o	Non-perturbed, steady value of velocity of gas as a function of x and t

$\bar{u}$	Total velocity of gas as a function of x and t, equal to sum of u_o and u
$U(x)$	Velocity of gas as a function of x only
X_l	Distance to leading edge of vortex from dump plane
X_t	Distance to trailing edge of vortex from dump plane
X_w	Width of vortex
x	Position
β	Complex reflectance
β_{exit}	Complex reflectance at combustion chamber exit
β_{plenum}	Complex reflectance at upstream end of plenum chamber
ε	emissivity
γ	Specific heat ratio of gas
ϑ	Phase angle
$\bar{\rho}$	Total density of gas as a function of x and t
ρ_w	Density of thermocouple material
σ	Stefan-Boltzman constant
ω	Frequency
Ψ	Acoustic impedance

Superscript

$(\ )^{combustor}$	Quantities referring to resonant mode of combustion chamber
$(\ )^{highest}$	Quantities referring to highest primary acoustic mode of apparatus
$(\ )^{plenum}$	Quantities referring to resonant mode of plenum chamber

Subscript

$(\ )_1$	Quantities referring to plenum chamber
$(\ )_2$	Quantities referring to inlet section

$( )_3$	Quantities referring to flame holder
$( )_4$	Quantities referring to combustion chamber between $0 \leq x \leq LH$
$( )_5$	Quantities referring to combustion chamber between $LH \leq x \leq LC$
$( )_{2.5\ cm}$	Quantities referring to the 2.5-cm deep chamber, expansion ratio of 4.0
$( )_{7.6\ cm}$	Quantities referring to the 7.6-cm deep chamber, expansion ratio of 12.0
$( )_i$	Quantities referring to light intensity measurements
$( )_p$	Quantities referring to pressure measurements
$( )_v$	Quantities referring to velocity measurements
$( )_{combustion}$	Quantities referring to hot-flow conditions
$( )_{experiment}$	Quantities experimentally determined
$( )_{model}$	Quantities predicted by acoustic model
$( )_{room}$	Quantities referring to cold-flow conditions

Chapter One
Introduction

1.1 An Introduction to Pulse Combustion

Pulsating combustion is an old technology that has recently experienced a revival of sorts in areas such as home heating furnaces, industrial burners, and waste incineration. Combustion in practical burners usually involves vortical structures in the gasdynamic flow. Introduced by the flow path through the burner, the purpose of these structures is to either accelerate the mixing of the fuel and oxidizer components or to enhance the rate of flame spreading through the fuel-oxidizer mixture. Whether these structures arise through the action of natural turbulent shear layers, dilution ports, purposeful generation by specific aerodynamic surfaces, or by other means, they serve as a means of either making the combustion volume more compact or, more generally, controlling the rate of the overall chemical reaction. As a consequence, experimental and analytical investigations into the detailed mechanism of vortex combustion take on great importance.

The creation of stable, reacting vortices is a prohibitively difficult problem, and, as a matter of fact, it is hard to think of a practical burner in which such structures are indeed stable. Fortunately, current optical instrumentation and data acquisition techniques allow the burning mechanism of time-dependent structures to be examined quantitatively as if they were stabilized. It remained, therefore, to find a relatively simple and reliable manner to generate such time-dependent reacting vortices, preferably periodically, so that phase-locked averaging could be employed. The dump combustor, which is notable for its simplicity on one hand and for its propensity to support periodic combustion oscillations on the other, is a likely candidate for time-resolved experiments.

Characterized by a sudden expansion of a fuel-air mixture into a combustion chamber formed by a rearward-facing step, the dump combustor first assumed technological interest through efforts to extend the range of solid rocket missiles by fuel-air combustion subsequent to solid propellant burnout. From the time of its introduction, the dump combustor has exhibited unstable combustion that usually resulted from a coupling between the oscillating pressure and the fluctuating heat release. These oscillations lead to a pulsating operation that typically is detrimental to the performance and life of the engine. Previous studies have examined the excitation of high-frequency transverse acoustic modes and low-frequency longitudinal acoustic modes of the combustion system and have focused on the global aspects or mechanisms of combustion instability.

1.2 Previous Research

Dump combustors exhibit primarily two types of instabilities. High-frequency oscillation, or screech, has been examined by Rogers and Marble (1956) and has been shown to be transverse in nature. These self-excited oscillations are associated with asymmetric vortex shedding from the edges of a V-shaped bluff body flame holder and can be damped with the combustor liner. The novel concept of the work, however, was the idea of a coupling between the acoustic waves and vortex generation with heat release. Abouseif *et al.* (1984) examined the low-frequency instability in a ramjet combustor in which pressure oscillations of large amplitudes were produced that either provided energy to vibratory systems elsewhere in the device or affected the combustion chamber by significantly increasing the heat flux.

Ganji and Sawyer (1980), in a rearward-facing step combustion facility, found that very large vortical structures were periodically formed as the fuel fraction of the combustible mixture was increased towards the stoichiometric value. During the formation of the structures, a large pressure rise was observed in the combustion chamber

causing a reversal in the direction of the incoming flow and leading to a flashback condition.

Work at Caltech has illustrated the importance of the shedding of large vortex structures and their impingement on the lower wall of the combustion chamber on the mixing of reactants with the hot products of combustion during instability. Smith (1985*a*, *b*) explored the effects of acoustic conditions, flow speed, and fuel-air ratio upon the instability mechanism and its development. His findings indicated that in the presence of strong acoustic oscillations which accompany combustion instability, the surging flow into the combustor produces a large vortex that is shed from the lip of the rearward-facing step. The unsteady combustion within the vortex supplies the energy to the acoustic field because the heat release fluctuations and pressure oscillations are in phase from initial vortex formation until the structure impinges against the lower wall.

Sterling (1987*a*, *b*) undertook a more detailed examination of longitudinal mode instabilities associated with premixed combustion and emphasized the mechanism causing the evolution of pressure oscillations during combustion instabilities. He concluded that the phase difference between the oscillating heat release rate and the oscillating pressure in the combustor determines the stability of the combustion process. This phase difference can be sufficiently described by a fluid mechanical mixing time and a chemical reaction time under given flow conditions.

Measurements of the total ignition delay time in a pulse combustor have been made for several chemical kinetic ignition delay times and several fluid dynamic mixing times (Keller *et al.* 1990). It was found that a good approximation to the total ignition delay can be made by simply adding the chemical and mixing delay times. This delay of ignition is an important factor in determining the response of a pulse combustor.

Willis *et al.* (1991) examined the effects of halon addition on the acoustical characteristics of a two-dimensional dump combustor with applications to waste incineration. Laminar flame speeds were reduced and the time lag between pressure

perturbations and heat release oscillations was increased. This resulted in a switch between acoustic modes during operation of the combustor as predicted by a one-dimensional acoustic model.

There is, however, a lack of understanding of the controlling physical and chemical processes present during the burning of vortex structures associated with combustion instabilities. It was recognized that the facility at Caltech constituted a convenient device for investigating the combustion process in vortex structures.

1.3 Objectives of Present Study

The objectives of the present study are threefold. First, the acoustic characteristics of the laboratory dump combustor must be determined for different expansion ratios so that the experimenter is able to differentiate between acoustic and non-acoustic phenomena in the experimental data. Resonant modes, mode shapes, and pressure and velocity amplitude spectra are predicted using one-dimensional acoustic wave theory. Next, the burning histories of the shed vortices are to be recorded. It is clear, for example, that as the expansion ratio of the dump combustor becomes large, the interaction of the burning vortex with the lower wall will be affected. To what extent this interaction will be affected is unclear, and one aim of this investigation is to shed some light on this relationship. Finally, the ignition mechanisms will be examined for different expansion ratios of the combustor. One question that can be asked is "Do vortices ignite in the same manner no matter what may be the configuration of the dump combustor?" This will be answered.

Along with the typical diagnostics of pressure transducers, hot-wire anemometers, photomultipliers, thermocouples, and shadowgraphic flow visualization, two techniques have been added to the experimental program so that the combustion activity within the chamber can be better documented. Ionization probes, primarily used in plasma work, are introduced as a means of identifying and tracking regions of combustion within the

combustion chamber. The second diagnostic technique added to the program is the imaging of the emitted radiation of the burning vortex structures using a solid-state, intensified, charge-injection-device (CID) camera. This non-intrusive flow visualization technique allows the experimenter to obtain very short exposure images of the chemiluminescence of the reacting vortices at preselected instances within their life spans. The resulting images reveal never-before-seen aspects of the burning vortex structures.

The experimental apparatus and diagnostic techniques are described in the following chapter, Chapter Two. Chapter Three details the formulation of a one-dimensional acoustic model used to predict the acoustic resonant modes and corresponding mode shapes of the system. The analysis shows the effects of varying the expansion ratio of the chamber as well as the location of heat addition in and temperature of the chamber. Experimental results are contained in Chapter Four. Here, the section begins with a comparison of the experimentally obtained pressure and velocity spectra with those predicted by the acoustic model for the expansion ratios of 4.0 and 12.0. Next, the flow fields are described using high-speed motion picture and spark shadowgraphy. The ionization probe data are presented as are the chemiluminescence images which detail the ignition and subsequent burning of the shed vortex structures. The chapter concludes with a presentation of temperature measurements made within the chamber for the two expansion ratios. The final chapter, Chapter Five, contains concluding remarks and a summary of the investigation into the reacting vortex structures associated with pulse combustion.

Chapter Two
Diagnostics

2.1 Experimental Apparatus

The laboratory combustor used in the present study differs from that used by Smith (1985*a*, *b*) and Sterling (1987*a*, *b*) in that the depth of the combustion chamber can be varied from 2.5 cm to 15 cm. The previous investigators discussed the design and operation of the facility, and a brief description will be given here.

An overall view of the dump combustor laboratory facility is given in Figure 2.1 showing the blow-down supply system and its numerous regulators and valves. Flow rates are measured at the sonic nozzles located in the air and fuel supply lines. These nozzles are sized so that for equal upstream pressures, a stoichiometric mixture of fuel and air is delivered to the combustor. The fuel and air lines can also be pressurized separately so that a wide range of mixture ratios can be used. These lines converge into a single line and the gases mix as they feed into the large, axisymmetric plenum section. The plenum smoothly converges to a rectangular inlet section at the end of which a flame holder is placed providing 75% blockage of the inlet leading into the combustion chamber.

A schematic of the apparatus focusing on the plenum chamber, inlet section, and combustion chamber is shown in Figure 2.2. The main feature to emphasize here is the ability to change the depth of the combustion chamber from 2.5 cm to 15 cm thereby changing the size of the vortices shed from the lip of the rearward-facing step flame holder as well as the influence of the lower wall on the motion and burning of the vortex structures. The fuel-air mixture enters the apparatus axially through the siren located in the upstream end of the plenum chamber. Consisting of one stationary and one rotating slotted plate (Figure 2.3), the siren provides the pulsating mass flow necessary to initiate

vortex shedding for chamber depths of 10 cm to 15 cm. This is accomplished by fluctuating the mass flow at the natural acoustic mode of the combustion chamber which, together with the coupling of the oscillating pressure and heat release, allows for vortex shedding to commence. For depths less than 10 cm, the instability is self-starting and the siren has no effect on the frequency at which the structures are shed from the lip of the rearward-facing step.

The siren also serves as the upstream end of the plenum chamber. Essentially a plug, it can be moved within the plenum so that the length of the plenum chamber can be varied from 46 cm to 91 cm therefore altering the acoustic response of the system. A smooth contraction from the 15-cm diameter plenum to the 7.6-cm wide by 2.5-cm high inlet section occurs at the downstream end of the plenum over a distance of 25 cm. The rectangular inlet section has a length of 43 cm. At the downstream end of the inlet section, the flow encounters the sudden area expansion of the combustion chamber. Flame holders of various blockage ratios can be placed at the dump plane. Typically, a blockage of 75% over a length of 7.6 cm is used at the end of the inlet section leading into the combustor.

The combustion chamber, 83 cm in length and 7.6 cm wide, has numerous ports for diagnostic access. The top wall has ten access ports for pressure transducers and the lower wall has seven for either ionization or fine-wire thermocouple probes. The face of the step and that of the flame holder have several areas of accessibility for probes as well. The flame holder also has a single port allowing for the placement of a hot-wire anemometer in the cold fluid above the step at a position 3.2 cm upstream of the dump plane. The top, bottom, and side walls of the combustion chamber are water-cooled as is the front face of the step. Side wall panels can be removed and replaced by optical quality Vycor glass windows for optical access when necessary. A spark igniter, located just downstream of the dump plane in the lower wall or placed below the lip of the rearward-facing step flame holder provides the spark which initially ignites the fuel-air mixture. In

all cases presented, a fuel-rich mixture of methane and air, 30% greater than stoichiometric, is used, and the average dump plane velocity is 21 m/sec.

2.2 Data Acquisition

Data acquisition is accomplished using a Zenith ZW-241-82 AT-compatible microcomputer with an A/D board and software provided by RC Electronics. A sampling rate of 80 μsec is typically used and is quite sufficient for the resolution of frequencies below 600 Hz in the signals. Generally, enough data are acquired so that amplitude spectra can be resolved to within 0.75 Hz using a Fast-Fourier-Transform algorithm. With four data acquisition channels in operation and sampling at 80 μsec, a data record 655 msec in length can be obtained. This is approximately equal to the duration of 150 cycles of vortex shedding. The diagnostics used consist of pressure transducers, hot-wire anemometers, fine-wire thermocouples, ionization probes, shadowgraphy, chemiluminescence imaging with a solid-state intensified camera, and a photomultiplier tube. A description of the various techniques will follow.

2.3 Pressure Instrumentation

Following the practice of Smith (1985*a*, *b*) and Sterling (1987*a*, *b*), PCB model 106B piezoelectric pressure transducers are used to measure the fluctuating pressure signals within the combustion chamber. These transducers feature a high signal-to-noise ratio and a fixed voltage sensitivity of 4410 mV/atm. Mounted in the water-cooled access ports on the top wall of the combustor, each transducer is protected from the rapid overpressurization and high temperatures common to the ignition of combustible mixtures by a cavity connected to the chamber by five small holes. Smith (1985*a*, *b*) designed the cavity so that its Helmholtz resonant frequency is approximately equal to 5500 Hz. Consequently, no magnitude or phase correction is needed between the measured and source pressures for disturbances below a value of approximately 800 Hz. Generally, the

pressure signal is used as the reference for all other measurements.

2.4 Hot-Wire Anemometry

A constant temperature hot-wire anemometer (TSI model 1210-T1.5), having a wire diameter of 5 μm, is placed 3.2 cm upstream of the dump plane to measure the velocity and oscillation of the flow during operation. The circuit for the anemometer was constructed by Sobota (1987) at GALCIT and is shown in Figure 2.4.

2.5 Fine-Wire Thermocouples

It is believed that the ignition of the vortex structures and their time histories are highly dependent upon the temperature of the hot products of combustion within the chamber. Temperature profiles within the chamber for the various expansion ratios examined will provide an insight into these areas. For example, is there a quenching effect near the faces of the water-cooled walls? Do the recirculation zones of the various geometries differ greatly in temperature, especially near the lip of the step?

The most suitable technique currently available for the measurement of the local temperature within combusting flows is generally accepted to be the use of unshielded, noble metals, fine-wire thermocouples (Bee'r and Chigier 1983). Because, for this investigation, vortices are shed from the lip of the rearward-facing step flame holder at a frequency of up to 235 Hz, thermocouple time response is critical. Also, disturbance to the flow caused by probe interference must be kept at a minimum. The smallest diameter wires possible, therefore, must be used, yet the thermocouple must be robust enough to withstand the harsh environment of the combustion chamber. For this investigation, R-type thermocouples, consisting of Pt-Pt/13% Rh wires 25μm to 50μm in diameter, were chosen because they exhibit stable characteristics and durability under high temperatures. A sketch of one such thermocouple probe is given in Figure 2.5.

2.5.1 Thermocouple Energy Balance

In general, the probe does not attain the same temperature as the hot, surrounding gas due to the fact that the gas is contained by solid walls which radiatively exchange energy with the probe (Bradley and Matthews 1968). The probe radiates energy to cooler walls and this heat loss must be balanced by convective energy transfer from the gas to the probe. In the absence of any heat release by chemical reaction, therefore, the probe wire is at a lower temperature than the surrounding gas. The value of the temperature difference is called the radiation correction.

For the thermocouple junction, the rate of change of energy must be balanced by the convection and radiation of heat to the surroundings as shown below

$$\rho_w \pi R^2 c \frac{\partial T_w}{\partial t} = 2\pi R\left\{h\left(T_g - T_w\right) - \sigma \varepsilon T_w^4\right\}.$$

Here, ρ_w is density of the thermocouple material, c is the specific heat of the thermocouple material, ε is the emissivity, h is the heat transfer coefficient, R is the radius of the wire junction, and T_g and T_w are the temperatures of the gas and wire, respectively. Experiments conducted by Carbon *et al.* (1950) have shown that heat loss by conduction of heat along the lead wires of the thermocouple was negligible. For this reason, the heat conduction term has been omitted.

Solution of the above equation using a finite-difference scheme yields the time response curve of Figure 2.6. Unfortunately for the 25-μm to 50-μm diameter wires used in this program, the time response of the thermocouple probes is equal to or longer than the period of one cycle of oscillation within the chamber for either of the expansion ratios examined. Temperature fluctuations, therefore, cannot be differentiated, and mean quantities will be reported. The radiation correction is at most 200 °K for the temperature range considered (Bradley and Matthews 1968).

Catalytic effects on the flame by noble metals such as platinum can also be a significant cause of error in thermocouple temperature measurements. These effects can

be eliminated by coating the thermocouple with an insulating material of non-catalytic materials, such as silicon oxides and beryllium/yttrium oxides (Chomiak 1990); however, this leads to a lower frequency response for the probe. Because frequency response is at a premium in this investigation, the thermocouples used are uncoated.

2.5.2 Adiabatic Flame Temperature

For methane-air mixtures, the adiabatic flame temperature varies with stoichiometry as shown in Figure 2.7. This is the maximum temperature that the products of such a reaction can achieve because the combustion process is assumed to take place adiabatically, with neither work nor changes in kinetic or potential energy involved. Any heat transfer from the reacting substances and any incomplete combustion would tend to lower the temperature of the products. For methane-air mixtures at a given pressure and temperature, the maximum adiabatic flame temperature that can be attained is with a mixture ratio that is about 110% of stoichiometric. This temperature is nearly 2220 °K. For an equivalence ratio of 1.30, the value used primarily in this study, the adiabatic flame temperature is about 2040 °K.

2.6 Ionization Probes

In order to facilitate the study of the growth and motion of the shed vortex structures examined in this investigation, it was desired to incorporate into the experimental program a probe able to follow the time-dependent phenomena associated with flame presence. The signal from such a probe could be used as a triggering mechanism for other instruments, or, in the very least, the frequency content of the signal could be used as a marker of combustion activity. One such probe is the ionization probe, because it is sensitive to the ions existing in the reaction zone, where concentrations range from 10^9 to 10^{12} ions/cm^3 for pressures between 2.6×10^{-3} atm to 1.0 atm, and it possesses adequate spatial resolution and time response.

It is well known that the peak ion density closely follows the reaction zone. This is due to the fact that the recombination time of ions, 10^{-7} sec to 10^{-5} sec, is at least one order of magnitude shorter than the time scale of fluctuations in turbulent flames (Chomiak 1972). As a consequence, diagnostic techniques based on ionization are appropriate tools for the examination of flame turbulence (Ventura 1981).

The principle of operation of the ionization probe is fully treated in the literature (Travers and Williams 1965), and a review of the theories supporting the use of the probe was written by Smy (1976). Work using the ionization probe in the study of flame turbulence was first presented by Karlovitz and co-workers (1953) at the Fourth International Combustion Symposium. Their study dealt with a premixed natural gas-air flame and measured the fraction of time the flame spent at the probe position, the most probable position of the combustion wave within the flame brush, and the root-mean-square displacement from this point. They also used the probe to detect 'holes' in the flame which they related to the fullness of the flame. One of the more interesting studies in recent times using the ionization probe was performed by Suzuki *et al.* (1979). Here, two sensors were used in premixed propane-air flames and the signals were cross-correlated to yield the most probable direction and velocity of local flame front movements.

In fact, the vast majority of ionization probe studies have dealt with unconfined, premixed flame situations. Schadow *et al.* (1989) have employed ionization probes in their laboratory dump combustor to determine the effect of pressure oscillation on the temperature fluctuations in the shear layer of the jet issuing from the dump plane. The shed vortices were found to be releasing heat periodically as they traveled downstream. Because this was the sole reference found where ionization probes were incorporated into an experimental investigation regarding the reacting flow within a dump combustor and ionization probes are a very practical means of identifying regions of combustion, it was felt that the addition of the ionization probe to the list of diagnostic tools employed in this

program would be beneficial.

A typical probe used in the present study is illustrated in Figure 2.8. Its components are the sensor of Pt/13% Rh wire, 200 μm in diameter with an exposed length of 1.5 mm, and the ceramic sheath which insulates the wire from the apparatus. A diagram of the complete circuit is also given in the figure. The wires are biased at -27 V to attract the positive ions. Mass spectrometric studies of hydrocarbon flames have revealed that the most dominant ion is H_3O^+ (Calcote 1963) . As one can see, when a region of combustion is present at the probe, the flame acts as a resistor and completes the circuit, enabling a voltage read across the 44 MΩ resistor to be recorded by the data acquisition system. Without the presence of combustion, the circuit is open. Despite the largely qualitative nature of ionization probe measurements, the versatility and simplicity of the method continue to make it a useful tool in combustion studies (Chomiak 1990).

2.7 Intensified Camera/Shadowgraphy

Flow visualization is accomplished through the use of spark and high-speed motion picture shadowgraphy as well as chemiluminescence imaging using a camera equipped with an image intensifier. The flow within the combustion chamber is assumed to be two-dimensional with no spanwise variation. As of yet, there is no method directly available to assess the validity of this assumption; however, the results of Smith (1985*a*, *b*) and Sterling (1987*a*, *b*), in addition to those that will be presented here, lead one to believe that the flow is essentially two-dimensional.

Time-resolved radiation intensity measurements are captured through the use of a General Electric TN2505A solid-state charge injection device (CID) camera (Figure 2.10). The camera divides the field of view into a grid of 360 pixels horizontally by 240 pixels vertically, with pixel values ranging from 0 to 255 depending on the intensity of the light incident on the imager. The spectral response of the camera is shown in Figure 2.11. It should be noted that there is no filtering around the primary bands of chemiluminescent

radiation which are present during the combustion process. These are, namely, C_2 at 516.5 nm, CH at 431.5 nm, and OH at 306.4 nm (Bulewicz 1967). As one can see from the response curve, the camera is detecting the broad-band radiation emitted by the burning vortex structures. These light intensity measurements allow for the estimation of the heat release rate because the local chemiluminescence is proportional to the mass rate of chemical reaction at the point considered (Chomiak 1972).

The principle of using measurements of chemiluminescence as a representation of chemical reaction and heat release is a frequently used technique in combustion flow studies. John and Summerfield (1957) suggest that the radiation and concentrations of these radicals are sensitive functions of fuel type, fuel-air ratio, mixture temperature, and pressure. Therefore, it is said, they can serve as tracers for the more important chemical processes occurring in the flame. Perhaps the first systematic comparisons of visible radiation intensity from laminar and turbulent flames were performed by Clark and Bittker (1954) where for a given mixture ratio, a linear relationship was found between radiation intensity and fuel flow rate. Diederichsen and Gould (1965) have also found the power radiated from a Bunsen-type flame to be proportional to the flow rate.

Currently, a number of pulsating combustion studies, for example Barr *et al.* (1991), Keller *et al.* (1991), Samaniego *et al.* (1991), Tang *et al.* (1991), and Zsak *et al.* (1991), are employing the above principle and are obtaining local heat release ratios by analyzing intensified camera images of spontaneous CH, C_2, and/or OH radical radiation.

For this investigation, a Poynting Products PC-170 programmable frame grabber board with Silicon Video software is used along with the Zenith AT-compatible personal computer for camera operation and image storage. The camera can be operated at a framing rate of up to 60 Hz; however, the normal manner of operation is in a 'snapshot' mode where single images are taken of the combusting flow field. Here, 'short' exposure times of 15 μsec to 60 μsec or 'long' exposures of up to 5 msec are used. A delay circuit, shown in Figure 2.11, has been assembled which triggers the camera at a preselected time

after the positive-going zero-crossing of the signal from the pressure transducer near the dump plane. Once captured, the images are processed using PV-WAVE software. Software has been written in-house for other analyses.

A standard Z-configuration optical arrangement is employed for spark and high-speed cinemagraphic shadowgraphy. The spark shadowgraphs are obtained through the use of a standard spark-gap light source and a Polaroid camera. The exposure time is approximately 2 μsec, and the delay circuit mentioned above is employed so that the photographs are taken at prescribed phases of the pressure cycle. High-speed shadowgraph motion pictures allow the flow field to be continuously recorded. Here, a mercury arc-lamp is used as the continuous light source and a Hycam motion picture camera, having a framing rate of just over 5100 frames per second, records the motion of the flow field on 16 mm film. Event and timing markers are placed on both sides of the film to indicate the beginning of data acquisition and to deduce framing rates.

Use of the CID camera in conjunction with spark shadowgraphy allows for the direct comparison of the shadowgraph with the image of the chemiluminescence. Insertion of a 60% transmittive/40% reflective beam splitter into the optical arrangement (Figure 2.12) enables the CID camera to have the same line of sight as that of the shadowgraph system. The experimental procedure is as follows. At a desired phase in the pressure cycle, a spark shadowgraph is taken. At a time of 15 μsec later, corresponding to a delay of roughly 1.5 degrees in the pressure oscillation cycle, an image of the chemiluminescence is obtained with the CID camera. Generally, the exposure time of this image is 60 μsec. A flame element travels approximately 2.3 pixel widths during this time. That is less than 0.1% of the horizontal field of view. The images obtained by the CID camera, therefore, are sufficiently sharp for analysis.

Qualitatively, the shadowgraph and chemiluminescence images represent the spatial and temporal locations of cold reactants and energy release, respectively. What is unique about the method incorporated in this study is that, for all intents and purposes,

these two images are obtained at the same time leaving no doubt as to the condition of the flow field within the combustor at the time of capture.

2.8 Photomultiplier Tube

Along with the intensified camera, a photomultiplier tube, RCA model 8645, is used to measure the radiation emitted by the combusting vortices at a particular axial location of the chamber, for it has a high frequency response as well as a broad spectral coverage. The field of view consists of a slice of the chamber, 2.5 cm in the vertical direction by 0.6 cm axially, integrated over the entire 7.6-cm width of the combustor. The apparatus is mounted on a traversing mechanism allowing ease of movement, and data are acquired continuously throughout each experimental run. The photomultiplier tube has been employed by Smith (1985*a*, *b*) and Sterling (1987*a*, *b*) in their experimental programs with a great deal of success.

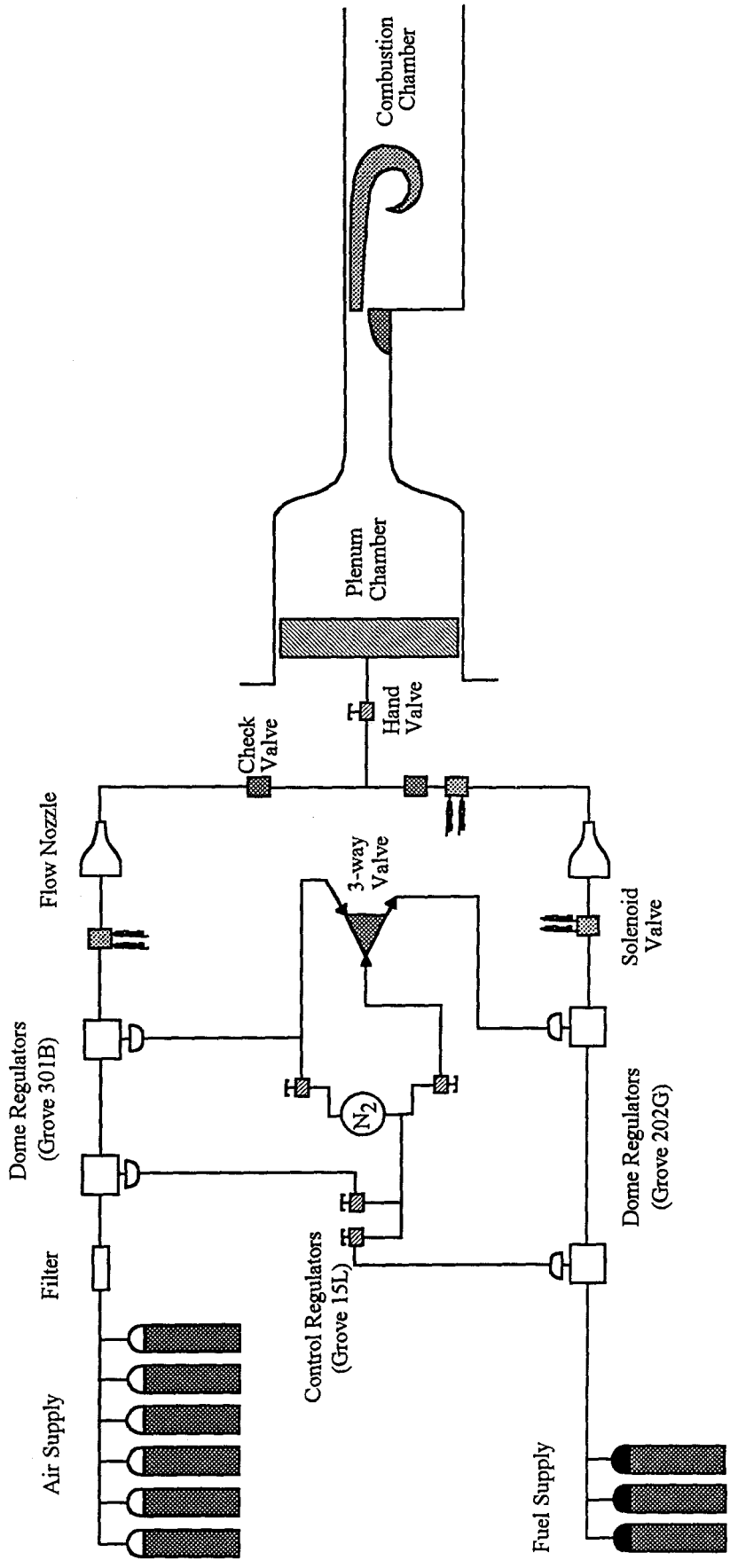

Figure 2.1: Overall view of laboratory dump combustor facility.

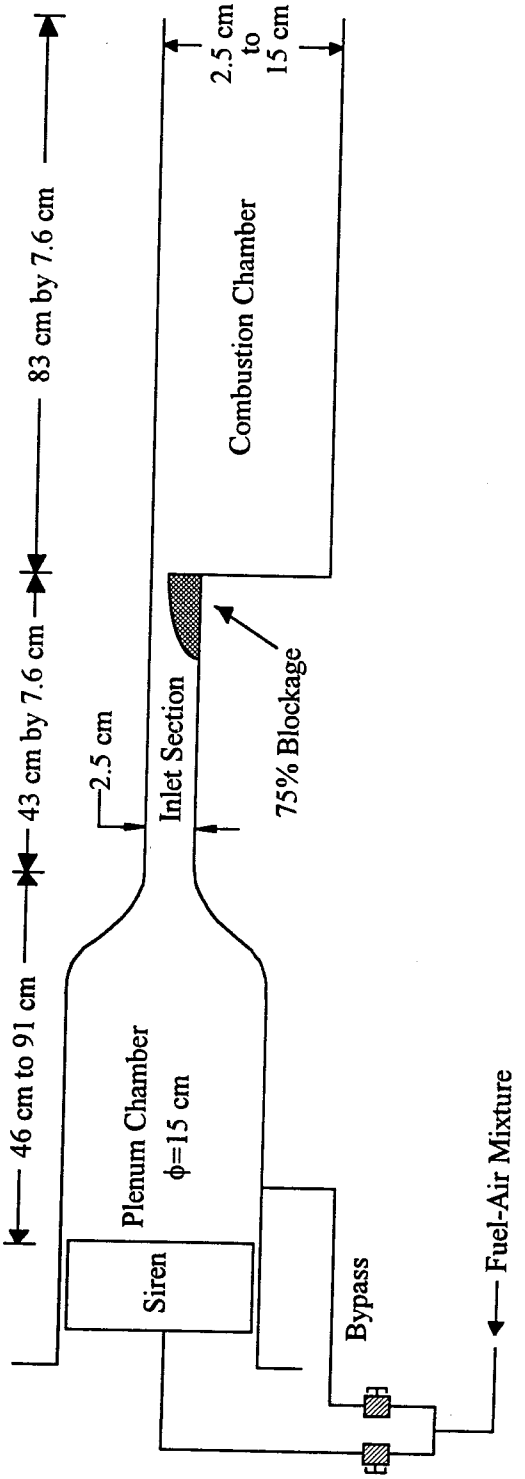

Figure 2.2: Diagram of experimental apparatus.

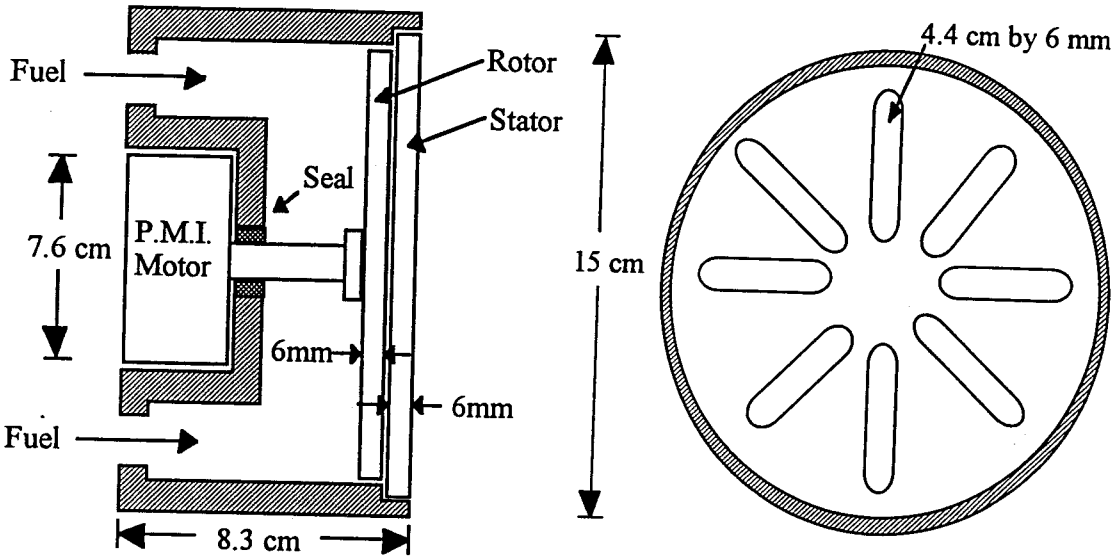

Figure 2.3: Diagram of siren.

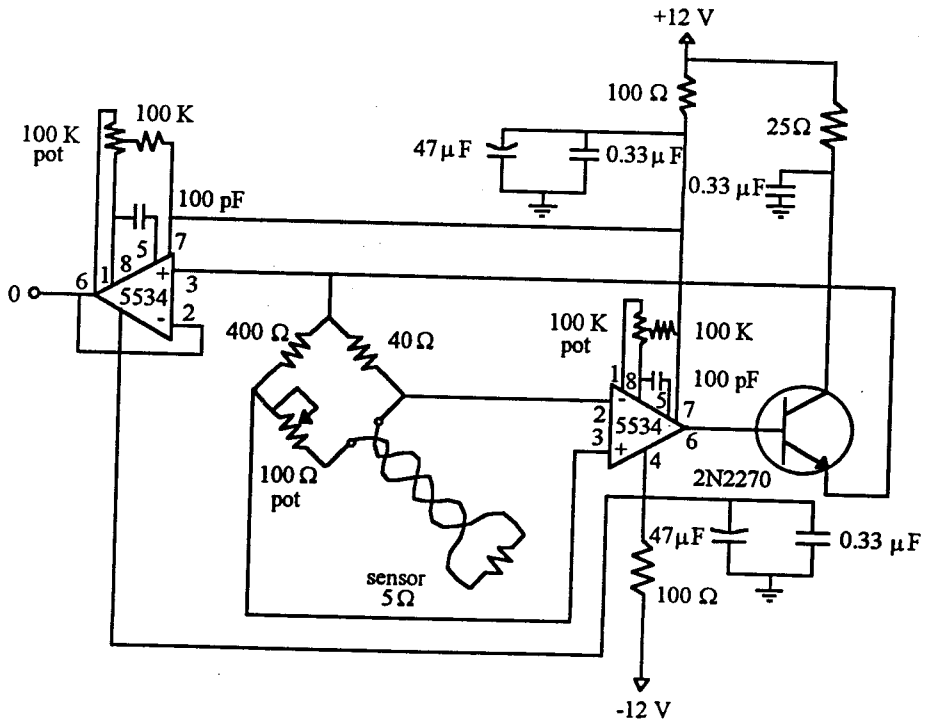

Figure 2.4: Hot-wire anemometer circuitry from Sobota (1987).

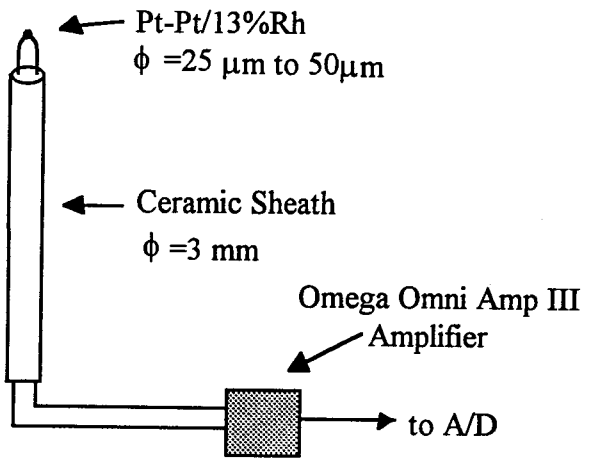

Figure 2.5: Diagram of fine-wire thermocouple probe.

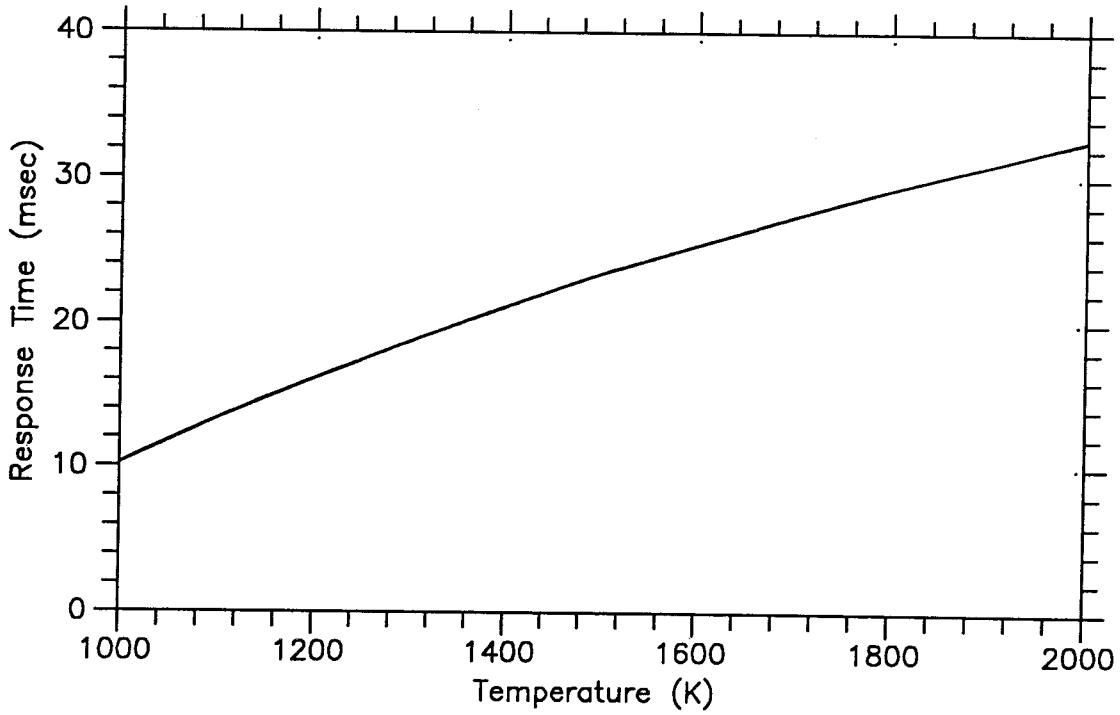

Figure 2.6: Fine-wire thermocouple time response curve.

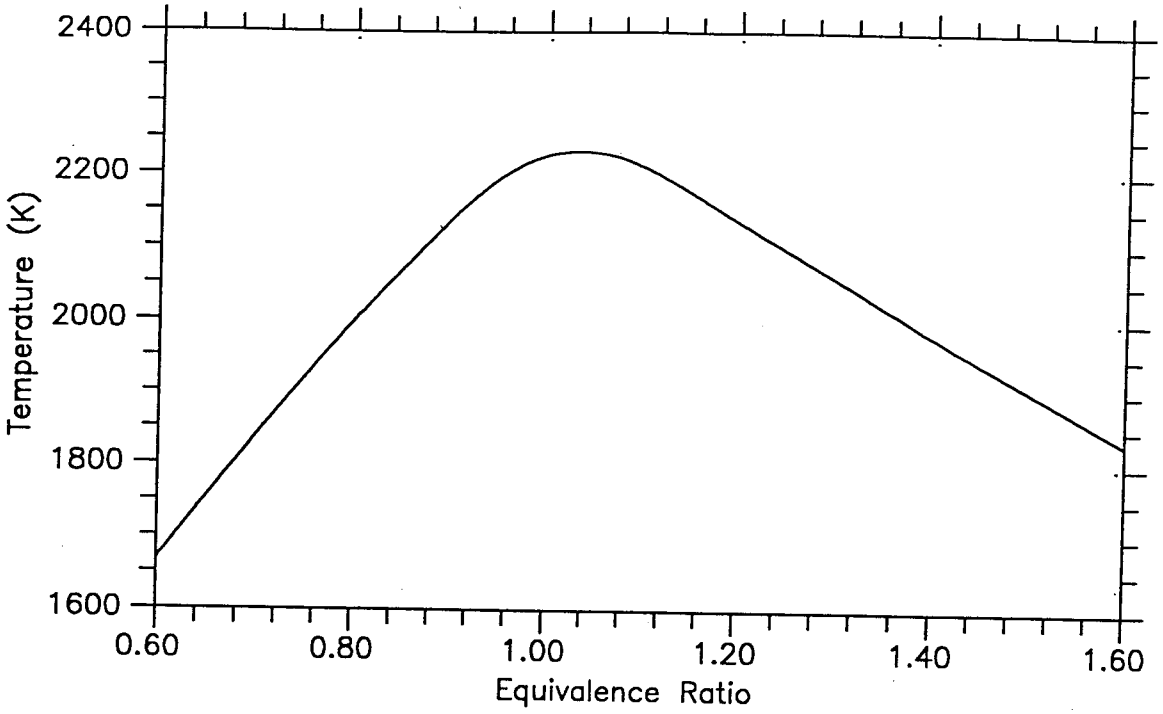

Figure 2.7: Adiabatic flame temperature as a function of equivalence ratio for methane-air mixtures.

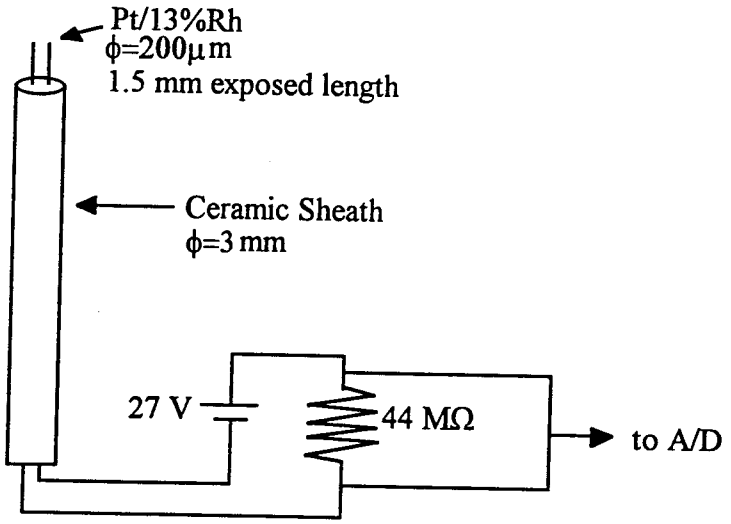

Figure 2.8: Diagram of ionization probe and circuit.

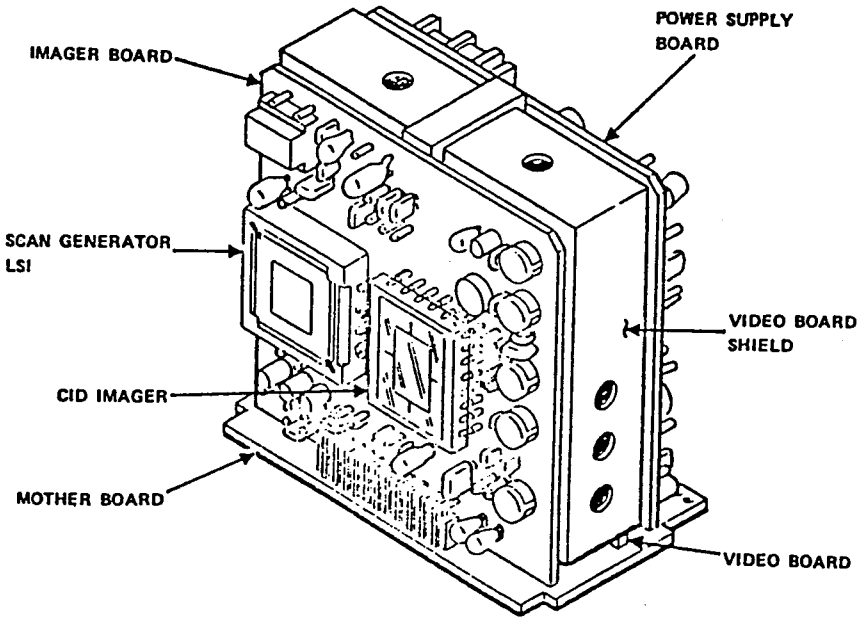

Figure 2.9: Diagram of charge-injection-device (CID) camera from General Electric Company (1983).

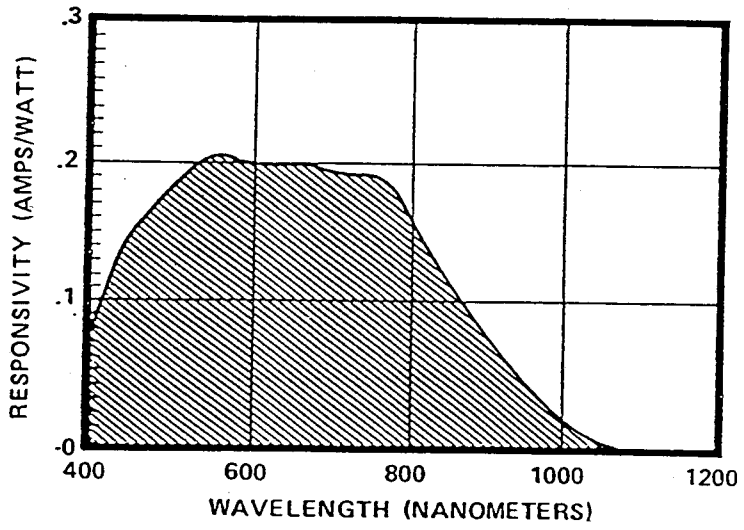

Figure 2.10: Spectral response of CID camera from General Electric Company (1983).

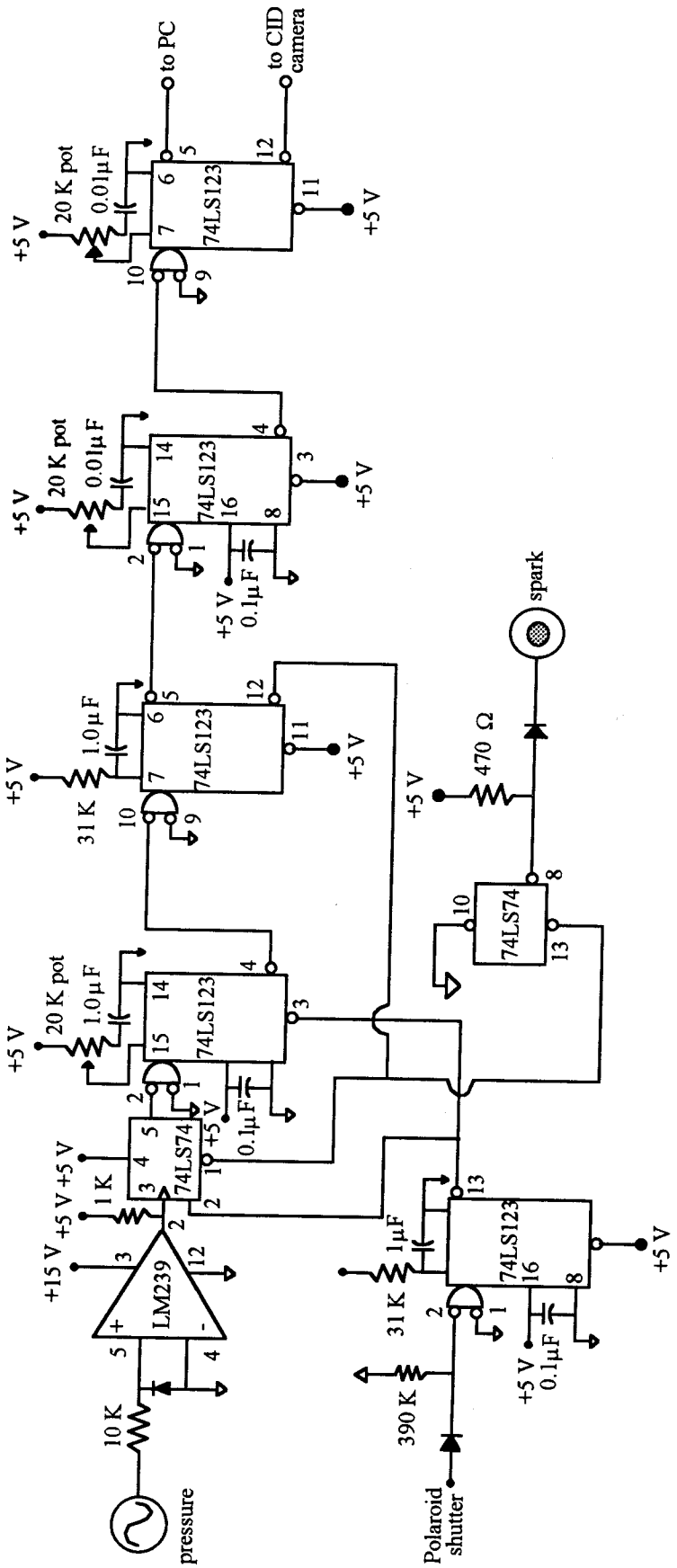

Figure 2.11: Circuitry for simultaneous acquisition of shadowgraph/chemiluminescence images.

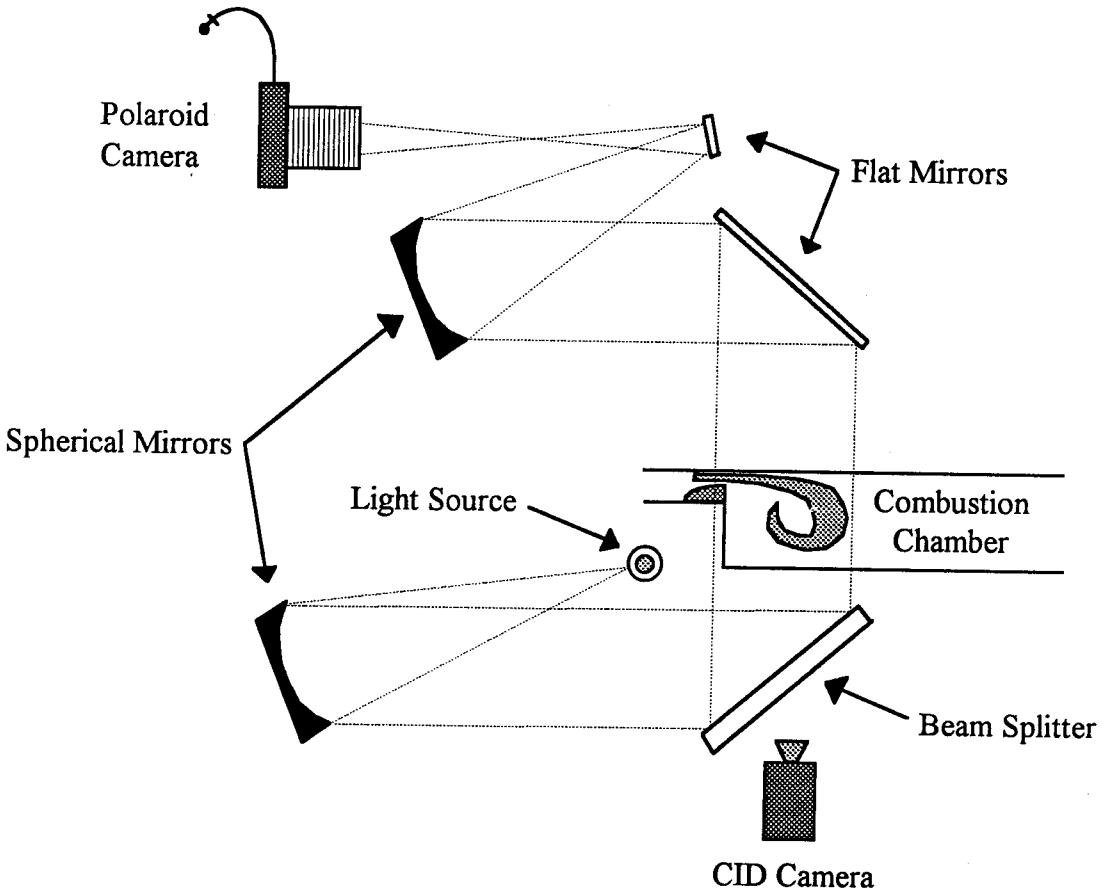

Figure 2.12: Optical arrangement for flow visualization.

Chapter Three
One-Dimensional Acoustic Model

A one-dimensional acoustic model has been developed to predict the resonant acoustic modes and corresponding mode shapes of the laboratory dump combustor. This information is useful in characterizing the behavior of the apparatus and in analyzing the experimental results, for phenomena which are acoustic in nature can be separated from those emanating from other sources.

3.1 Development of One-Dimensional Model

For planar acoustic waves, the conservation equations of mass and momentum can be written as

$$\frac{1}{\bar{\rho}}\frac{\partial \bar{\rho}}{\partial t}+\bar{u}\frac{1}{\bar{\rho}}\frac{\partial \bar{\rho}}{\partial x}+\frac{\partial \bar{u}}{\partial x}=0 \tag{3.1}$$

$$\frac{\partial \bar{u}}{\partial t}+\bar{u}\frac{\partial \bar{u}}{\partial x}+\frac{1}{\bar{\rho}}\frac{\partial \bar{p}}{\partial x}=0, \tag{3.2}$$

where $\bar{\rho}$, $\bar{p}$, and $\bar{u}$ are the density, pressure, and velocity, respectively, of the gas, and x denotes position and t denotes time.

Making use of the isentropic relation

$\bar{p}(\bar{\rho})^{-\gamma}=constant$,

where γ is the ratio of the specific heats, yields the following forms of the above equations

$$\frac{1}{\gamma\,\bar{p}}\frac{\partial \bar{p}}{\partial t}+\bar{u}\frac{1}{\gamma\,\bar{p}}\frac{\partial \bar{p}}{\partial x}+\frac{\partial \bar{u}}{\partial x}=0 \tag{3.3}$$

$$\frac{\partial \bar{u}}{\partial t}+\bar{u}\frac{\partial \bar{u}}{\partial x}+\bar{a}^2\left(\frac{1}{\gamma\,\bar{p}}\frac{\partial \bar{p}}{\partial x}\right)=0, \tag{3.4}$$

where $\bar{a}$ is the sonic speed.

Along with being isentropic, acoustic waves are also of small amplitude. The pressure and velocity variations, therefore, can be linearized by describing each property as the sum of an undisturbed, steady value, denoted by the subscript 'o', and a perturbation value as follows

$$\bar{p} = p_o + p$$
$$\bar{u} = u_o + u$$
$$\bar{a} = a_o.$$

The perturbation of the sonic speed is omitted because it has no bearing on the derivation of the acoustic equations.

Neglecting second-order terms in the fluctuating components, substitution of the linearized variables into equations 3.3 and 3.4, while making use of equations 3.1 and 3.2, gives

$$\left\{\frac{\partial}{\partial t} + a_o(M_o + 1)\frac{\partial}{\partial x}\right\}\left(\frac{u}{a_o} + \frac{p}{\gamma\, p_o}\right) = 0 \qquad (3.5)$$

$$\left\{\frac{\partial}{\partial t} + a_o(M_o - 1)\frac{\partial}{\partial x}\right\}\left(\frac{u}{a_o} - \frac{p}{\gamma\, p_o}\right) = 0, \qquad (3.6)$$

where $M_o = \frac{u_o}{a_o}$, the local Mach number.

If a periodic time disturbance of the form

$$\frac{p}{\gamma\, p_o} = P(x)e^{-i\omega t}$$
$$\frac{u}{a_o} = U(x)e^{-i\omega t},$$

where ω is the frequency, is assumed, substitution into equations 3.5 and 3.6 yields two ordinary differential equations coupling the spatial components $P(x)$ and $U(x)$

$$a_o M_o \frac{d}{dx}U(x) - i\omega U(x) + a_o \frac{d}{dx}P(x) = 0$$

$$a_o \frac{d}{dx}U(x) - i\omega P(x) + a_o M_o \frac{d}{dx}P(x) = 0.$$

Manipulation of the above equations gives the following second-order ordinary differential equation for $U(x)$

$$\frac{ia_o}{\omega}\left(1 - M_o^2\right)\frac{d^2}{dx^2}U(x) - 2M_o \frac{d}{dx}U(x) + \frac{i\omega}{a_o}U(x) = 0.$$

Solving for $U(x)$ and then $P(x)$ gives the following expressions for the fluctuating pressure and velocity

$$\frac{p}{\gamma\, p_o} = e^{-i\omega t}\left\{ P^+ e^{\frac{i\omega x}{a_o\,(M_o+1)}} + P^- e^{\frac{i\omega x}{a_o\,(M_o-1)}} \right\} \qquad (3.7)$$

$$\frac{u}{a_o} = e^{-i\omega t}\left\{ P^+ e^{\frac{i\omega x}{a_o\,(M_o+1)}} - P^- e^{\frac{i\omega x}{a_o\,(M_o-1)}} \right\}, \qquad (3.8)$$

where P^+ and P^- are complex coefficients representing the downstream- and upstream-traveling waves, respectively, computed from the boundary and matching conditions. Equations 3.7 and 3.8 are applicable in each of the regions of the experimental apparatus, and each quantity is in reference to the particular segment in question.

The laboratory dump combustor is modeled as a series of five constant area segments joined by abrupt area changes as shown in Figure 3.1. Because the acoustic wavelengths of the relevant frequencies are long compared to the lengths of the matching regions over which the areas change, the assumption of abrupt area changes is valid. For example, the plenum chamber can be assumed to be an acoustic body with solid boundaries at both ends because its cross-sectional area is much larger than either the sum

of the areas of the fuel supply lines leading into the plenum or the area of the inlet section which connects to the downstream end of the plenum chamber. At resonance, therefore, the solid boundaries act as pressure nodes so that the wavelength of the natural mode of the plenum is equal to twice the length of the plenum chamber, 182 cm. This is over seven times greater than the length of the transition region from the axisymmetric geometry of the plenum chamber to the rectangular cross-section of the inlet section.

The large volume plenum chamber is represented as section *1*, $-(LP+LE) \le x \le -(LI+LE)$, and section *2*, $-(LI+LE) \le x \le -LE$, is the inlet section. The contraction caused by the flame holder at the downstream end of the inlet section is denoted as section *3*, $-LE \le x \le 0$. In all cases, the temperature is taken as $T = T_{room}$ in the area upstream of the dump plane, covering all $x \le 0$. Within this region, $a = a_{room} = 335$ m/sec and $\gamma = \gamma_{room} = 1.4$ as well.

Two segments comprise the combustion chamber. Their boundary is denoted as the position $x = LH$, the location at which an oscillatory volumetric mass source is placed. This driving term, equal to $D(\omega)e^{-i\omega t}$, where $D(\omega)$ is the magnitude of the volumetric mass source introduced at frequency ω, is used to represent the heat addition process. The temperature within section *4*, $0 \le x \le LH$, can be varied; however, it generally has the same value as that in section *5*, $LH \le x \le LC$, where $T = T_{combustion}$, $a = a_{combustion} = 750$ m/sec, and $\gamma = \gamma_{combustion} = 1.3$.

It is desired to use the model to predict the pressure and velocity responses of the apparatus at the dump plane to unit driving over the frequency range $0 \le \omega \le 600$ Hz for different combustion chamber configurations. Using the matching conditions that the pressure is continuous and that the velocity satisfies volumetric continuity at each segment boundary, one can obtain expressions for the coefficients $P^+(\omega)$ and $P^-(\omega)$ in any section in terms of known quantities. Equations 3.7 and 3.8 can then be used to obtain the amplitude spectra of the pressure and velocity within that section. Because pressure measurements are made within the combustion chamber, the coefficients $P_4^+(\omega)$ and

$P_4^-(\omega)$ or $P_5^+(\omega)$ and $P_5^-(\omega)$ are solved for depending on the placement of the volume source. The coefficients $P_3^+(\omega)$ and $P_3^-(\omega)$ are solved for to determine the velocity response above the flame holder because the hot-wire anemometer is placed in the cold flow upstream of the dump plane.

At the area change between the plenum chamber (*1*) and inlet section (*2*), the matching conditions are

pressure:

$$p_1 = p_2$$

$$P_1^+ e^{-\frac{i\omega(LE+LI)}{a_3(M_3+1)}} + P_1^- e^{-\frac{i\omega(LE+LI)}{a_3(M_3-1)}} = P_2^+ e^{-\frac{i\omega(LE+LI)}{a_2(M_2+1)}} + P_2^- e^{-\frac{i\omega(LE+LI)}{a_2(M_2-1)}}$$

continuity:

$$u_1 A_1 = u_2 A_2$$

$$A_1\left\{P_1^+ e^{-\frac{i\omega(LE+LI)}{a_1(M_1+1)}} - P_1^- e^{-\frac{i\omega(LE+LI)}{a_1(M_1-1)}}\right\} =$$

$$A_2\left\{P_2^+ e^{-\frac{i\omega(LE+LI)}{a_2(M_2+1)}} - P_2^- e^{-\frac{i\omega(LE+LI)}{a_2(M_2-1)}}\right\}.$$

Remember that the temperature is constant for all $x \le 0$, meaning that $\gamma_1 = \gamma_2$ and $a_1 = a_2$.

At the area change at $x = -LE$, the matching conditions give

pressure:

$$p_2 = p_3$$

$$P_2^+ e^{-\frac{i\omega LE}{a_2\left(M_2+1\right)}} + P_2^- e^{-\frac{i\omega LE}{a_2\left(M_2-1\right)}} = P_3^+ e^{-\frac{i\omega LE}{a_3\left(M_3+1\right)}} + P_3^- e^{-\frac{i\omega LE}{a_3\left(M_3-1\right)}}$$

continuity:

$$u_2 A_2 = u_3 A_3$$

$$A_2\left\{P_2^+ e^{-\frac{i\omega LE}{a_2\left(M_2+1\right)}} - P_2^- e^{-\frac{i\omega LE}{a_2\left(M_2-1\right)}}\right\} = A_3\left\{P_3^+ e^{-\frac{i\omega LE}{a_3\left(M_3+1\right)}} - P_3^- e^{-\frac{i\omega LE}{a_3\left(M_3-1\right)}}\right\}.$$

At the dump plane, $x = 0$, allowance must be made for the temperature change that occurs as the flow enters the combustion chamber. The constraints are

pressure:

$$p_3 = p_4$$

$$\gamma_3\left\{P_3^+ + P_3^-\right\} = \gamma_4\left\{P_4^+ + P_4^-\right\}$$

continuity:

$$u_3 A_3 = u_4 A_4$$

$$a_3 A_3\left\{P_3^+ - P_3^-\right\} = a_4 A_4\left\{P_4^+ - P_4^-\right\}.$$

At the driving location, there exists the possibility of another temperature difference. The matching conditions at $x = LH$ are

pressure:

$$p_4 = p_5$$

$$\gamma_4\left\{P_4^+ e^{\frac{i\omega LH}{a_4\left(M_4+1\right)}} + P_4^- e^{\frac{i\omega LH}{a_4\left(M_4-1\right)}}\right\} = \gamma_5\left\{P_5^+ e^{\frac{i\omega LH}{a_5\left(M_5+1\right)}} + P_5^+ e^{\frac{i\omega LH}{a_5\left(M_5-1\right)}}\right\}$$

continuity:

$$u_4 A_4 + D(\omega)e^{-i\omega t} = u_5 A_5$$

$$a_4 A_4\left\{P_4^+ e^{\frac{i\omega LH}{a_4\left(M_4+1\right)}} - P_4^- e^{\frac{i\omega LH}{a_4\left(M_4-1\right)}}\right\} + D(\omega) =$$

$$a_5 A_5\left\{P_5^+ e^{\frac{i\omega LH}{a_5\left(M_5+1\right)}} - P_5^- e^{\frac{i\omega LH}{a_5\left(M_5-1\right)}}\right\}.$$

Finally, the boundary conditions at the ends of the apparatus must be defined. The complex reflectance β relating the downstream- and upstream-traveling acoustic waves is given as

$$\beta = \frac{\Psi - 1}{\Psi + 1},$$

where Ψ is the acoustic impedance defined as (Currie 1974)

$$\Psi = \frac{p}{\gamma\ p_o}\frac{a}{\vec{u}\cdot\vec{n}}$$

with $\vec{n}$ being the outward-going unit normal vector.

For the plenum section, the complex reflectance at $x = -(LP + LE)$ is

$$\beta_{plenum} = \frac{P_1^+ e^{-\frac{i\omega(LP+LE)}{a_1(M_1+1)}}}{P_1^- e^{-\frac{i\omega(LP+LE)}{a_1(M_1-1)}}}.$$

The relationship between the coefficients P_1^+ and P_1^- is, therefore

$$P_1^+ = \beta_{plenum} P_1^- e^{-\frac{2i\omega(LP+LE)}{a_1(M_1^2-1)}}.$$

At the combustor exit, the reflectance at $x = LC$ is

$$\beta_{exit} = \frac{P_5^- e^{\frac{i\omega LC}{a_5(M_5-1)}}}{P_5^+ e^{\frac{i\omega LC}{a_5(M_5+1)}}}.$$

The coefficients are related as follows

$$P_5^- = \beta_{exit} P_5^+ e^{-\frac{2i\omega LC}{a_5(M_5^2-1)}}.$$

The reflection coefficient at the upstream end of the apparatus is taken to be ideal because the area of the plenum section is much larger than the sum of the areas of the fuel supply lines leading into the plenum. At the downstream end, experimental correlations of Mahan *et al.* (1984) for the exit impedance of a duct exhausting a hot gas are used. This impedance is dependent upon the temperature of the gas, the acoustic frequency, and the hydraulic radius of the rectangular duct.

3.2 Effects of Varying the Combustion Chamber Temperature

3.2.1 Expansion Ratio of 4.0

The validity of the model can be demonstrated by comparing the predicted acoustic modes with those determined experimentally for cold-flow conditions. For the model, this amounts to setting $T = T_{room}$ in each of the five segments so that $a = a_{room} = 335$ m/sec and $\gamma = \gamma_{room} = 1.4$. Experimentally, the cold-flow resonant modes were determined for the 2.5-cm tall combustor as they were excited by the sound produced as air passed through the siren located in the upstream end of the plenum chamber. The frequency of the siren was altered between 100 Hz and 600 Hz. Four modes were found within this range of frequencies and the results are tabulated in Table 3.1, where a comparison is made of the predicted and measured resonant mode frequencies.

As one can see, the agreement is very satisfactory, and it is felt that the one-dimensional model will predict the acoustic resonant modes of the experimental apparatus under operating conditions quite well.

Table 3.1: A comparison of predicted and measured cold-flow resonant modes for the 2.5-cm deep chamber and 100 Hz$\leq \omega \leq$600 Hz.

FREQ$_{model}$ (Hz)	**FREQ$_{experimental}$ (Hz)**	**% DIFFERENCE**
123	133	8.1
249	274	10.0
334	351	5.1
507	527	3.9

For the case of combustion with unit driving at the dump plane, LH is set equal to zero, and the amplitude spectrum of pressure as determined by the model shows three

primary modes at frequencies of 185 Hz, 222 Hz, and 294 Hz. This is quite a different result from the cold-flow case, and the two spectra are shown graphically in Figure 3.2. Have the cold flow modes shifted to other frequencies or have they been damped or amplified by the heat release and temperature increase of combustion?

To investigate this, the temperature within the combustion chamber was varied from T_{room} to $T_{combustion}$ by varying the sonic speed in the combustor from 335 m/sec to 750 m/sec with $\gamma_{room} = 1.4$ and $\gamma_{combustion} = 1.3$. This amounts to a factor of 5.4 change in temperature, and it is interesting to note the movement of the cold-flow resonant modes to their hot-flow counterparts as the combustion chamber temperature increases.

Figure 3.3*a* shows the effect of increasing the combustor sonic speed from 335 m/sec to 488 m/sec for the 2.5-cm tall combustor over the entire frequency range of interest. The combustor sonic speed is further increased from 549 m/sec to 750 m/sec, and the resulting pressure amplitude spectrum is shown in Figure 3.3*b*. The most interesting activity occurs within the frequency range 100 Hz$\leq \omega \leq$300 Hz, and the results presented in Figures 3.3*a* and *b* are reproduced in Figure 3.4 *a* and *b*, respectively, with an emphasis on this range.

The lowest cold-flow resonant mode, which is related to the entire length of the experimental apparatus, is at a frequency of 15 Hz. This value changes to 17 Hz as the combustor sonic speed is increased to 488 m/sec. At a combustor sonic speed of 549 m/sec, the lowest frequency mode is 18 Hz and becomes 19 Hz at the final combustor sonic speed of 750 m/sec.

The cold-flow mode at 123 Hz, which eventually becomes the hot-flow mode at 185 Hz, moves upward to 129 Hz, 142 Hz, and 154 Hz for the sonic speeds of 366 m/sec, 427 m/sec, and 488 m/sec, respectively, as shown in Figure 3.4*a*. Figure 3.4*b* shows that further increasing the combustor sonic speed to 549 m/sec, 610 m/sec, and 671 m/sec shifts this mode to 164 Hz, 173 Hz, and 180 Hz, respectively. Finally, at a sonic speed of 750 m/sec, the resonant acoustic mode which initially had the value of 123 Hz settles into

its hot-flow value of 185 Hz. The amplitudes of the peaks are shown to decrease as the combustor sonic speed, *i.e.*, temperature, is increased. The damping in the system is evidently increasing with increasing combustor temperature and, in fact, the reflection coefficient at the exit of the combustion chamber moves further away from an ideal value of -1.0 as the temperature of the exhaust gas increases.

The hot-flow acoustic mode at 222 Hz begins as a very small response at 194 Hz under cold conditions. The response increases in amplitude as the peak shifts up the frequency scale to 195 Hz, 198 Hz, and 200 Hz as the temperature in the chamber is increased as given in Figure 3.4*a*. This mode, as shown in Figure 3.4*b*, moves from 202 Hz at a sonic speed of 549 m/sec to 206 Hz and 212 Hz at sonic speeds of 610 m/sec and 671 m/sec, respectively. At the final sonic speed of 750 m/sec, the resonant mode reaches a value of 222 Hz. One notes that the response of this mode increases in amplitude as the sonic speed is increased to 488 m/sec and then decreases in amplitude as the temperature within the combustion chamber is increased further.

The primary acoustic mode having the highest frequency under hot-flow conditions is predicted to be at 294 Hz for the 2.5-cm deep chamber. The origin of this mode is the 249 Hz cold-flow mode. As the temperature in the combustion chamber is increased, Figure 3.4*a* shows that this mode shifts to 256 Hz and to 265 Hz as the sonic speed changes from 366 m/sec to 427 m/sec, respectively. The amplitude of the response is decreasing rapidly so that at a frequency of 272 Hz, corresponding to a combustor sonic speed of 488 m/sec, the response is but a fraction of that under cold-flow conditions. Figure 3.4*b* shows that the natural mode occurs at frequencies of 277 Hz, 281 Hz, and 286 Hz for combustor sonic speeds of 549 m/sec, 610 m/sec, and 671 m/sec, respectively, before reaching the value of 294 Hz at a sonic speed of 750 m/sec.

The velocity amplitude spectrum for the 2.5-cm deep chamber under hot-flow conditions with unit driving at the dump plane is given in Figure 3.5*b*. The corresponding pressure amplitude spectrum is repeated in Figure 3.5*a*.

3.2.2 Expansion Ratio of 12.0

The primary resonant modes of the larger, 7.6-cm deep combustion chamber having an expansion ratio of 12.0 are determined by the acoustic model to occur at frequencies of 110 Hz, 258 Hz, 316 Hz, and 501 Hz under cold-flow conditions. The cold-flow resonant modes were not determined experimentally for this chamber configuration. Under hot-flow conditions, the acoustic modes are predicted to occur at frequencies of 190 Hz, 222 Hz, and 278 Hz. The pressure amplitude spectra for the two flow conditions are plotted in Figure 3.6.

For hot-flow conditions, increasing the cross-sectional area of the combustion chamber by a factor of 3.0 has lead to a 2.6% increase in the frequency of the lowest primary acoustic mode and a 5.4% reduction in the frequency of the highest resonant mode as compared to the values of 185 Hz and 294 Hz, respectively, for the chamber with an expansion ratio of 4.0. Interestingly, the mode at 222 Hz has remained the same. The amplitude spectra of pressure and velocity for unit driving at the dump plane of the 7.6-cm deep chamber are given in Figures 3.7*a* and *b*, respectively.

3.3 Shapes of Primary Resonant Modes

3.3.1 Expansion Ratio of 4.0

The one-dimensional model is also able to give the shape of a particular pressure and velocity mode. The pressure and velocity mode shapes of the three primary acoustic modes of 185 Hz, 222 Hz, and 294 Hz are given in Figures 3.8*a* and *b*, respectively, for the 2.5-cm deep chamber where the dump plane is located at $x = 0$. The plenum chamber comprises the region -134 cm$\leq x \leq$-51 cm. The inlet section is between -51 cm$\leq x \leq$-7.6 cm, and the flame holder is at -7.6 cm$\leq x \leq$0. The combustion chamber occupies $0 \leq x \leq 83$ cm. It can be seen that the mode at 185 Hz has a wavelength which is approximately twice as long as the length of the plenum chamber. Because the cross-sectional area of the plenum is large compared to that of the inlet section, it can be

thought of having closed conditions at either end. The ends, therefore, are pressure antinodes and velocity nodes as depicted in Figures 3.8*a* and *b*, respectively. In fact, dividing the sonic speed of 335 m/sec by twice the plenum length gives a frequency of 201 Hz, a difference of 8.6% from the 185-Hz value given by the acoustic model. This mode will be referred to as the 'plenum mode' at times in the following text.

The combustion chamber, whose cross-sectional area is much larger than that of the flame holder segment, behaves as if it had closed-open end conditions as does an organ pipe. Its natural frequency, therefore, has a wavelength which is four times the length of the combustion chamber and is equal to 226 Hz. This value is merely 1.8% different from the acoustic mode of 222 Hz predicted by the one-dimensional model. Henceforth, this mode will be referred to as the 'organ pipe mode'.

One is unable to assign a particular segment of the apparatus to the 294 Hz acoustic mode.

3.3.2 Expansion Ratio of 12.0

Pressure and velocity mode shapes of the three primary acoustic modes at frequencies of 190 Hz, 222 Hz, and 278 Hz for the 7.6-cm deep chamber are given in Figures 3.9*a* and *b*, respectively. Because the lengths of the components of the apparatus have not changed, the coordinates given above for the boundaries of each segment remain the same. Again, it is noted that the 'plenum mode' at 190 Hz has a wavelength which is nearly twice as long as the plenum chamber, and the wavelength of the 'organ pipe mode' of the combustion chamber at 278 Hz is approximately four times as long as the chamber.

3.4 Effects of Varying the Location of Heat Addition

The location of the driving or mass source within the combustor was found to have a negligible effect on the values of the resonant frequencies for either the 2.5-cm or 7.6-cm tall combustion chamber configurations under hot-flow conditions. Figures 3.10*a* and

b show the amplitude spectra of pressure and velocity, respectively, for the 2.5-cm deep combustion chamber as the location of the mass source is varied from $0 \leq x = LH \leq LC$. The corresponding spectra for the 7.6-cm deep chamber are shown in Figure 3.11*a* and *b*, respectively.

To obtain a better understanding of how the amplitudes of the resonant modes change as the location of the driving varies, Figures 3.12 and 3.13 show the variation of pressure and velocity amplitudes with location *LH/LC* for the 2.5-cm and 7.6-cm tall combustors respectively.

3.4.1 Expansion Ratio of 4.0

For the smaller depth chamber, Figure 3.12*a* shows that the pressure responses of the 185-Hz and 222-Hz modes falls steadily to nearly zero as the driving location moves downstream of the dump plane. The response of the 294 Hz mode actually increases in magnitude initially, reaching its maximum value at roughly $LH \cong 0.3LC$, then falls off to zero with the other modes.

The velocity response in the region of the flame holder, shown in Figure 3.12*b*, reveals that the amplitude of the response of the 185-Hz mode steadily falls to zero as did the corresponding pressure response. The 222-Hz mode is rather unaffected by the position of the driving source within the chamber. Its curve is nearly flat, although it does slowly fall to zero. Once again, the response of the 294-Hz mode reaches a maximum at $LH \cong 0.3LC$. At $LH \cong 0.44LC$, the velocity responses of the 185 Hz and 294 Hz modes are equal, and the amplitude of the 294 Hz mode is greater than that of the 185 Hz mode as *LH* approaches *LC*.

3.4.2 Expansion Ratio of 12.0

The responses of the three primary acoustic modes of the 7.6-cm deep chamber behave in much the same way as those for the smaller depth duct. Figure 3.13*a* shows

that the pressure responses of the modes in the combustion chamber steadily fall to zero as the driving is placed further from the dump plane. As was the case previously, the amplitude of the response of the 'plenum mode' is greater than that of the 'organ pipe mode' which, in turn, is greater than that of the highest frequency mode. The 278-Hz mode is shown to increase in magnitude until $LH \cong 0.3LC$ then falls to zero as the driving location reaches the end of the combustion chamber.

The velocity responses of Figure 3.13*b* indicate once again that the combustion chamber mode at 222 Hz is relatively unaffected by the location of the driving in the chamber. The two other modes have the same relationship as they had for the 2.5-cm deep chamber examined above. The response of the 'plenum mode' is greater than that of the 278-Hz mode until the driving occurs at $LH \cong 0.42LC$ where the two responses are equal. For locations of driving which are greater than this position, the amplitude of the response of the 278-Hz mode is greater than that of the 190-Hz mode as they fall to zero.

These plots for the two chambers show that even if the heat source was not compact, but rather, distributed, the result would be a linear sum of a number of compact sources.

3.5 Effects of Varying the Temperature Upstream of the Location of Heat Addition

Finally, the effect of varying the temperature in region *4*, $0 \le x \le LH$ is examined by changing the sonic speed in the region from cold- to hot-flow conditions while maintaining the driving at $LH = 0.2LC$. This driving location was chosen after an examination of the experimental results showed that the bulk of the heat release occurs approximately 15 cm downstream of the dump plane when the expansion ratio of the combustor is equal to 12.0. The pressure and velocity spectra for the 2.5-cm deep combustion chamber are shown in Figures 3.14*a*, and *b*, respectively, and those for the larger chamber are given in Figure 3.15*a*, and *b*, respectively. The sonic speeds between

the dump plane and the driving location are 335 m/sec, which is the cold-flow condition, 457 m/sec, 610 m/sec, and 750 m/sec, the hot-flow condition.

3.5.1 Expansion Ratio of 4.0

Examining the pressure amplitude spectrum for the 2.5-cm deep duct shown in Figure 3.14*a*, one sees that the frequencies of the resonant modes are lowered by only a few hertz from their hot-flow values when cold conditions exist in the region $0 \le x \le LH = 0.2LC$. This is the worst case. The 'plenum mode' drops from 185 Hz to 182 Hz, a change of 1.6%, and the 'organ pipe mode' of the combustor becomes 221 Hz, a drop of only 1 Hz or 0.5% from the value of 222 Hz attained when the driving occurs at the dump plane. The greatest effect is shown in the highest of the three primary resonant modes where the frequency falls from 294 Hz to 287 Hz, a 2.4% change. This mode is also seen to be the only one of the three whose response increases in magnitude as the temperature within the region between the dump plane and the driving location approaches that of the rest of the combustion chamber. The responses of the two other primary modes decrease in amplitude as the temperature reaches that of the rest of the duct.

3.5.2 Expansion Ratio of 12.0

For the 7.6-cm deep chamber, Figure 3.15*a* shows that the pressure responses of the plenum and combustor modes also decrease as the temperature in the region $0 \le x \le LH = 0.2LC$ approaches that of the rest of the combustion chamber; however, their frequencies remain nearly the same. In the worst case, the 'plenum mode' drops from 190 Hz to 188 Hz, a change of 1.1%, and the 'organ pipe mode' of the combustor falls from 222 Hz to 220 Hz, only a 0.9% difference. The frequency of the highest primary mode drops 0.7% to 276 Hz from 278 Hz.

The resonant modes of the laboratory apparatus have been predicted for two expansion ratios, and it has been shown how the modes change from cold- to hot-flow conditions for the 2.5-cm deep chamber. The location of the driving was demonstrated to have little effect on the values of the natural frequencies of the system under either combustor configuration. Finally, it has been shown that the resonant modes are essentially unchanged when the location of the heat source is placed just downstream of the dump plane and the temperature of the region between the dump plane and the location of heat addition is varied from cold- to hot-flow conditions. In the following chapter, the results from the one-dimensional acoustic model will be compared to those obtained experimentally for the two expansion ratios of 4.0 and 12.0.

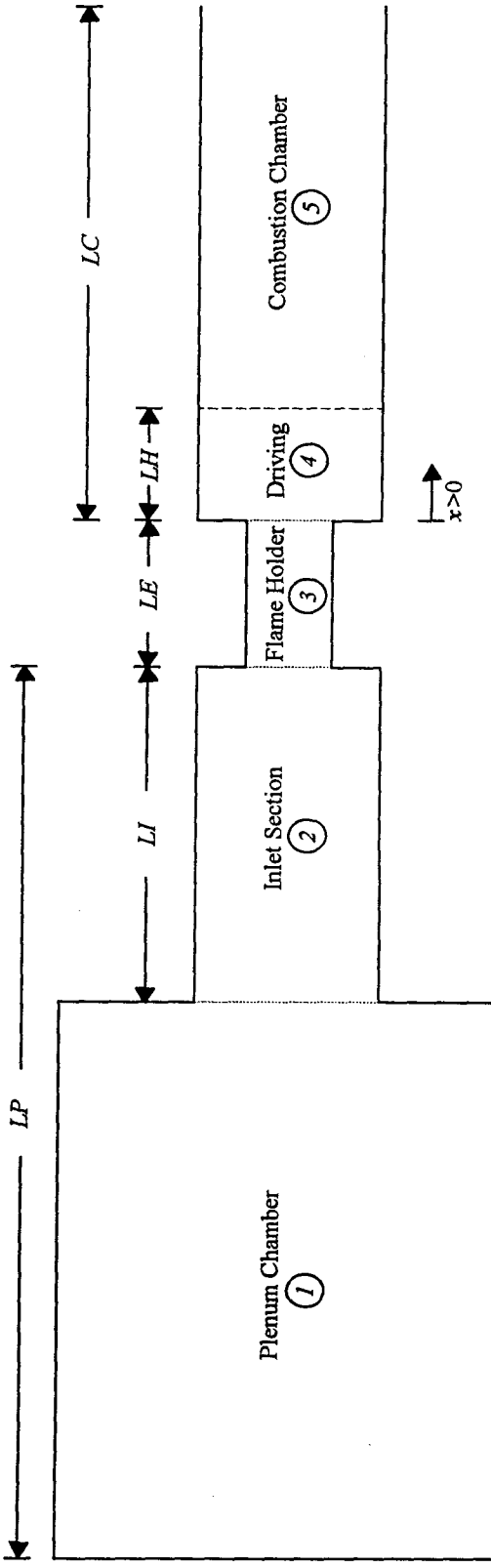

Figure 3.1: Schematic of experimental apparatus as used for the one-dimensional acoustic model.

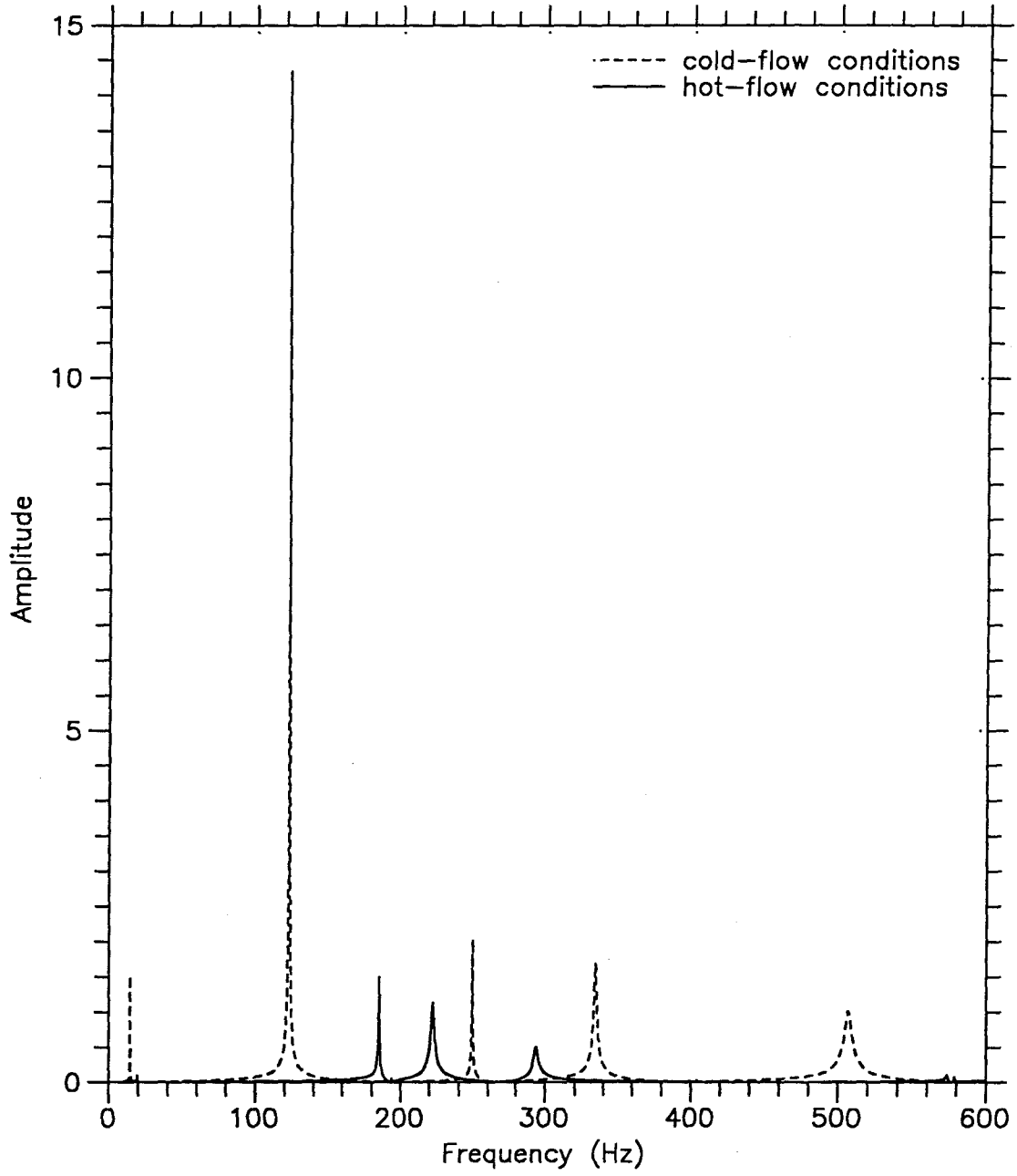

Figure 3.2: Pressure amplitude spectra for chamber with expansion ratio of 4.0 under cold- and hot-flow conditions with unit driving at dump plane.

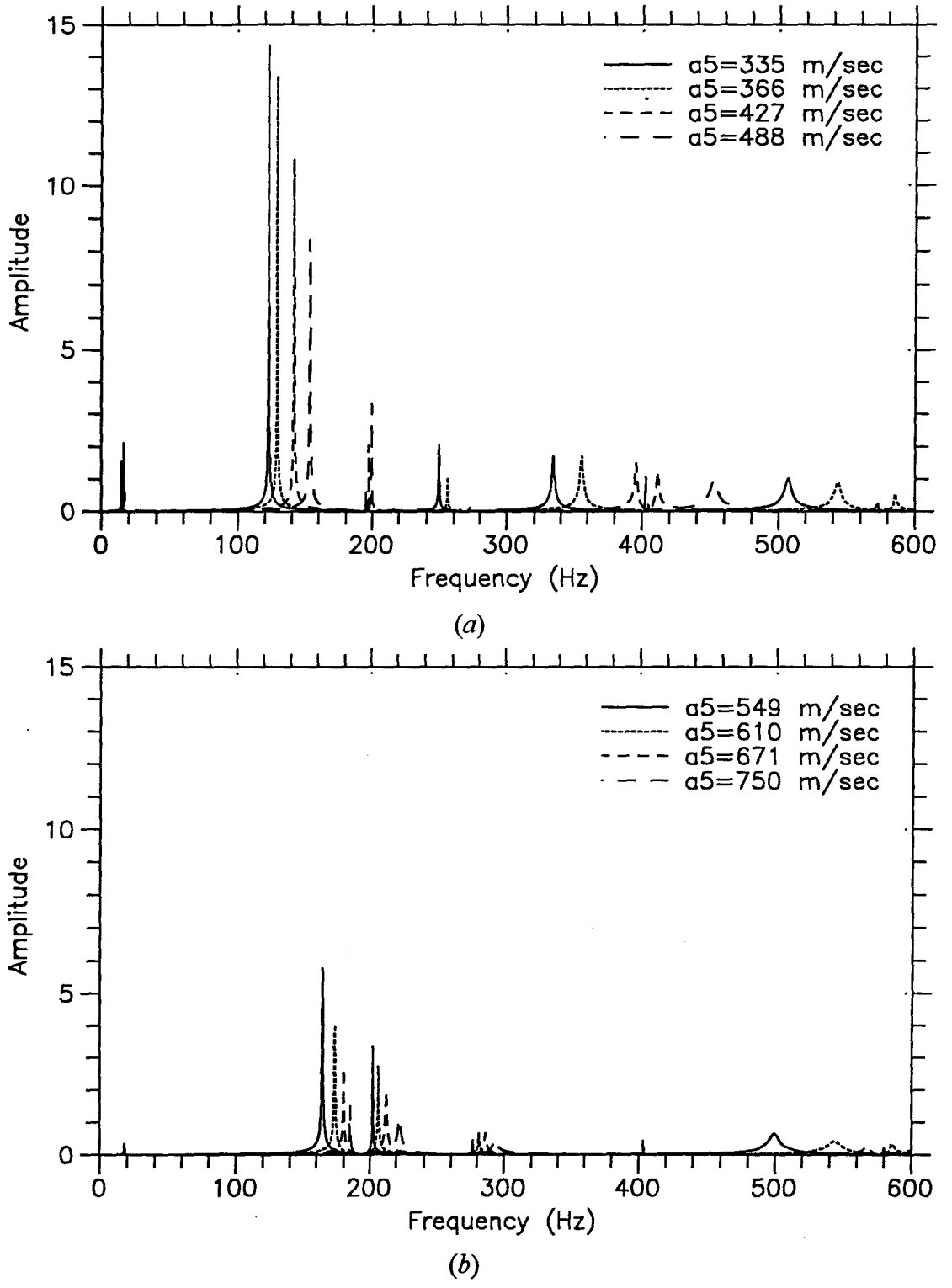

Figure 3.3: Pressure amplitude spectra for chamber with expansion ratio of 4.0 with unit driving at dump plane and $0 \leq \omega \leq 600$ Hz for various combustor sonic speeds (*a*) 335 m/sec $\leq a_5 \leq$ 488 m/sec, $\gamma_5 = 1.4$ and (*b*) 549 m/sec $\leq a_5 \leq$ 750 m/sec, $\gamma_5 = 1.3$.

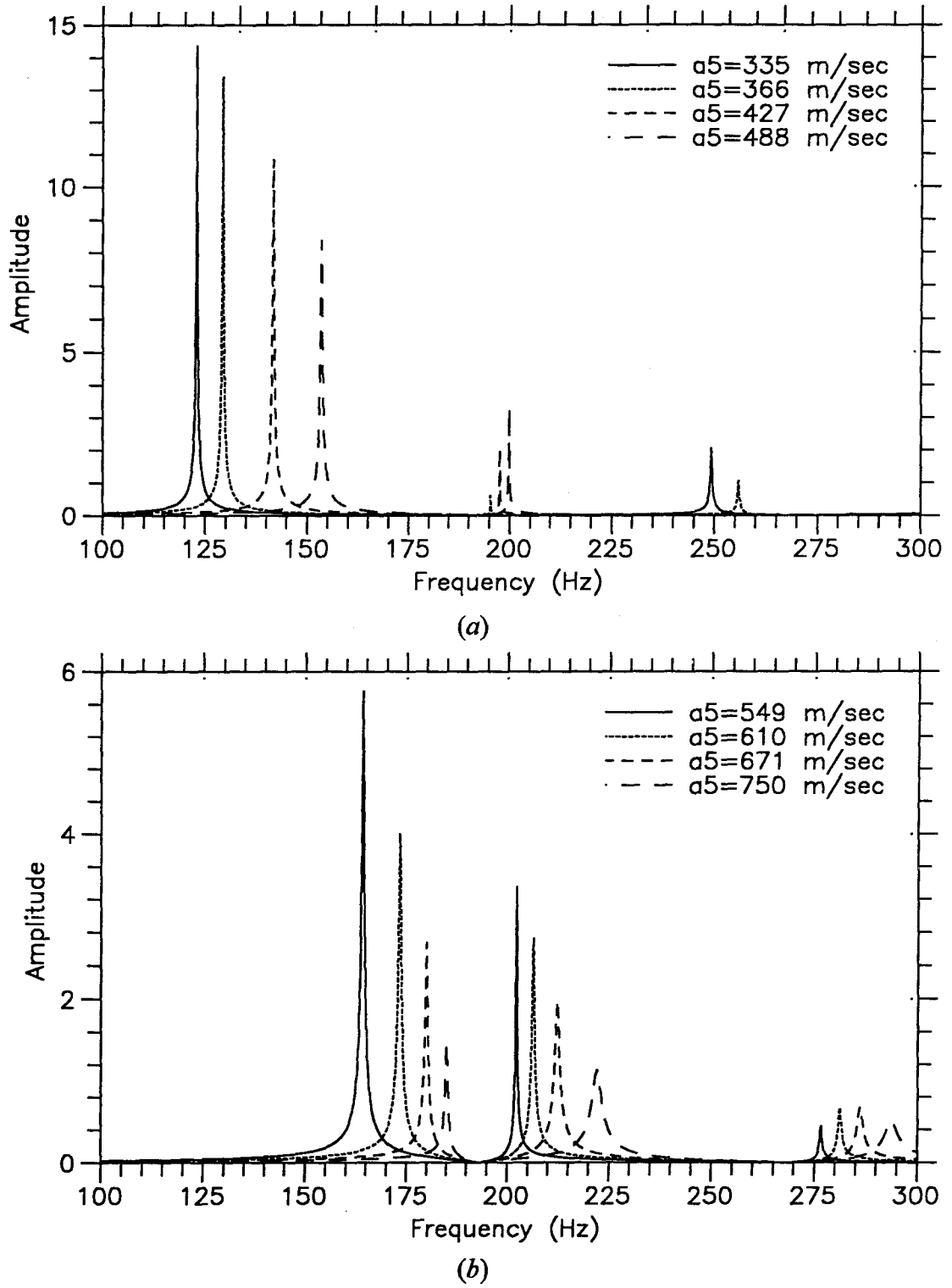

Figure 3.4: Pressure amplitude spectra for chamber with expansion ratio of 4.0 with unit driving at dump plane and 100 Hz $\leq \omega \leq$ 300 Hz for various combustor sonic speeds (*a*) 335 m/sec $\leq a_5 \leq$ 488 m/sec , $\gamma_5 = 1.4$ and (*b*) 549 m/sec $\leq a_5 \leq$ 750 m/sec, $\gamma_5 = 1.3$.

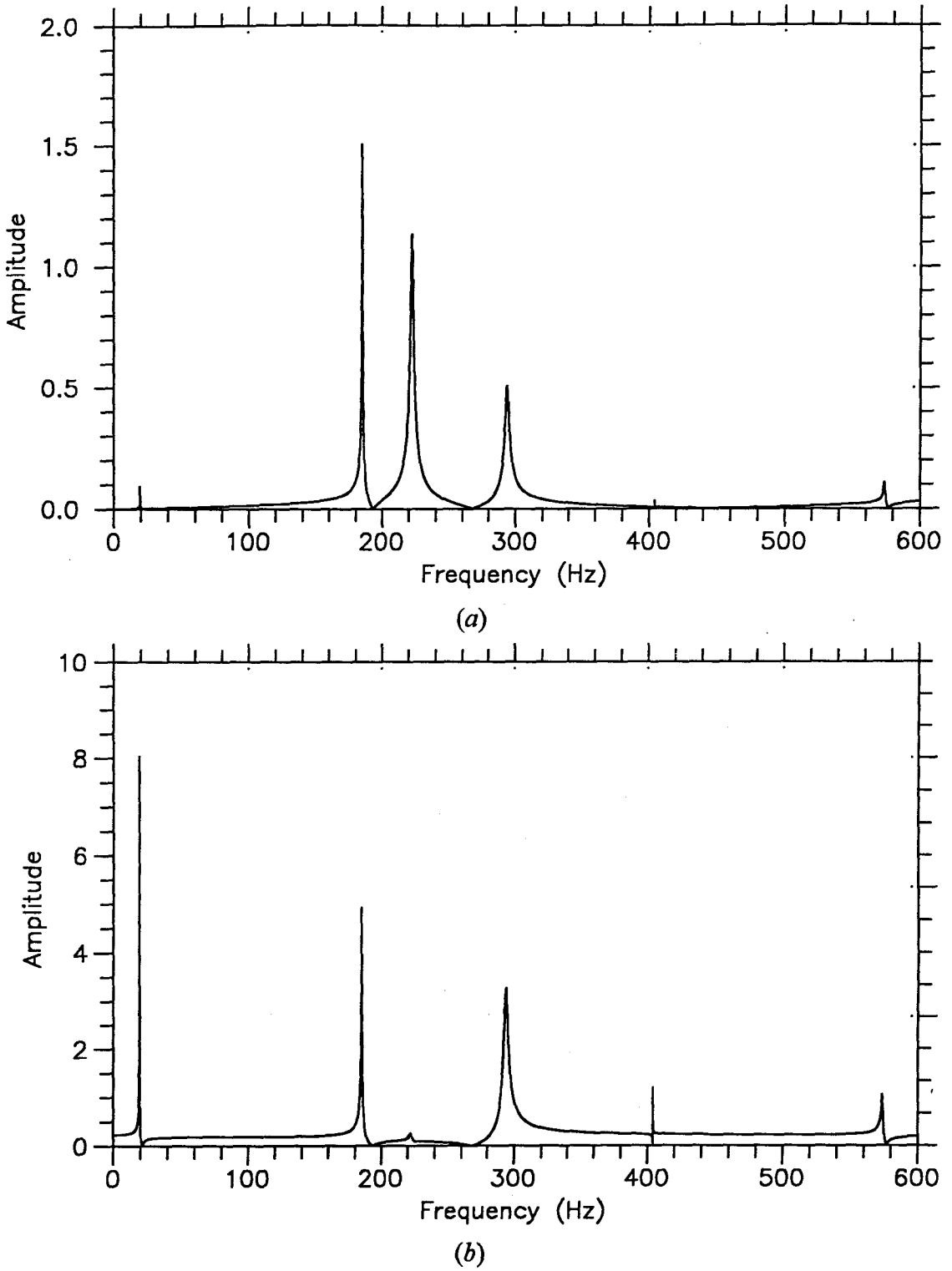

Figure 3.5: (*a*) Pressure and (*b*) velocity amplitude spectra for chamber with expansion ratio of 4.0 with unit driving at dump plane for hot-flow conditions.

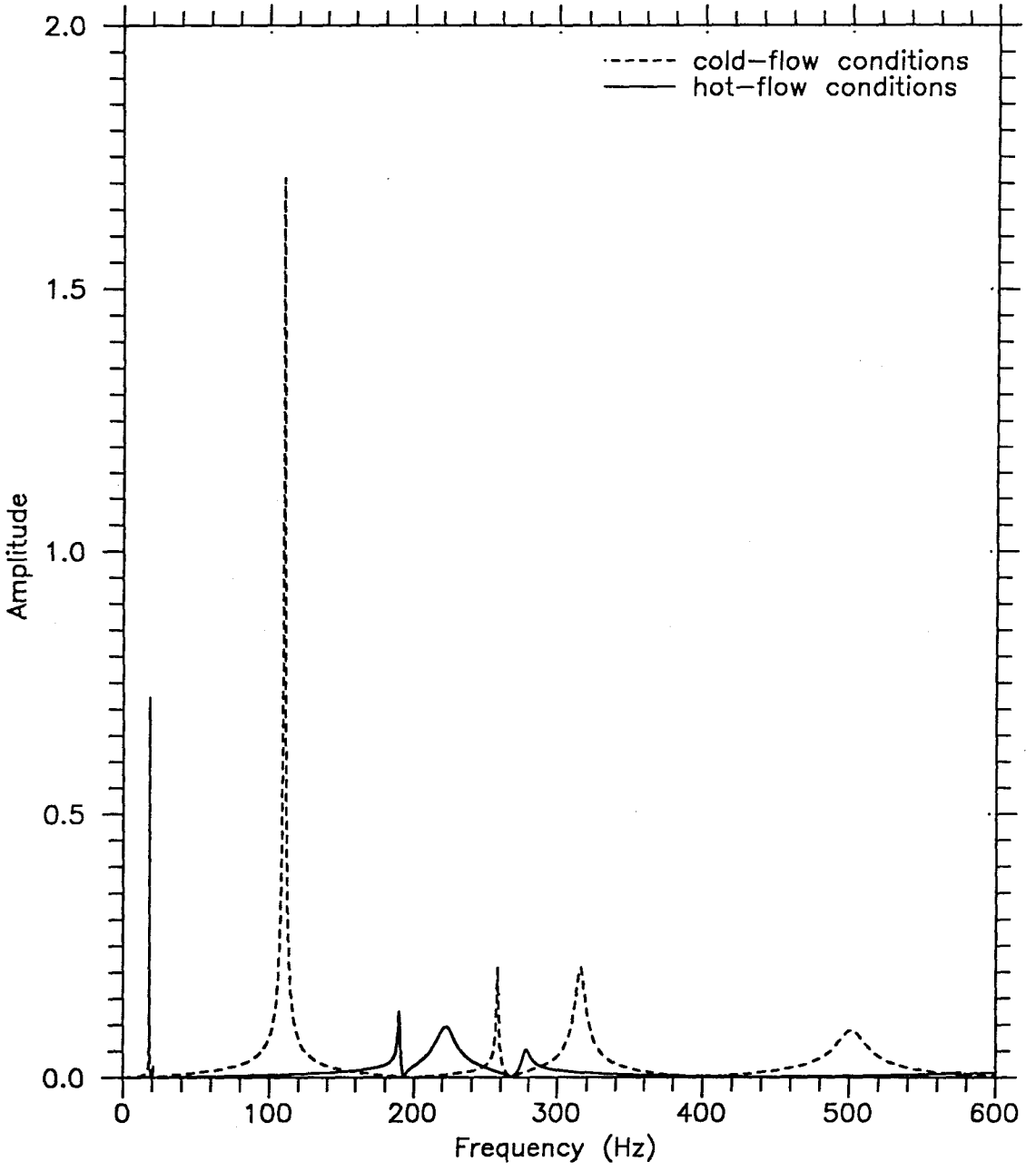

Figure 3.6: Pressure amplitude spectra for chamber with expansion ratio of 12.0 under cold- and hot-flow conditions with unit driving at dump plane.

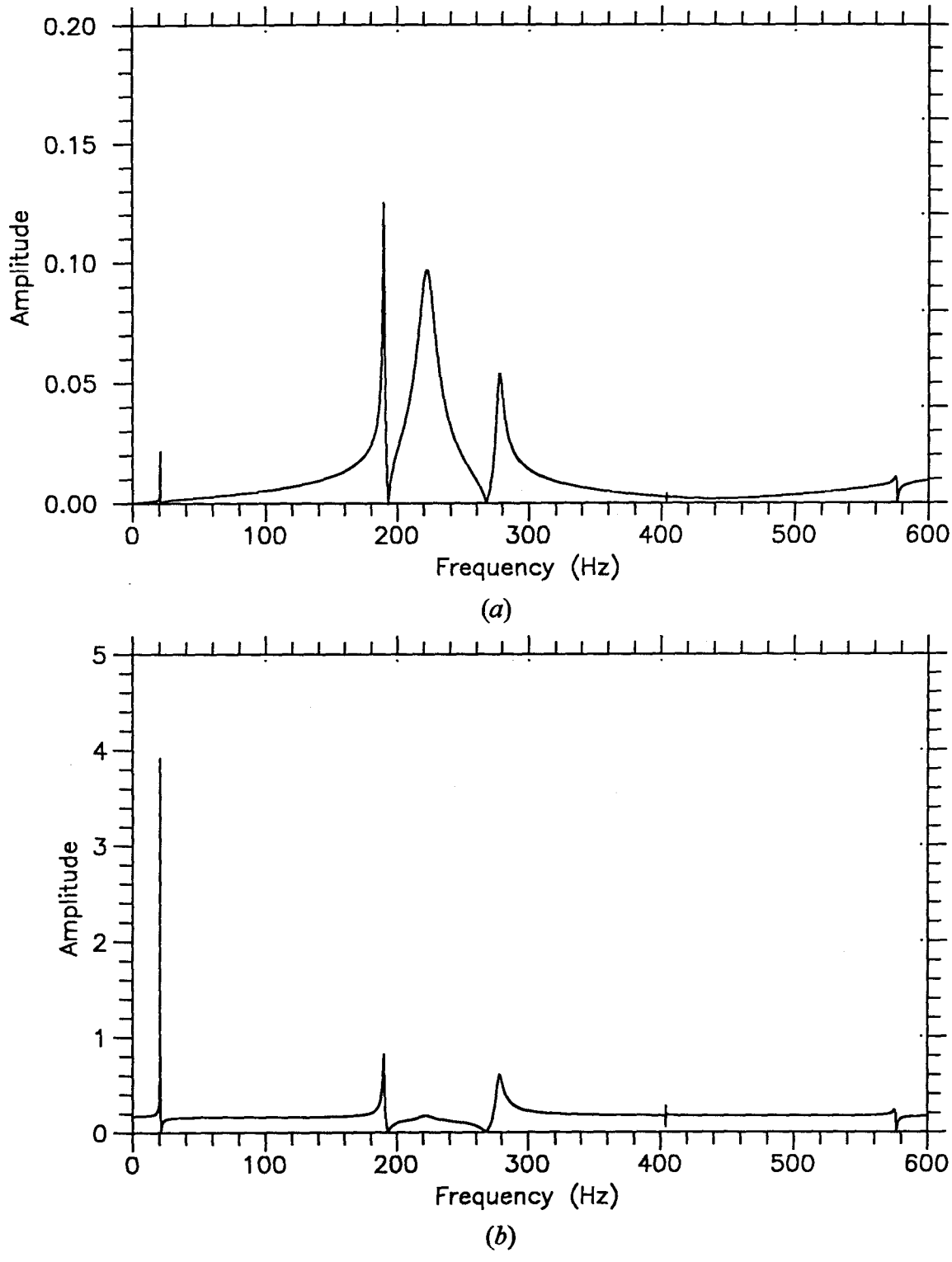

Figure 3.7: (*a*) Pressure and (*b*) velocity amplitude spectra for chamber with expansion ratio of 12.0 with unit driving at dump plane for hot-flow conditions.

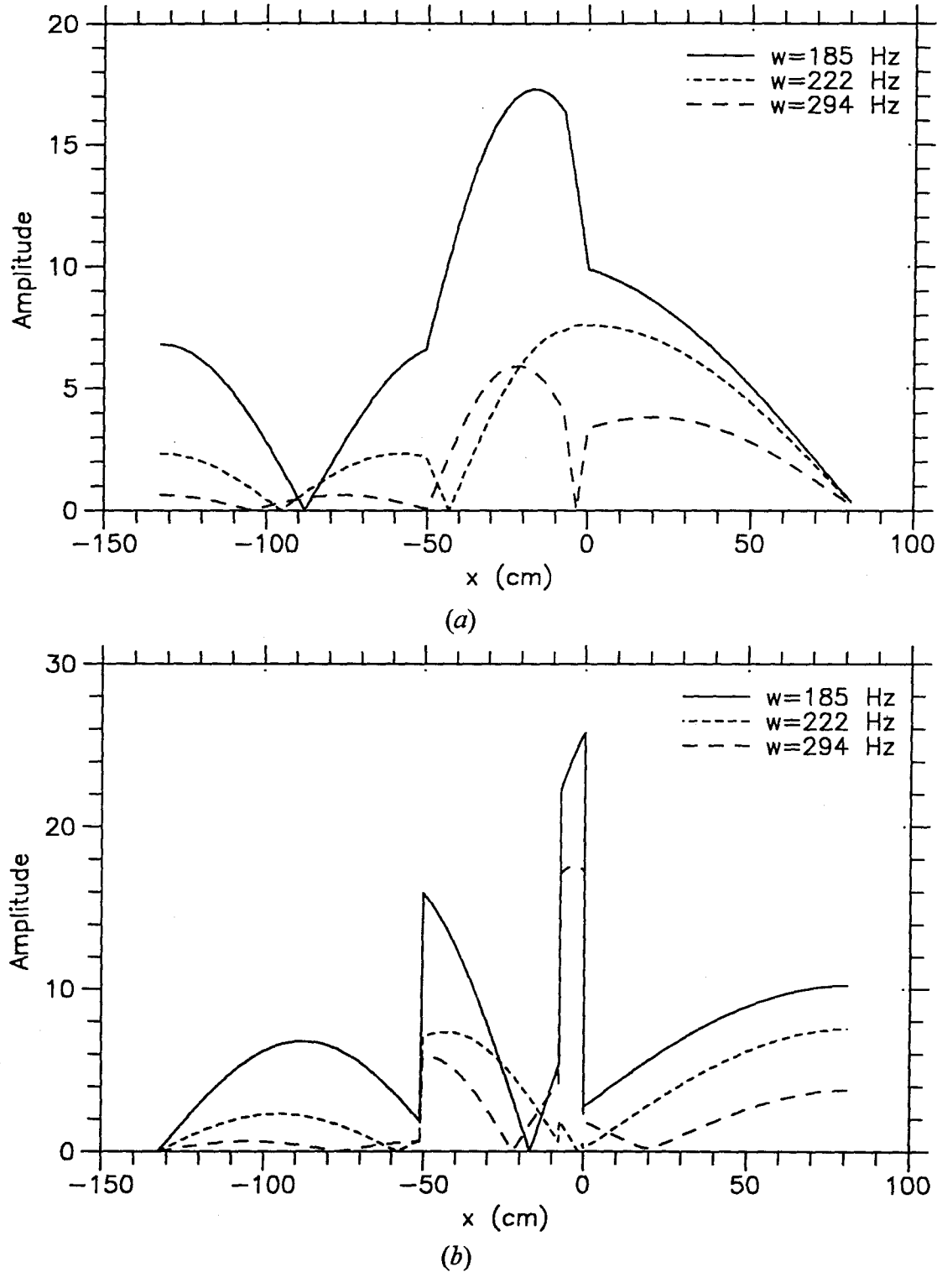

Figure 3.8: (*a*) Pressure and (*b*) velocity mode shapes of primary acoustic modes of chamber with expansion ratio of 4.0.

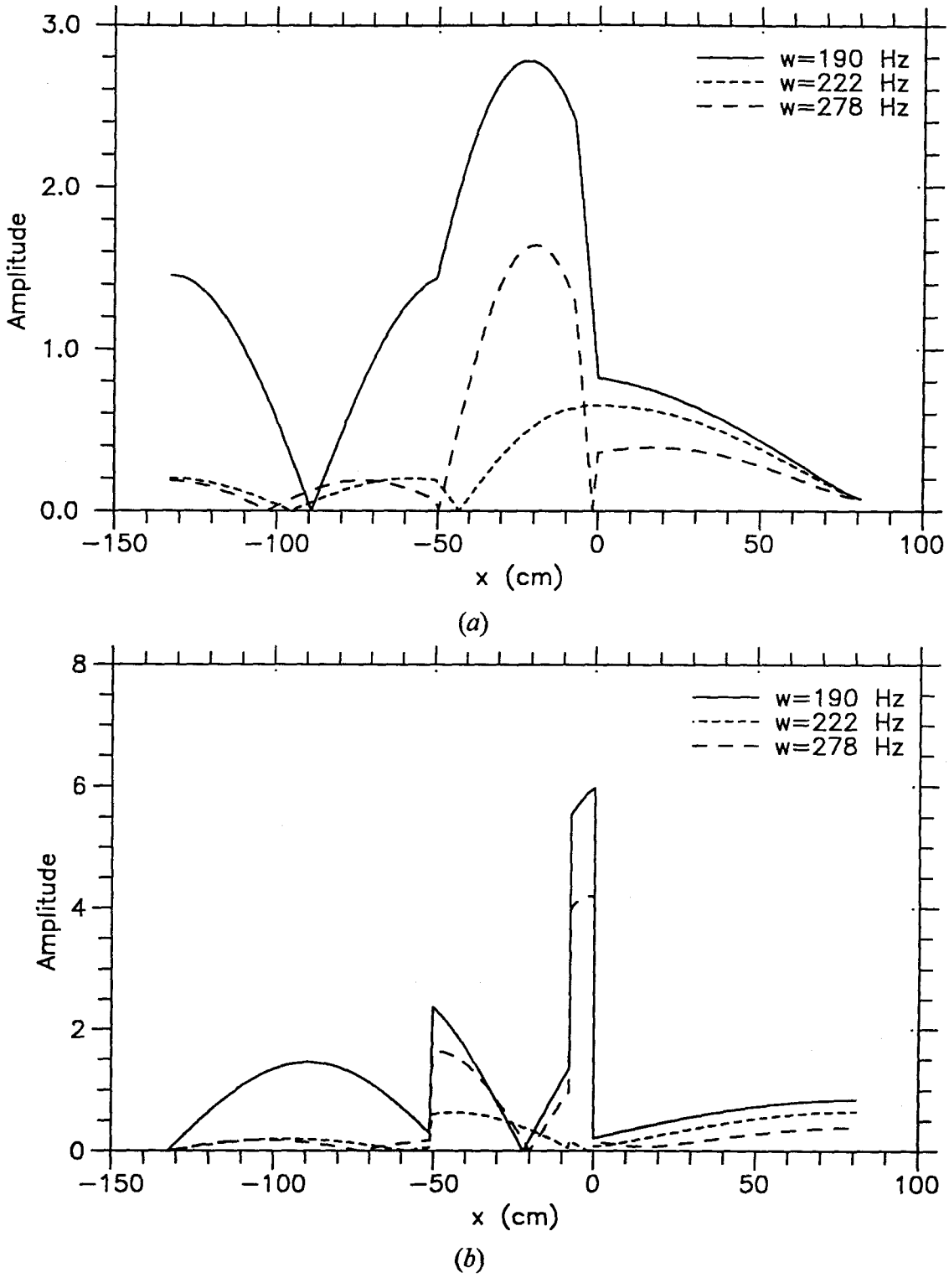

Figure 3.9: (*a*) Pressure and (*b*) velocity mode shapes of primary acoustic modes of chamber with expansion ratio of 12.0.

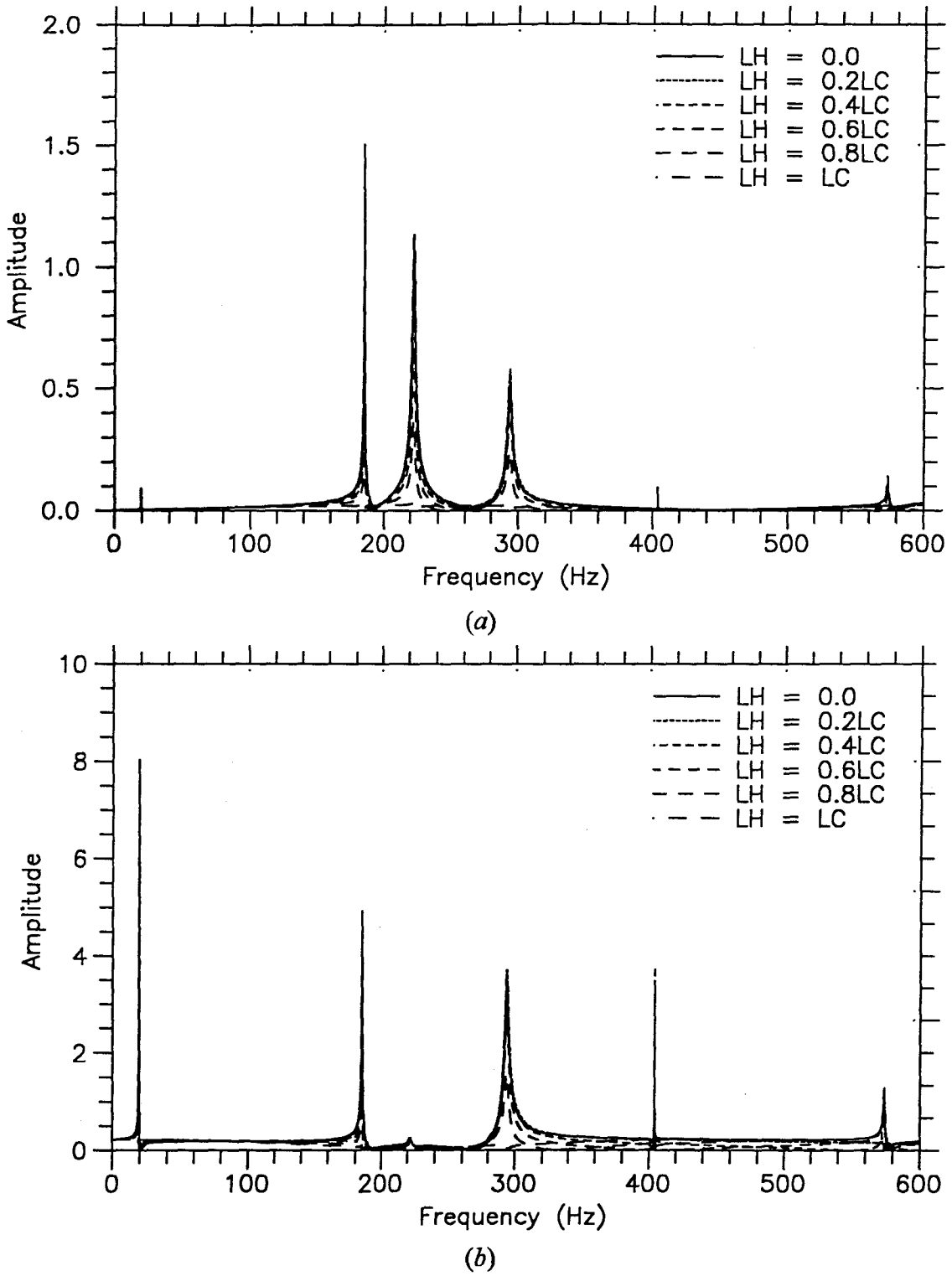

Figure 3.10: (*a*) Pressure and (*b*) velocity amplitude spectra for chamber with expansion ratio of 4.0 with unit driving at various locations $0 \le x = LH \le LC$.

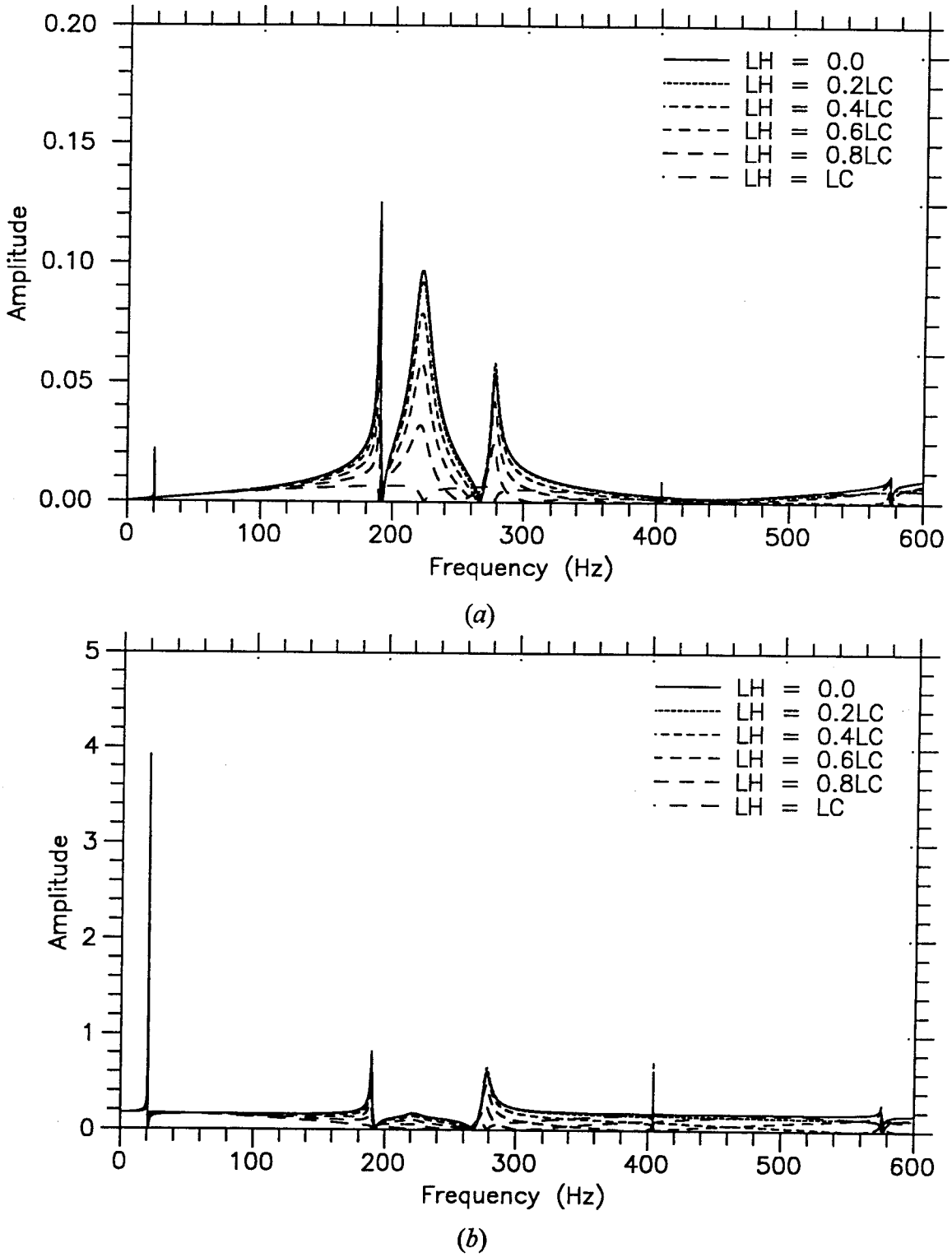

Figure 3.11: (*a*) Pressure and (*b*) velocity amplitude spectra for chamber with expansion ratio of 12.0 with unit driving at various locations $0 \le x = LH \le LC$.

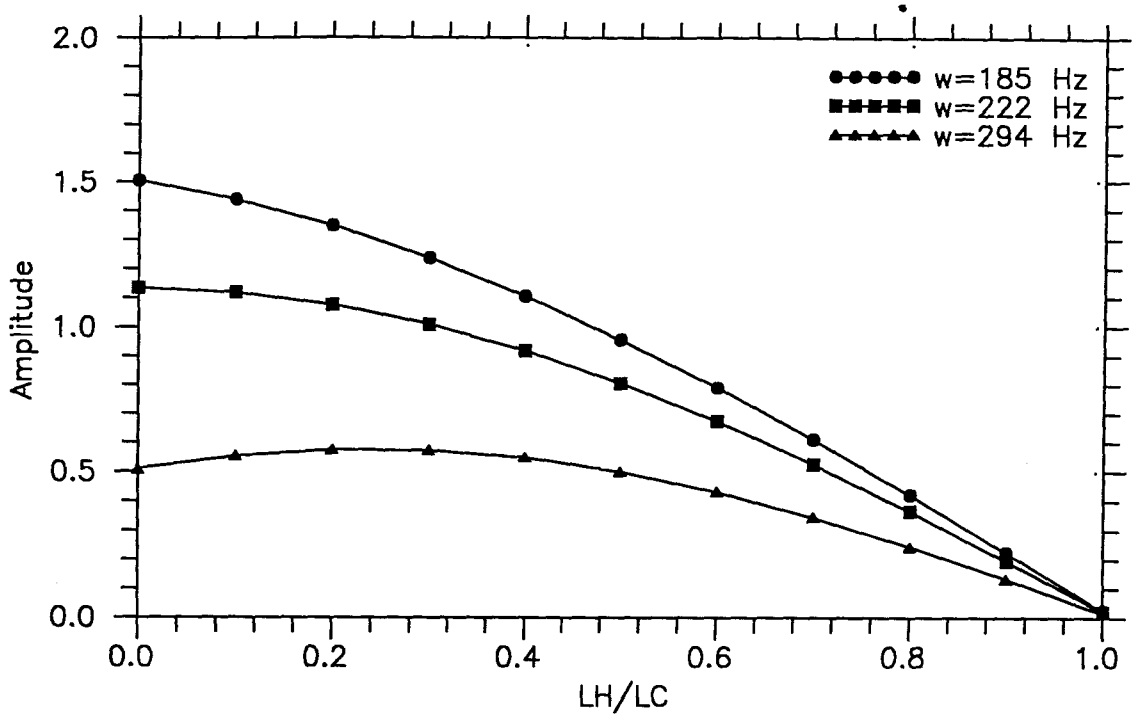

(*a*)

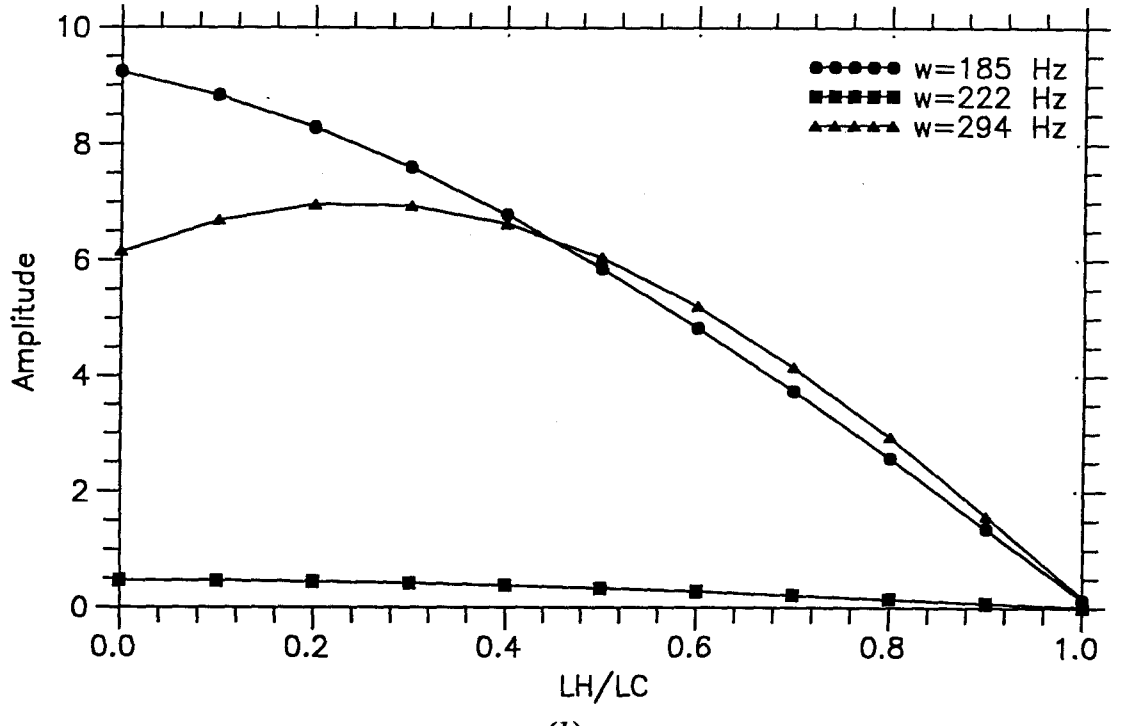

(*b*)

Figure 3.12: (*a*) Pressure and (*b*) velocity amplitudes of primary acoustic modes of chamber with expansion ratio of 4.0 as a function of unit driving location.

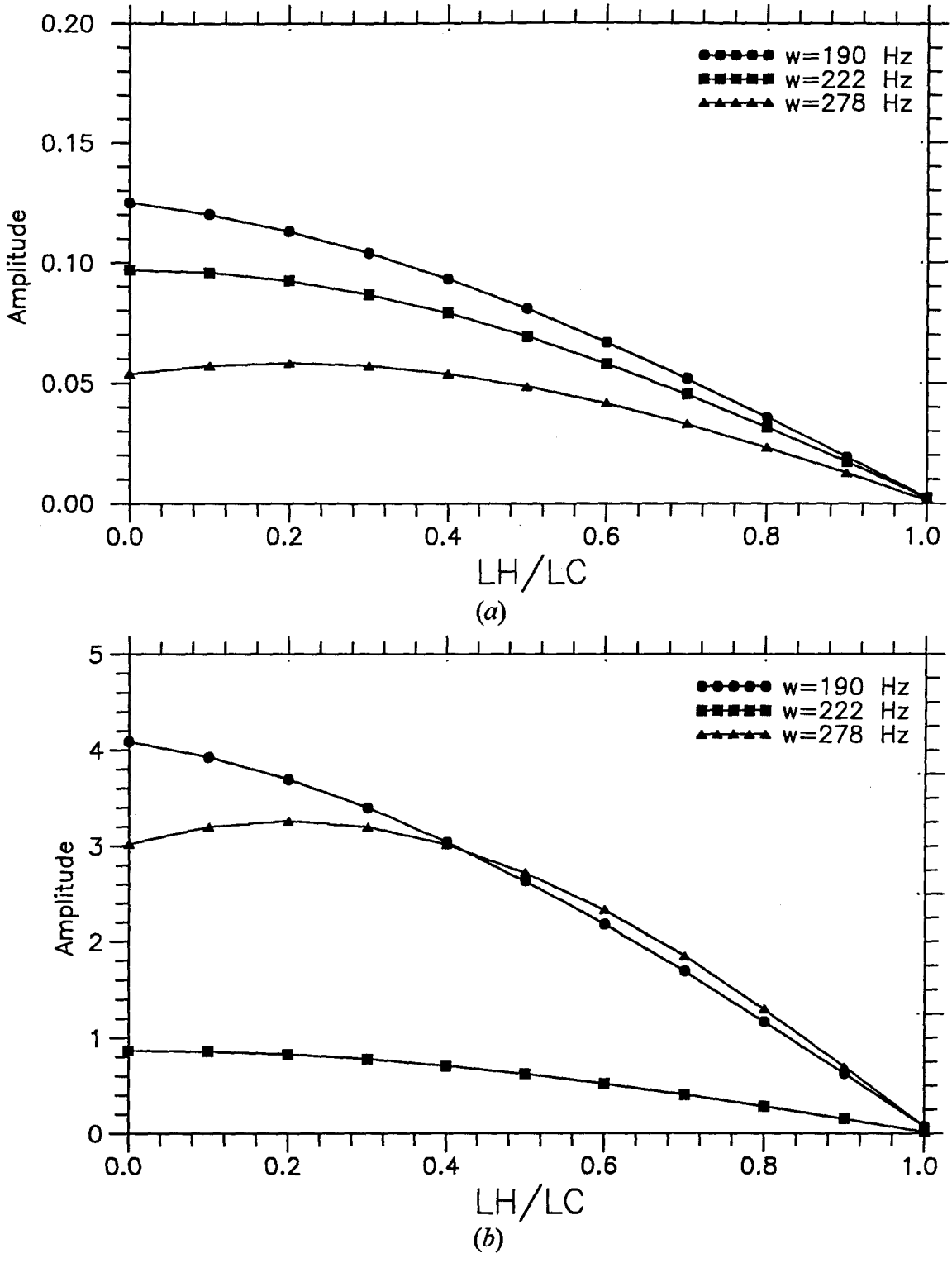

Figure 3.13: (*a*) Pressure and (*b*) velocity amplitudes of primary acoustic modes of chamber with expansion ratio of 12.0 as a function of unit driving location.

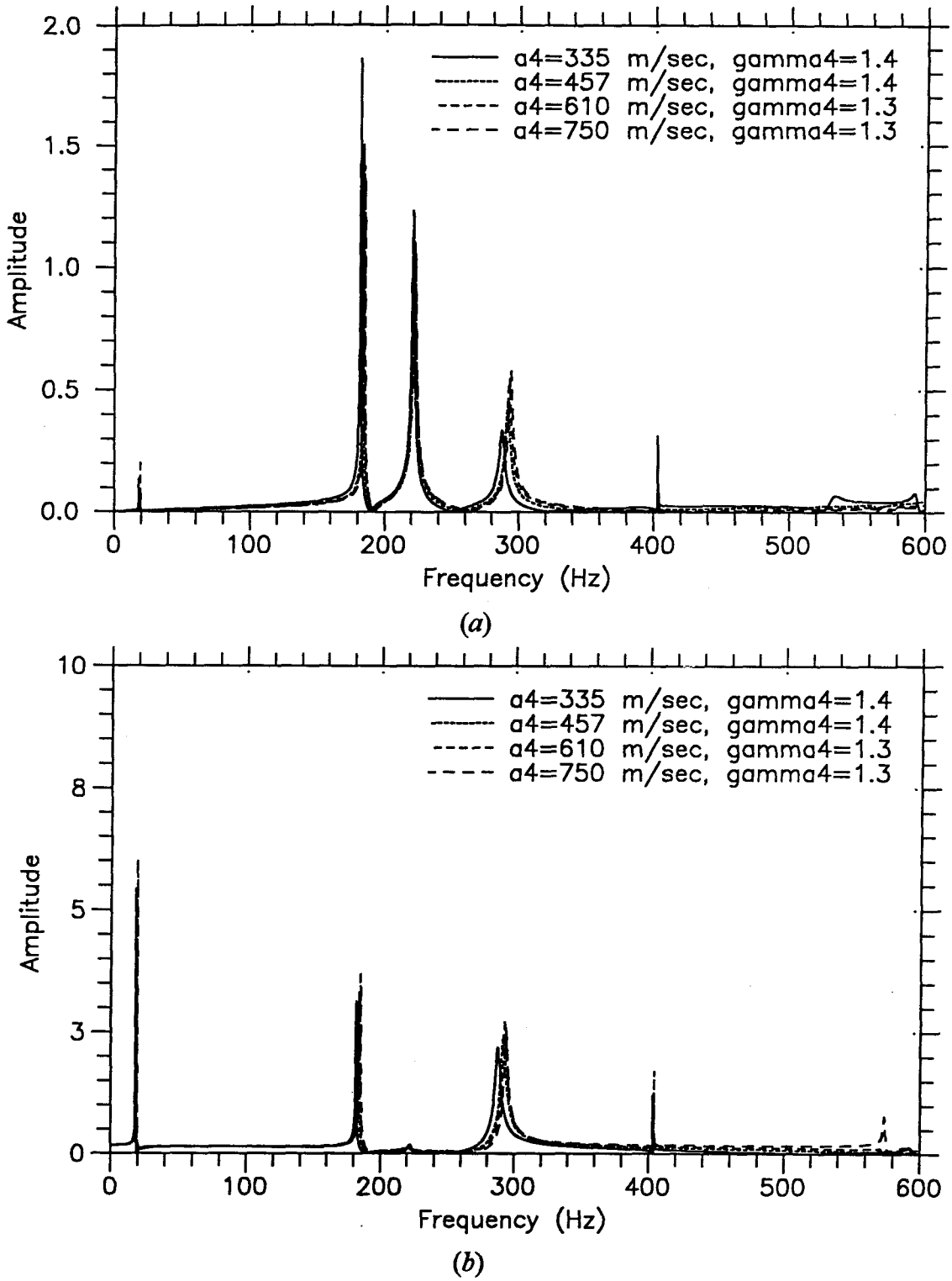

Figure 3.14: (*a*) Pressure and (*b*) velocity amplitude spectra for chamber with expansion ratio of 4.0 with unit driving at $LH = 0.2LC$ and various sonic speeds between $0 \le x \le LH$.

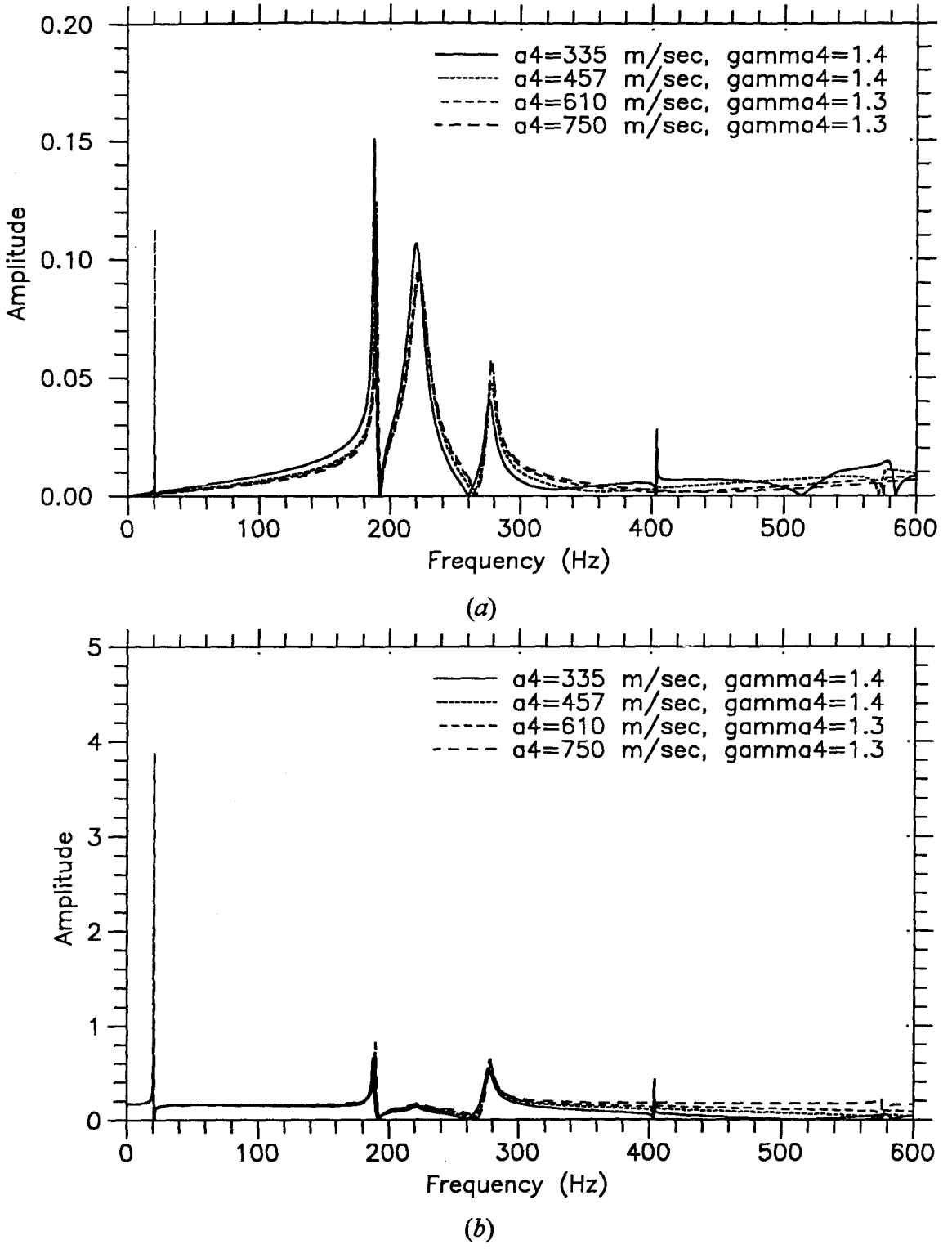

Figure 3.15: (*a*) Pressure and (*b*) velocity amplitude spectra for chamber with expansion ratio of 12.0 with unit driving at $LH = 0.2LC$ and various sonic speeds between $0 \le x \le LH$.

Chapter Four
Experimental Results

This chapter begins with an examination of typical experimental data records obtained for the 2.5-cm and 7.6-cm deep combustion chambers. First, particular emphasis will be placed on the experimental pressure amplitude spectra and how they compare with those obtained from the one-dimensional acoustic model discussed in the previous chapter. Next, the motion and growth of the reacting vortex structures will be examined by analyzing data obtained from the various diagnostic tools as well as from the different flow visualization methods including the images of the chemiluminescence.

4.1 Examination of Pressure and Velocity Data for the Two Expansion Ratios

Typically, the pressure oscillations within the combustor near the dump plane and the velocity fluctuations just upstream of the lip of the rearward-facing step are recorded during each experimental run. Examples of these data are given in Figure 4.1*a* for the 2.5-cm deep chamber and Figure 4.1*b* for the 7.6-cm deep chamber. The pressure oscillations are much stronger for the smaller depth duct, where

$$\left|\frac{p}{p_o}\right|_{2.5\ cm} \leq 0.15$$

$$\left|\frac{p}{p_o}\right|_{7.6\ cm} \leq 0.05.$$

Flow visualization shows that in either case, the surging flow into the chamber is periodically halted and at times reverses direction over the step so that

$$\left|\frac{u}{u_o}\right|_{2.5\ cm\ and\ 7.6\ cm} \geq 1.0.$$

The pressure amplitude spectrum for the 2.5-cm deep chamber is shown in Figure 4.2*a* and Figure 4.2*b* is the pressure amplitude spectrum of the 7.6-cm deep combustor. As one can see, the spectra are strikingly different. The 2.5-cm deep chamber is excited almost exclusively at the frequency of 186 Hz while the 7.6-cm deep chamber responds with excitations of the 187-Hz and 235-Hz modes. It is apparent that the different geometries have produced different acoustic behaviors signifying a change in the coupling mechanism between the pressure and the heat release within the combustion chamber due to the configuration change. A further analysis of the experimental data and the one-dimensional model is required. The larger chamber appears to be the most interesting with its multiple mode excitation; therefore, this case will be examined first.

4.2 Comparison of Experimental Spectra with Those Predicted by Acoustic Model

4.2.1 Expansion Ratio of 12.0

It is evident that the acoustic model predicts the resonant frequencies of the system quite well. For example, there are significant peaks associated with the frequencies of 187 Hz and 235 Hz as well as a much smaller peak at 281 Hz for the 7.6-cm deep combustion chamber. Remember that the model gave the natural modes as 190 Hz, 222 Hz, and 278 Hz for this configuration as shown in Figure 3.7*a*. The model as derived, however, is unable to correctly predict the relative magnitudes of the three peaks in the $p/\gamma p_o$ amplitude spectrum. The reason for this is simply because the acoustic model, as presented in Chapter 3, assumes a unit driving for all frequencies. Clearly, the heat addition, or driving, is not of uniform magnitude over the frequency range of interest. Rather, it is coupled with the vortex shedding from the lip of the rearward-facing step flame holder. Figure 4.3*a* shows the velocity spectrum of the signal from the hot-wire

anemometer which is placed just upstream of the dump plane in the cold flow for the 7.6-cm deep chamber. Once again the resonant modes are clearly represented in the spectrum with the mode at 235 Hz dominating the others. It is expected that the heat release follows the same pattern with frequency as the velocity; however, it is not possible to correctly assume what the characteristics of the driving amplitude spectrum are. It is possible, though, to experimentally determine the amplitude spectrum of the driving by taking advantage of the linear relationship between the light intensity of the chemiluminescence and the heat release of the combustion process. Once obtained, the driving spectrum can be inserted into the acoustic model, and the resulting $p/\gamma p_o$ spectrum can then be more realistically compared to the experimentally obtained pressure amplitude spectrum.

Light emitted from the combustion chamber over the first 30 cm downstream of the dump plane was focused into the photomultiplier tube for both combustion chamber configurations using one of the 32-cm diameter spherical mirrors as shown in Figure 4.4. In each case, visible combustion appeared to terminate at a distance of less than 30 cm downstream of the step, so it is felt that the entire region over which heat release occurs has been accounted for. With the system depicted in Figure 4.4, less than 15% of the total chemiluminescent radiation emitted by the combustion process could be captured for analysis. However, because the frequency content of the light emission signal is the important aspect of this measurement, and the frequency content is the same irrespective of the direction of emission, this limitation in light-gathering capacity is not detrimental to the objective of this part of the investigation and only decreases the amplitude of the measurement. The resulting light intensity measurement will contain the desired frequency content of the total heat release, and it will also contain important phase information which will prove useful later.

The amplitude spectrum of the heat release for the 7.6-cm deep chamber is shown in Figure 4.3*b*. Note the similarities with the velocity spectrum of Figure 4.3*a*, namely, a

dominating peak at 235 Hz with smaller peaks at the other resonant modes on either side. This figure gives the frequency content of the total heat release for the 7.6-cm deep chamber under the given flow conditions. Clearly, the driving is not uniform over the frequency range of interest. A calculation of the $p/\gamma p_o$ amplitude spectrum as determined from the acoustic model using the experimentally derived driving spectrum gives the result shown in Figure 4.5*b*. Here, the resonant frequencies of the experimental driving spectrum have been shifted slightly so that the experimental modes coincide with those of the one-dimensional model. It is recalled that the acoustic model revealed the peaks in the pressure amplitude spectrum to be very sharp (Figure 3.5*a*). Because of this, the magnitude of the response decreases rapidly as one moves slightly above or below the values of the natural mode frequencies. The experimentally determined resonant values, therefore, must be equal to those determined from the one-dimensional model to obtain a better comparison between the predicted response and the actual pressure response of the combustor. The frequency scaling is as follows.

(*i*) For $\omega \le \omega_{model}^{plenum}$,

$$\omega = \omega \times \left(\frac{\omega_{model}^{plenum}}{\omega_{experiment}^{plenum}} \right)$$

so that the 'plenum modes' are aligned. For example, the frequency of 100 Hz is shifted to the value

$$\omega = 100 \text{ Hz} \times \left(\frac{190 \text{ Hz}}{187 \text{ Hz}} \right) = 101.6 \text{ Hz}$$

and the experimental 'plenum mode' frequency of 187 Hz shifts upward to 190 Hz, the value as determined by the acoustic model.

(*ii*) For $\omega_{experiment}^{plenum} \le \omega \le \omega_{experiment}^{combustor}$,

$$\omega = \omega_{model}^{plenum} + \left| \left(\omega - \omega_{experiment}^{plenum} \right) \times \left(\frac{\omega_{model}^{combustor} - \omega_{model}^{plenum}}{\omega_{experiment}^{combustor} - \omega_{experiment}^{plenum}} \right) \right|$$

so that the 'organ pipe modes' coincide. The frequency of 200 Hz, for example, becomes

$$\omega = 190\ Hz + \left| (200\ Hz - 187\ Hz) \times \left(\frac{222\ Hz - 190\ Hz}{235\ Hz - 187\ Hz} \right) \right| = 198.7\ Hz$$

and the experimental 'organ pipe mode' of 235 Hz is moved to 222 Hz.

(*iii*) For $\omega_{experiment}^{combustor} \le \omega \le \omega_{experiment}^{highest}$,

$$\omega = \omega_{model}^{combustor} + \left| \left(\omega - \omega_{experiment}^{combustor} \right) \times \left(\frac{\omega_{model}^{highest} - \omega_{model}^{combustor}}{\omega_{experiment}^{highest} - \omega_{experiment}^{combustor}} \right) \right|$$

allowing the highest primary modes to align. The frequency of 250 Hz is now

$$\omega = 222\ Hz + \left| (250\ Hz - 235\ Hz) \times \left(\frac{278\ Hz - 222\ Hz}{281\ Hz - 235\ Hz} \right) \right| = 240.3\ Hz.$$

Finally,

(iv) for $\omega_{experiment}^{highest} \le \omega \le 600$ Hz,

$$\omega = \omega \times \left(\frac{600\ \text{Hz} + 1\ \text{Hz}}{600\ \text{Hz}} \right) - 1\ \text{Hz}$$

so that the upper frequency limit matches that of 600 Hz. For example, the frequency of 400 Hz changes to

$$\omega = 400\ \text{Hz} \times \left(\frac{601\ \text{Hz}}{600\ \text{Hz}} \right) - 1\ \text{Hz} = 399.7\ \text{Hz}.$$

Figure 4.6*a* shows the actual experimental driving spectrum for the 7.6-cm deep combustion chamber configuration and Figure 4.6*b* gives its corrected counterpart so that

the three primary modes coincide with those determined by the one-dimensional model. As one can see, there is very little difference between the two.

A driving magnitude of 1.5 m^3/sec, such that

$$D_{7.6\,cm}(\omega) = \frac{I_{7.6\,cm}(\omega)}{\sum_{\omega} I_{7.6\,cm}(\omega)} \times 1.5 \text{ m}^3/\text{sec},$$

has been used so that the peak at 235 Hz scales with that in the experimental pressure amplitude spectrum shown again in Figure 4.5*a* allowing the two spectra to be shown on the same scale. In the above equation, $D_{7.6\,cm}(\omega)$ is the driving at frequency ω and $I_{7.6\,cm}(\omega)$ is the experimentally determined value of the radiation intensity amplitude at a particular frequency ω for the 7.6-cm deep chamber. The two spectra of Figure 4.5 agree quite well. There is a slight underprediction by a factor of 0.96 in the amplitude of the 187-Hz mode and an overprediction by a factor of 2.42 for the 281-Hz mode. Because the mode at 281 Hz is of little acoustic consequence compared to the other modes, the overprediction of its amplitude by nearly a factor of 2.50 is not very disturbing.

The spectrum of u_3/a_o for the 7.6-cm deep chamber as predicted by the acoustic model for the same driving is given in Figure 4.7*b* next to the experimental velocity spectrum upstream of the dump plane repeated in Figure 4.7*a*. As one can see, the agreement of the relative amplitudes between the two plots is not strong. The reason for this lack of agreement is believed to be due to the complexity of the actual flow above the flame holder and over the step. The flow is complex because of the occurrence of phenomena such as flow reversal and flow separation which cannot be accounted for by one-dimensional acoustics.

It has been demonstrated (Sterling (1987*a*), and Hegde *et al.* (1991), for example) that the phase relationship between the fluctuating pressure and oscillating heat release within the combustion chamber dictates whether or not acoustic energy is amplified or

damped at a particular frequency. This is commonly referred to as the Rayleigh Criterion (Rayleigh 1878). It is proposed that the dominant acoustic mode of the system is the one for which the heat release and pressure are most closely in-phase with one another. Other phase relationships of interest are those between the heat release and the fluctuating velocity over the flame holder, giving an idea of the delay between the shedding of a vortex structure and its combustion, and those between the oscillating pressure within the chamber and the fluctuating velocity over the step, showing how the vortex shedding is affected by the pressure within the chamber. A phase analysis, given in Table 4.1, shows the following results for the 7.6-cm deep chamber, where the phase difference $\Delta\vartheta_{j-k}$ is defined as $\Delta\vartheta_{j-k} \equiv \vartheta_j - \vartheta_k$. Furthermore, if $\Delta\vartheta_{j-k} \leq 0$ then signal j is said to lead signal k and if $\Delta\vartheta_{j-k} \geq 0$ then signal j is said to lag signal k.

Table 4.1: Phase relationships for the 7.5-cm deep combustion chamber.

FREQ (Hz)	$\Delta\vartheta_{i-p}$ (degrees)	$\Delta\vartheta_{i-v}$ (degrees)	$\Delta\vartheta_{v-p}$ (degrees)
187	-64	179	118
235	19	-26	45
281	39	-45	84

Here, the subscripts p, v, and i denote pressure, velocity, and light intensity oscillations, respectively. As one can see, the pressure oscillations and heat release fluctuations are more closely in phase for the 235-Hz combustion chamber mode which is the dominant vortex shedding mode as shown by the velocity amplitude spectrum, Figure 4.3*a* or 4.7*a*. The second column of the table shows that the heat release and pressure are 19 degrees out of phase at a frequency of 235 Hz. This is considerably smaller than the phase differences between the heat release and pressure at the other two acoustic modes. It is felt that this phase relationship is responsible for the domination of the 235-Hz mode over

the others in the duct. The lack of excitement of the 281-Hz mode is due primarily to fuel type or chemical reaction time. Recent experiments performed at the dump combustor facility and not reported here have shown that this mode can be more vigorously excited by using a more easily ignitable fuel, such as a mixture of 15% hydrogen or 30% hydrogen in methane, where these are the mass fractions of hydrogen used. The smaller, 2.5-cm deep chamber behaves in a very different manner and will be examined next.

4.2.2 Expansion Ratio of 4.0

As noted previously and shown in Figure 4.2*a*, the pressure within the 2.5-cm deep combustor responds almost exclusively to excitations occurring at a frequency of 185 Hz. There is a much smaller response near the harmonic of this frequency at 369 Hz. One would expect the dominant vortex shedding and heat release mode to be equal to 185 Hz as well, and the velocity and light intensity spectra of Figure 4.8*a* and 4.8*b*, respectively, indicate that indeed vortices are being shed and heat release is occurring primarily at a frequency of 185 Hz. Both plots also indicate a slight response at 208 Hz, a non-acoustic mode as determined by the one-dimensional model which gave the frequencies of 185 Hz, 222 Hz, and 294 Hz as the resonant modes for this configuration. Because the length scales have remained the same for this expansion ratio, it is not plausible that the 'organ pipe mode' of the combustion chamber has dropped 6.3% from its value of 222 Hz to a value of 208 Hz; therefore, the small response at this frequency must originate from the combustion process itself rather than from any acoustic means. This non-resonant mode in the velocity and heat release spectra does not appreciably appear in the pressure response.

When the heat release spectrum of Figure 4.8*b* is used as the driving spectrum for the one-dimensional model, the resulting $p/\gamma p_o$ spectrum is shown in Figure 4.9*b*. Here, a driving magnitude of 0.5 m^3/sec, such that

$$D_{2.5\,cm}(\omega) = \frac{I_{2.5\,cm}(\omega)}{\sum_{\omega} I_{2.5\,cm}(\omega)} \times 0.5 \text{ m}^3/\text{sec},$$

has been used so that the peak at 185 Hz scales with that at the same frequency in the experimental pressure amplitude spectrum shown again in Figure 4.9*a*. The quantity $D_{2.5\,cm}(\omega)$ in the above equation is the driving at frequency ω and $I_{2.5\,cm}(\omega)$ is the value of the radiation intensity amplitude spectrum at a particular frequency ω as determined experimentally for the 2.5-cm deep combustion chamber. One can see that the model predicted a much stronger response at the resonant mode of 222 Hz, stronger by a factor of 17.5, and failed to predict the responses at the non-acoustic mode of 208 Hz and the harmonic at 369 Hz. Because these responses are still negligible when compared to the dominant response at 185 Hz, these shortcomings are not of great importance.

The velocity response u_3/a_o for the same driving spectrum is given in Figure 4.10*b* next to the experimental velocity spectrum repeated in Figure 4.10*a*. The model has predicted that the only significant response to this driving input occurs at a frequency of 185 Hz which is clearly the case for the experimental data; however, the responses at the non-acoustic mode of 208 Hz and at the harmonic frequency of 369 Hz, evident in Figure 4.10*a*, have not been accounted for.

An analysis of the phase information for the 2.5-cm deep chamber gives the following relationships shown in Table 4.2. Once again, the subscripts *p*, *v*, and *i* denote pressure, velocity, and light intensity oscillations, respectively. The resonant mode at 185 Hz, which dominates the pressure, velocity, and light intensity spectra for the 2.5-cm deep combustion chamber, can be seen to be the one whose pressure and heat release oscillations are most nearly in phase as compared with the other two acoustic modes at 222 Hz and 294 Hz, as shown in the second column of the table. The same relationship between the pressure fluctuations and heat release oscillations was found for the dominant

235-Hz mode, you will remember, for the 7.6-cm deep chamber. The dominant mode, or vortex shedding mode, therefore, is the one for which the pressure and heat release are most nearly in phase. It is not clear, however, how the dominant mode is chosen among the several acoustic modes present. A further examination of the other experimental data is required and will be undertaken in the following sections. Nevertheless, this section has shown the merits of one-dimensional linear acoustics as a simple means to predict the overall behavior of the laboratory dump combustor for different expansion ratios and for given heat release frequency spectra.

Table 4.2: Phase relationships for the 2.5-cm deep combustion chamber.

FREQ (Hz)	$\Delta\vartheta_{i-p}$ (degrees)	$\Delta\vartheta_{i-v}$ (degrees)	$\Delta\vartheta_{v-p}$ (degrees)
185	-28	-150	123
208	-21	154	133
222	-79	-120	41
294	83	-12	95
369	79	73	6

The investigation now shifts to a more focused examination of the reacting vortex structures shed from the lip of the rearward-facing step flame holder in an effort to explain the different behaviors of the dump combustor for the two chamber configurations. It will begin with a comparison of the flow fields through an examination of spark shadowgraph images. From there, the combustion processes will be investigated, first, intrusively with ionization probes, and then non-intrusively with chemiluminescence imaging using the intensified camera. Finally, temperature profiles will be examined as will velocity field measurements.

4.3 Shadowgraph Images

This section contains a description of the flow fields of the two combustion chamber configurations as determined by the flow visualization techniques of spark and high-speed motion picture shadowgraphy. Smith (1985*a*, *b*) and Sterling (1987*a*, *b*) found the flow field of the laboratory dump combustor to be dominated by the presence of large vortex structures shed from the lip of the rearward-facing step flame holder when the combustor is operating in a pulsating, or unstable, mode. Their studies, however, were performed only for the 2.5-cm deep combustion chamber. Because the findings noted previously in the examination of the acoustic response of the apparatus indicate a very different behavior for the deeper chamber configuration as far as the vortex shedding frequency is concerned, a comparison of the flow fields is in order.

4.3.1 Expansion Ratio of 4.0

The evolution of the vortex structure for a typical cycle of the 2.5-cm deep chamber is shown in the sequence of shadowgraph images presented in Figure 4.11. Remember that the vortex shedding frequency is 185 Hz for this case giving a period of 5.41 msec. These photographs were obtained from a high-speed motion picture of the pulsating flow where the framing rate was approximately 5100 frames per second giving nearly 28 frames per cycle for the 2.5-cm deep configuration. The time-step between the frames shown in Figure 4.11 is 0.2 msec, equal to 13 degrees in one complete cycle of oscillation. Flow is from left to right with the rearward face of the step flame holder and the 0.6-cm inlet to the chamber visible at the upstream end of the image. An axial distance of 30 cm downstream from the dump plane can viewed, and one must recall that the shadowgraph technique is an integrating method over the line-of-sight of the parallel light beam from the mercury arc-lamp. The beam is traveling into the page in this case. These images are of poor quality, and the reader is encouraged to consult either Smith (1985*a*,

b) or Sterling (1987*a*, *b*) to view more detailed shadowgraph images of the flow field in the first 12 cm downstream of the dump plane for the 2.5-cm deep chamber configuration.

The vortex structure can be seen to be emerging from the lip of the rearward-facing step flame holder in the upper left corner of Figure 4.11*a*. This first image was obtained approximately 39 degrees after the pressure had reached its maximum value in the combustion chamber. Two points are obvious from examining the cycle of oscillation shown in Figure 4.11. The first is that only one vortex structure is present in the visible portion of the chamber during each operating cycle, and the second is that the shed vortex travels only a short distance downstream of the dump plane before encountering the lower wall of the combustion chamber. The shape of the vortex begins to deform and elongate in Figure 4.11*i*, 143 degrees from the time that it was shed from the step. The leading edge is only 5 cm downstream of the dump plane in this case. The subsequent collision of the structure with the lower wall, depicted in Figures 4.11*m* through *v* where the combustion chamber pressure is increasing, destroys the vortical shape of the structure. This interaction with the lower wall greatly enhances the mixing of the fuel with the hot products of combustion thereby initiating a large burst of heat release, as noted by Smith (1985*a*, *b*). Combustion is seen to linger along the upper wall of the chamber during the completion of the cycle as well as propagate upstream beyond the dump plane into the inlet section during the height of activity.

4.3.2 Expansion Ratio of 12.0

A sequence of motion picture shadowgraph images for the 7.6-cm deep combustor is shown in Figure 4.12, where, once again, the framing rate of the Hycam is 5100 frames per second giving nearly 22 frames per cycle of oscillation. Here, one period is equal to 4.26 msec for the 235-Hz vortex shedding frequency; therefore, the time interval between images is 0.19 msec, equal to 16 degrees in one cycle. A complete cycle of pressure oscillation, beginning at maximum chamber pressure, is shown in Figures 4.12*d* through *z*.

Figures 4.12 *a* through *c* and Figures 4.12*aa* through *dd* are included so that the moments preceding the emergence of the vortex from the inlet section and following the end of the cycle, respectively, are shown as well.

What is immediately apparent from an examination of the images is the fact that there are two structures present in the duct during the period of one cycle as opposed to the single structure present for the chamber with the smaller expansion ratio. At maximum pressure, Figure 4.12*d* shows that the flow into the chamber is constricted in the vicinity of the dump plane. A fully-developed structure, whose leading edge is 12 cm downstream of the dump plane, is present in the duct at this time. Although the vortex emanating from the inlet to the chamber is the one on which to concentrate, it is also important to follow the motion of this fully-developed structure, for it represents the history of the shed structure after one cyclic period.

At 48 degrees after maximum chamber pressure, Figure 4.12*g*, a bump is noticeable in the fuel stream issuing from the dump plane and develops into a distinct vortex structure in subsequent frames. Just before the pressure in the chamber has reached its minimum value, Figure 4.12*o* at 176 degrees, one sees that the core of the most recently shed vortex has traveled 2.6 cm from the lip of the flame holder while the leading edge of the fully-developed structure, now present in the duct for 1.49 periods, is nearly 18 cm downstream of the dump plane. This structure has grown to the size of the depth of the chamber, and its shape is being altered by the presence of the lower wall, albeit to a far lesser extent than was the case for the duct whose expansion ratio is 4.0. It has also faded considerably indicating that combustion has been occurring throughout the vortex.

Now a fully-developed structure of its own, the most recently shed vortex has been in the chamber for 0.71 periods in Figure 4.12*t*. The leading edge of this vortex is 7 cm from the flame holder. All that remains of the previous structure is a small amount of residual combustion along the upper wall ahead of the fully-developed vortex. Note also

that the inlet flow to the chamber is becoming restricted as the pressure in the combustor nears its maximum.

At the end of the pressure cycle, Figure 4.12*z*, the leading edge of the vortex is 11 cm downstream of the lip of the rearward-facing step. A bulge in the upper portion of the leading edge is now evident indicating a sudden expansion of the fuel in the body of the structure. The vortex is igniting at this location, and the ignition mechanism must be the residual combustion along the upper wall remaining from the previous structure. The cycle is complete, and the remaining shadowgraph images, Figures 4.12*aa* through *dd*, show the beginnings of the next cycle.

Because the lower wall is further from the lip of the step for the configuration having an expansion ratio of 12.0, each vortex shed from the flame holder is able to achieve a greater degree of development and, therefore, is able to exist as a distinctive vortical structure for a length of time greater than one cyclic period as the above analysis has shown. This longer life span allows for the measurement of various physical properties of the vortices as functions of time. These include the width of the structure, X_w, the distance to the leading edge of the vortex, X_l and the distance to the trailing edge of the shed vortex, X_t. These quantities are shown schematically in Figure 4.13, and measurements were obtained for vortices shed during the five cycles shown in Figure 4.14. This figure contains the data traces of the pressure transducer and hot-wire anemometer at the dump plane as well as the photomultiplier readout at a location of 15 cm downstream of the dump plane.

Figures 4.15*a*, *b*, and *c* illustrate the linear relationships existing between the quantities X_w, X_l, and X_t, respectively, and time. This is in agreement with the numerical work of Hendricks (1986) in which a linear growth rate of the vortex was predicted throughout the early portion of the cycle. It is also worth noting that the vortex growth rates appear to be unaffected by the varying velocity and pressure amplitudes for the cycles considered. The slopes of the lines of Figures 4.15*b* relating the positions of the

leading edges of the vortices with time show that the structures are convected downstream at approximately 21 m/sec, the average dump plane velocity for these tests.

In either of the configurations considered, it is difficult to assess the degree of combustion or heat release occurring by merely examining the shadowgraph images. The changes in image illumination are proportional to the second derivative of density making the shadowgraph technique useful in analyzing small density gradients; however, as noted by Chomiak (1990), the zones of increased illumination cannot be clearly related to flame pattern, and it is the darker zones in the shadow that provide a representation of the disturbance geometry. Because of this, the method can be useful only in qualitative analyses.

There is some question as to whether the fine-scale structure evident in the images is actually part of the combusting vortex proper or merely residual burning clinging to the inner surfaces of the windows. Also, because combustion occurs at nearly uniform temperatures within the chamber, regions of burning may not appear in the shadowgraph images. Therefore, a comparison of the shadowgraph, showing density or temperature gradients, with a corresponding record of flame front position would be a marked step forward in understanding the ignition and combustion of the reacting vortex structures of pulse combustion. The following sections describe the methods developed to make such comparisons.

4.4 Ionization Probe Measurements

Ionization probes, previously discussed in Chapter Two, were incorporated into the experimental program in order to facilitate the study of the growth and motion of the combustion zone engulfing the shed vortex structures within the combustion chamber. The data from these probes are also useful in the examination of the shadowgraph images, for the data can be recorded along with a timing pulse signifying the capturing of a

shadowgraph image by the Polaroid camera. The images can then be deciphered with the aid of the ionization probe data trace. An example is given in the following figure.

4.4.1 Expansion Ratio of 4.0

Figure 4.16 contains a spark shadowgraph of the flow field for the 2.5-cm deep combustor along with the corresponding data record containing the traces of the pressure transducer, two ionization probes, and the photomultiplier. The ionization probes are located at 5 cm and 10 cm downstream of the dump plane and their sensors are 1.3 cm above the floor of the combustion chamber. The ceramic sheath of the probe closest to the step is clearly visible in the shadowgraph. The probe further downstream is hidden behind the support for the photomultiplier tube which obstructs a 0.6-cm wide slice of the field of view. The bottom data trace is that of the triggering pulse for the spark-gap light source. The leading edge of this pulse represents the instant when the shadowgraph image was obtained. In this case, this is at minimum combustion chamber pressure.

There are two points that can be readily made by examining the data record. The first is that there is a definite phase difference between the two signals from the ionization probes. As is to be expected, the flame front of the combusting vortex is detected at the upstream probe before detection occurs at the probe located further downstream of the dump plane. This difference in phase is equal to 50 degrees at the vortex shedding frequency of 185 Hz. For the probe separation distance of 5 cm, this gives a combustion wave velocity of 66.6 m/sec which is a value over three times as large as the mean dump plane velocity of 21 m/sec. The shadowgraph shows that the structure collides with the lower wall at a position between the locations of the two ionization probes, and material is thrust fore and aft of this point engulfing the probes. The resulting burst in reaction is quickly detected by the probes. The second point that is clear from the data is that the signals from the ionization probe and the photomultiplier tube, which are located at the same axial distance from the rearward-facing step, are in phase. It is very comforting, to

say the least, to find that the chemiluminescence, or heat release, is coinciding with the location of the combustion front and that the signal from the ionization probe, a very localized measurement, is representative of the combustion process occurring across the entire width of the chamber, for the photomultiplier signal is a line-of-sight measurement. The flow within the chamber, therefore, is behaving in a two-dimensional manner.

Although the ionization probes give point measurements, their signals are useful in the analysis of the shadowgraph images nonetheless. As mentioned, the shadowgraph of Figure 4.16 was obtained when the pressure in the duct was at its minimum value of approximately $0.86p_o$. At this time, a low level of combustion is occurring along the centerline of the combustion chamber 5 cm from the dump plane, as indicated by the slight rise in the probe voltage. The shadowgraph shows that the upstream probe is positioned along the underside of the cold-fuel stream, which appears as a bright streak in the image. Evidently, the fine-scale structure beneath the fuel stream surrounding the probe is not yet burning vigorously due to the weakness of the signal. The structure has encountered the lower wall at this instant, and negligible combustion is detected by the probe 10 cm downstream of the step at mid-height. The light intensity data show that intense combustion will occur shortly at this location. In fact, the burning will occupy a major portion of the duct because the signals from the two ionization probes overlap somewhat.

Figure 4.17 is a magnified portion of a typical data record for the smaller depth duct and will be used, along with the shadowgraph sequence of Figure 4.11, to explain the combustion process for the 2.5-cm deep chamber. Points *a*, *d*, . . ., *t*, and *w* in Figure 4.17 correspond to similarly lettered images in Figure 4.11.

The shadowgraph at the beginning of the sequence of Figure 4.11, Figure 4.11*a*, shows that as the pressure at the step begins to fall, a new structure forms at the lip of the rearward-facing step and begins to enter the combustion chamber. While the pressure continues to decrease during this portion of the cycle, points (*d*), (*f*), and (*i*), the two ionization probes detect very little combustion occurring on the centerline of the duct, and

the corresponding shadowgraphs reveal very little fine-scale structure indicative of combustion. Near minimum dump plane pressure and maximum dump plane velocity, points (*i*) and (*l*), the flow over the step is fully developed. A weak combustion front is detected first by the upstream ionization probe and, after a slight delay, by the probe furthest from the dump plane. The signature of this front is the small peak preceding the much larger and broader peak in the ionization probe traces, and is indicative of the passing of the front face of the vortex. The front passes the downstream measurement position 1.68 msec$\pm$160 μsec after encountering the upstream probe giving a front velocity of 27.6 m/sec to 33.4 m/sec, values slightly greater than the expected value of the average dump plane velocity of 21 m/sec.

It is believed that the ignition of the vortex structure is initiated at its front by the combustion residue of the previous structure lingering on the upper wall of the combustion chamber (Sterling 1987*a*, Keller 1987), and these data would support that conjecture. Once the leading edge of the structure passes, the level of combustion, as detected by the probes, decreases once again signifying the passage of the body of the vortex composed of unburned fuel. As the pressure begins to rise in the chamber, points (*o*), (*r*), and (*t*), one can see that the structure has collided with the lower wall. The shape of the structure has been destroyed and the levels of combustion begin to rise, as indicated by the upstream probe, point (*o*), and the downstream probe, point (*r*). The light intensity signal 10 cm from the dump plane is also rising. These data, along with their corresponding shadowgraph images, show that the collision of the structure with the lower wall has enhanced the mixing between the hot combustion products and the cold fuel stream resulting in a rapid burst in the levels of combustion and heat release. Finally, maximum pressure is attained at point (*w*), Figure 4.11*w*, and the cycle begins anew.

4.4.2 Expansion Ratio of 12.0

A single ionization probe is located on the centerline of the 7.6-cm deep chamber, 10 cm downstream of the dump plane and 3.8 cm above the floor in the shadowgraph of Figure 4.18. The corresponding pressure transducer and probe data records are given beneath the image as is the light source timing pulse. This shadowgraph, taken at nearly the positive-going zero-crossing in the pressure cycle, shows two vortices within the chamber. The most recently shed vortex is centered approximately 2.5 cm downstream of the dump plane while the fully-developed structure is positioned nearly 13 cm from the flame holder. This vortex has grown to occupy nearly the entire height of the chamber, and the ionization probe data trace shows that its tail contains a considerable amount of combusting fuel. The data record shows the very periodic burning taking place at the probe position at a frequency of 235 Hz. In contrast to the smaller depth chamber where the heat release was in phase with the pressure at the lip of the step at a position of 10 cm from the dump plane, one can see that for the deeper chamber the ionization probe and pressure signals are 68 degrees out of phase at 235 Hz at the same axial location. This corresponds to a length of time of 0.80 msec or 0.19 periods of oscillation at 235 Hz.

The greater height of the 7.6-cm deep chamber allowed for a number of flame front position profiles to be acquired at several levels above the chamber floor by an array of ionization probes situated 5 cm, 10 cm, 15 cm, and 20 cm from the dump plane. Each probe was inserted through a port in the floor of the combustion chamber and the spacing of 5 cm was chosen to minimize the disturbance to the flow. The incidences of regions of combustion contacting the probes were recorded at six different heights above the lower wall of the combustor and the results are given in Figures 4-19*a* through *f*. Each individual data set contains the pressure response at the dump plane along with the signals from the four ion gauges whose sensors are positioned at the same level in the chamber. The probes in the first data set, Figure 4-19*a*, are located 7 cm above the floor. For each

successive record, the probes are lowered 1.3 cm until they are 0.6 cm above the lower wall in the last data set, Figure 4-19*f*.

Several observations concerning the combustion of the vortex structures shed from the rearward-facing step flame holder in the 7.6-cm deep chamber can be made after examining these data. First, the intensity of the combustion appears to be greatest in the upper half of the chamber because the magnitudes of the ionization probe signals are larger in this region. A significant decrease in signal amplitude occurs as the probes are lowered from 3.2 cm to 0.6 cm above the floor signifying a decrease in the level of combustion at these positions. In fact, very little activity is apparent in the last data set, Figure 4.19*f*, at any probe level. One would expect, after examining these results, that the vortex structures are not interacting with the lower wall as strongly in the deeper chamber as they were in the case of the 2.5-cm deep chamber where the lower wall influenced the development and burning of the structures a great deal. The shadowgraph sequence of Figure 4.12 shows quite plainly that this is indeed the case for the first 30 cm downstream of the dump plane, for the vortex barely comes into contact with the floor of the duct.

Next, one notes that the probes located 10 cm and 15 cm from the step generally record both the greatest amount of combustion and the strongest combustion activity at any of the positions above the lower wall, particularly at the 5.7 cm and 4.4 cm levels as shown in Figures 4.19*b* and *c*, respectively. Because the shadowgraph sequence of Figure 4.12 shows that the vortex structure consists of many fine-scale elements in this region, it can be concluded that these elements are indicative of combustion activity and that most of this activity is occurring 10 cm to 15 cm from the dump plane. An analysis of the signals from the gauges axially located 5 cm and 20 cm from the rearward-facing step flame holder supports these findings, for they consistently record the least amount of combustion activity or flame front presence at any location above the floor.

The probe nearest the dump plane is most active at the highest level above the floor, just 0.6 cm from the upper wall of the chamber as shown in Figure 4.19*a*. It is felt

that this is primarily due to the residual combustion from the previous structure that remains along the upper wall and serves as the ignition source for the following vortex. Fine-scale elements are visible in this area in Figure 4.12 as well, providing further evidence of combustion taking place here. The recording of the presence of combustion by this probe at the other higher levels may be due to a low degree of burning taking place in either the core of the newly shed structure or along its front face. The signal from the most downstream probe, 20 cm from the dump plane, is the strongest at 4.4 cm above the lower wall, as shown in Figure 4.19*c*, and very intermittent elsewhere. The data suggest, therefore, that the bulk of the combustion has been completed before the structure has reached this downstream location.

Ionization probes have proven to be useful tools in the study of the reacting vortex structures associated with the laboratory dump combustor. Their results, in conjunction with the shadowgraph images of the flow fields, have shown that the two chamber configurations exhibit different combustion profiles during operation in that the majority of the burning takes place further downstream of the dump plane as the lower wall is moved further below the lip of the flame holder. One drawback, however, is the fact that the probes provide only a very localized measurement of the combustion activity. Although it has been shown for the smaller depth chamber that this local measurement is indicative of what is occurring across the width of the chamber at the same downstream location, it is still a point measurement and the level of combustion in the region surrounding the probe can only be conjectured about. An image of the chemiluminescence, similar to those of the density or temperature gradients obtained by shadowgraph imaging, is needed to completely understand the nature of the heat release of the entire flow field. These images have been obtained and will be discussed next.

4.5 Chemiluminescence Images

Chemiluminescence imaging is a widely used technique for qualitatively determining the heat release from a reacting flow field. In the field of pulsating combustion, favorable results have been obtained by numerous experimenters, Keller *et al.* (1991), Samaniego *et al.* (1991), Tang *et al.* (1991), and Zsak *et al.* (1991) to name a few, who have employed a solid-state intensified imaging camera in their studies. Typically, however, low-frequency, single-mode oscillations, on the order of 50 Hz to 60 Hz, have been examined. Having a single excited acoustic mode allows phase-locking of the captured light intensity images to be performed with relative ease due to the small amount of cycle-to-cycle variation present during operation. Similarly, comparison of these chemiluminescence images with those obtained using the shadowgraph technique, albeit acquired during different experimental runs, provides a complete visual representation of the reacting flow field. When there are multiple acoustic modes excited as in this investigation, phase-locking of the imaging systems is not a trivial matter due to the fact that the beating which occurs between the excited modes affects the period of each cycle so that cycle-to-cycle variations can take place. Taking this into account, a method has been developed in which the two images, one acquired with the intensified CID camera and the other obtained with the shadowgraph system, have been captured, for all intents and purposes, simultaneously so that true, direct comparisons can be made between the images obtained by the two techniques. The 'simultaneous' acquisition of a shadowgraph and a corresponding image of the chemiluminescence has been described in Chapter Two in the section pertaining to the GE TN2505A intensified camera. One is reminded that the images are actually taken approximately 15 μsec apart from one another, or in other words, there is a delay of nearly 1.5 degrees between the two. This is considered a negligible length of time when compared to the period of one cycle.

4.5.1 Expansion Ratio of 4.0, Short Exposure Images

Typical examples of the images acquired by the two flow visualization methods for the 2.5-cm deep combustion chamber are shown in Figures 4.20 and 4.21. Two components comprise the figures. They are the shadowgraph image (*a*) and the color-enhanced image of the chemiluminescence (*b*). The field of view of the shadowgraph is limited by the diameters of the spherical mirrors used in the optical configuration to the first 14 cm downstream of the flame holder. The intensified camera, on the other hand, was able to include the first 16.5 cm of the combustion chamber as measured from the dump plane. The dark tic marks along the lower wall of the chamber in each shadowgraph are placed 2.5 cm apart and coincide with the tics along the lower wall of the chamber in the chemiluminescence image. Once again, pixel values range from 0 to 255 for the intensified camera images, and the color bar shown in each image (*b*) has been selected to provide the greatest contrast in intensities. The exposure time of the light intensity images is 60 μsec.

The images of Figure 4.20 were obtained 81 degrees after maximum pressure was attained in the combustion chamber. For a shedding frequency of 185 Hz, this is equivalent to a time of 1.22 msec or 0.23 periods of oscillation. The shadowgraph of Figure 4.20*a* reveals a single vortex whose leading edge is approximately 3.4 cm downstream of the dump plane. Note the smoothness of the cold fuel stream and the fine-scale structures inhabiting the core of the vortex and prevalent along the tail as well. The remnants of the previous vortex are seen to linger along the upper wall of the chamber roughly 10 cm from the lip of the step flame holder.

The chemiluminescence image of Figure 4.20*b* shows that the fine-scale structure is indeed combusting material. The core of the shed vortex, for example, is seen to be emitting nearly all of the visible radiation. Why is this the case? The tail of the vortex contains fuel that has been in the chamber for the longest time; therefore, it has had the longest time to react with the combusting material of the previous vortex that propagated

upstream beyond the dump plane as well as with the hot products of combustion in the recirculation zone of the chamber. As the shed vortex developed, this material was swept around by the motion of the structure until it became trapped in the vortical core. A very small and less intense amount of combustion is occurring along the outer edge of the structure, as denoted by the green color along this edge, while combustion of a slightly greater intensity is occurring in the remnant material of the previous cycle downstream. The small area of combustion activity centered 4.2 cm from the dump plane along the lower wall corresponds to the fine-scale structure appearing in the same location in the shadowgraph image- an interesting point.

A second example of the simultaneous shadowgraph/chemiluminescence image technique for the chamber with an expansion ratio of 4.0 is given in Figure 4.21. The images were obtained at a phase of 142 degrees after maximum chamber pressure. This corresponds to 2.13 msec or 0.39 periods of the 185 Hz oscillation. The flow field is quite different than that of the previous figure.

The shadowgraph image of Figure 4.21*a* shows that the vortex has been immensely elongated due to the presence of the lower wall of the chamber. The leading edge is seen to be positioned beyond the 14-cm field of view, and the tail of the vortex is centered at 2.5 cm downstream of the dump plane. The fine-scale indicative of combustion is seen to permeate the visible area of the combustion chamber, especially in the area lying 10 cm from the step and beyond. A significant amount of fine-scale structure lies along both the lower and upper walls of the chamber. These elements reach upstream beyond the dump plane as well.

The corresponding image of the chemiluminescence is shown in Figure 4.21*b*. Intense combustion occurs throughout the entire 16.5-cm long and 7.6-cm deep visible portion of the duct, with the strongest activity occurring near the impingement point of the vortex with the lower wall between 9 cm and 14 cm from the dump plane. A less intense region of combustion is located in the center of the duct stretching from 5 cm to 8.3 cm

from the step. This area appears as a uniform region in the shadowgraph of Figure 4.21*a*. An important point to note is the combustion activity propagating upstream beyond the lip of the flame holder, clearly evident in Figure 4.21*b*. It is this material which reacts with the lead material of the next structure beginning the ignition process of the vortex.

A number of short exposure images of the chemiluminescence of the reacting vortex structures of the 2.5-cm deep chamber were obtained. A sampling of four is given in Figure 4.22. Here, contour plots of the pixel values are given rather than the color-enhanced images. The contour levels are at the pixel values of 30, 80, 130, 180, 220, and 250.

The first image, (*a*), was taken 11 degrees after the pressure in the combustor reached its maximum value. This corresponds to 0.17 msec or 0.03 periods of oscillation of the 185-Hz shedding mode. The bulk of the light intensity is seen to radiate from the previous structure which is centered roughly 9 cm downstream of the dump plane. A new structure is rolling from the lip of the step, and the leading edge of this vortex is impinging against combusting material contained in the tail of the previous structure. The second image, Figure 4.22*b*, shows the radiation in the chamber 26 degrees after maximum pressure. This is equivalent to 0.39 msec or 0.07 periods of oscillation. The leading edge of the shed vortex structure is located approximately 2 cm downstream of the dump plane, and a significant amount of combustion is seen to exist within the visible length of the chamber from the previous structure. Next, Figure 4.22*c* shows an image which was obtained at a phase of 209 degrees after maximum pressure was attained, corresponding to 3.14 msec or 0.58 periods of oscillation. The unburned fuel stream forms a distinct ring, much larger than that of Figure 4.20*a*, and traps combusting material within its center. The leading edge of this structure is located at an axial position of 5 cm. A significant amount of combustion occurs along the upper portion of the leading edge of this vortex, initiated by the residual combustion in the tail of the previous structure. Finally, Figure 4.22*d* presents an image of the chemiluminescence taken 349 degrees in the

cycle from maximum pressure. This is equal to 5.24 msec or 0.97 periods. A high level of combustion fills the duct and is beginning to move downstream, for the trailing edge of the combusting region is approximately 1 cm from the dump plane.

Even though it is apparent that cycle-to-cycle variations are occurring in the burning of the structures, these images illustrate the various degrees of reaction of the vortex structures associated with the smaller depth chamber. Figures 4.23*a*, *b*, and *c* give the average light intensity of Figures 4.22*a*, *b*, and *c*, respectively, as a function of axial position. The average light intensity at a particular axial location is obtained by adding the values of the pixels over the entire depth of the chamber and dividing the sum by the total number of pixels contained in that column. These plots give the heat release as a function of axial position at a particular phase of the pressure cycle owing to the linear relationship between heat release and intensity of emitted visible radiation.

4.5.2 Expansion Ratio of 12.0, Short Exposure Images

Striking differences are apparent for the deeper combustion chamber. Figure 4.24*a* shows a vortex centered approximately 4 cm from the rearward-facing step flame holder and another, fully-developed structure is located 13 cm downstream of the step. The two structures have been in the duct for 2.40 msec and 6.48 msec, respectively, as measured from the minimum of the hot-wire anemometer signal. Here, 2.40 msec corresponds to 0.56 periods of oscillation or 203 degrees and 6.48 msec corresponds to 1.52 periods of oscillation or 548 degrees. Owing to the very small time delay between the capturing of the two images, a direct comparison can be made between the shadowgraph, (a), and the image of the chemiluminescence, (b).

A comparison of the two images reveals that a negligible amount of light is being emitted from the most recently shed vortex, whereas the fully-developed structure exhibits a much larger intensity which is interpreted as a much larger heat release per unit volume. This suggests that a very low level of combustion occurs near the lip of the step for the

7.6-cm deep chamber in contrast to the case for the 2.5-cm deep chamber where the flame actually propagates upstream over the step. The greatest amount of heat release appears to be located in the upper right quadrant of the structure as indicated by the yellow to white colorization of this area. Unfortunately, most of this region is out of view in the shadowgraph. Interestingly, the intensity of the emitted light abruptly rises along the upper wall at a distance of a little less than 7 cm from the step. As the shadowgraph shows, this location is the interface between the tail of the developed vortex and the leading edge of the structure entering the combustion chamber. It has been stated that the tail of the developed vortex serves as the ignition source for the next incoming structure, and these images clearly illustrate this thought.

The next figure, Figure 4.25, contains images of a vortex whose development lies between those shown in the previous figure. This structure was shed 4.08 msec before the images were captured and is centered at 6.5 cm from the dump plane. The time of 4.08 msec is equivalent to 0.96 periods of oscillation or 345 degrees. One can note the unburned fuel stream evident in the shadowgraph (*a*). The image of the light intensity (*b*) clearly outlines the cold-fuel stream. A small amount of combustion is occurring in the core of the vortex resulting from the entrapment of hot products of combustion by the fuel stream as it issues from the inlet of the chamber and begins to form the vortex structure. The most intense combustion activity is taking place in the region along the upper wall where the front of the vortex has come into contact with the tail of the preceding structure which is beginning to burn out. Again, this is the primary ignition point.

A sequence of intensified camera snap-shots illustrating the progression of combustion through the vortex structure for the 7.6-cm deep combustor is given in Figure 4.26, where the exposure time of the images is now 36 μsec. The time interval between the images is not constant; therefore, each image contains the respective lengths of time that the vortices have been in the duct. The field of view has been expanded to include the first 30 cm downstream of the dump plane. Contour plots of the pixel values have been

used, and the contours are at the levels 30, 80, 130, 180, 220, and 250. Once again, the tic marks at the base of the duct are spaced in 2.5-cm increments.

Looking at the figure, one sees that as the well-developed vortex furthest from the dump plane begins to burn out, the structure nearest to the step begins to ignite, primarily on the upper portion of its leading edge. The ignition of the most recently shed vortex is clearly shown in Figure 4.26*c* where the most intense heat release is occurring along the upper edge of the structure. This combustion is swept around the vortex, as in Figure 4.26*d*, until finally the entire structure is burning, Figures 4.26*e* and *f*.

Figure 4.27 shows the average light intensity over the entire height of the duct as a function of the axial distance from the dump plane for each of the images of the previous figure. The lengths of time in degrees that the vortices have been in the chamber, as measured from the hot-wire anemometer traces, are also shown within each plot. The burning out of the fully-developed vortex structure is evident in Figures 4.27*a* through *c*. Here, the large peak in light intensity associated with this structure, initially centered at roughly 13 cm from the step, decreases in magnitude and broadens as it moves downstream with increasing time. As this is occurring, the light intensity radiating from the newly shed vortex begins to increase in amplitude and move further from the step. Ignition is shown to occur nearly 4.4 cm downstream of the dump plane in Figure 4.27*c*. As the development of the vortex continues, its associated chemiluminescence becomes larger as well, reaching a maximum nearly 15 cm downstream as was the case for the previous structure. Overall, the greatest light intensity readings, and hence the largest heat releases per unit volume, are obtained from structures that have been shed from 5.12 msec to 7.60 msec before the triggering of the images occurred. This is equivalent to 1.18 to 1.75 times the length of one period of the 235-Hz mode.

A comparison of Figures 4.23 and 4.27 reveals that the bulk of the heat release takes place at different locations for the two chamber configurations. The combustion activity occurs much closer to the step for the 2.5-cm deep chamber and further

downstream for the 7.6-cm deep duct. To illustrate this difference, a number of long-time exposure images, equal to 5 msec, were taken of the chemiluminescence for the two cases. From these, one can obtain the distribution of the heat release over the first 30 cm of the combustion chamber.

4.5.3 Expansion Ratio of 4.0, Long Exposure Images

Three contour plots of the light intensity for the 2.5-cm deep chamber are given in Figure 4.28 as examples of the 'long' exposure images of the chemiluminescence. The contours are at the levels 30, 80, 130, 180, 220, and 250. The distributions are significantly different for the two chamber depths. The majority of the combustion occurs much closer to the dump plane and extends roughly 15 cm downstream of the step for the 2.5-cm deep chamber. It is also noted that the combustion activity occupies the entire height of the duct in this region and even propagates upstream beyond the lip of the step. Because the combustion reaches upstream of the dump plane, the ignition of the shed vortices can begin earlier in their histories, giving the burning of the structures a 'head start', so to speak, as they enter the combustion chamber. Recall that the shadowgraph sequence of Figure 4.11 showed that the shed vortex structure travels only a few centimeters downstream of the dump plane before it impinges on the lower wall. As has been already stated, it is believed that this collision enhances the mixing between the hot products and the cold fluid leading to a burst in heat release. The long-time exposure images of the chemiluminescence have shown that this burst in combustion is confined to the first 15 cm of the combustion chamber for this configuration.

4.5.4 Expansion Ratio of 12.0, Long Exposure Images

The lower wall has less of an effect on the combustion of the vortex structures for the deeper depth configuration because it is further below the inlet lip. The bulk of the combustion, as seen in the contour plots of Figure 4.29, occurs much further downstream

of the dump plane. Once again, the contour levels are 30, 80, 130, 180, 220, and 250. The combustion neither occupies the entire height of the chamber nor propagates upstream of the dump plane as it does in the 2.5-cm deep chamber. Also, the evidence presented has given no indication that a collision by the vortex with the floor of the duct is as important to the combustion process occurring in the 7.6-cm chamber as it is in the smaller depth chamber. Lack of a strong influence by the lower wall of the deeper chamber on the histories of the structures as they propagate downstream is one of the major differences between the characteristics of the two combustor configurations detailed in this study. Another important point of difference is the upstream propagation of the combustion over the lip of the rearward-facing step flame holder which is quite apparent for the smaller depth chamber. As previously mentioned, this propagation of the combustion upstream beyond the dump plane serves as an ignition source for the vortices of the 2.5-cm deep chamber.

As different as the two combustion processes are, as shown in the previous figures, one would expect the total heat release per unit volume for either configuration to be equal because the combustor inlet conditions are the same. Averaging the pixel intensities for the long-time exposure images of each of the chamber depths and plotting the results as light intensity versus distance from the dump plane gives the curves shown in Figure 4.30. Integration of the curve for the 2.5-cm deep chamber gives an area of 998 cm while the 7.6-cm curve yields a value of 970 cm, a difference of just under 3%. This result validates the interpretation of the proportionality between the chemiluminescence and the heat release rate.

4.6 Temperature Measurements

As the results of the previous sections have shown, there is quite a difference in the heat release profiles of the combustion chamber for the two duct configurations as well as in the mechanisms of ignition of the reacting vortex structures. The measurements of the

ionization probes and the images from the intensified camera have qualitatively revealed aspects of the combustion processes which have previously gone unnoticed. This section describes an attempt to quantify these aspects through fine-wire thermocouple measurements at various locations throughout the 2.5-cm and 7.6-cm deep combustion chambers because it is believed that the ignition of the vortex structures and their time histories are dependent upon the temperature of the hot products of combustion within the dump combustor.

The R-type thermocouples described in Chapter Two have been employed to extract temperature information from the reacting flow. The sensors have been placed along the centerline of the lower wall in the same ports that were used for the ionization probes, and readings were taken at various elevations above the floor of the chamber. Additional access ports were machined into the front face of the rearward-facing step flame holder in order to obtain temperature measurements near the dump plane. As noted in the second chapter, the response times of the thermocouples used in this investigation are of the same order as the periods of the vortex shedding frequencies for the two chamber depths. Because of this limitation, fluctuations in temperature could not be determined accurately. The results presented here, therefore, are of mean temperatures only.

4.6.1 Expansion Ratio of 4.0

It has been shown that the greatest amount of combustion activity occurs within the first several centimeters downstream of the dump plane for the 2.5-cm deep chamber. Temperature measurements were made, therefore, at axial positions 1.4 cm, 5 cm, and 10 cm from the step flame holder. Those measurements made at the 5 cm and 10 cm locations include readings at four elevations above the lower wall of the duct, namely at 0.3 cm, 0.6 cm, 1.3 cm, and 1.9 cm, so that variations in temperature over the height of the duct could be discerned. The measurements made 1.4 cm downstream of the step

were performed at a single elevation of 1 cm above the floor. This is as close to the lip of the step, located 1.9 cm above the lower wall, as could be reached by the thermocouples.

Figure 4-31*a* contains sample temperature readings, not corrected for radiation losses, recorded 5 cm downstream of the dump plane at the four levels above the floor of the chamber. The measurement of the probe located 1.4 cm from the step and 1 cm above the lower wall is also included in this figure. Temperature measurements at the four heights above the floor recorded 10 cm axially from the step are shown in Figure 4.30*b*. These plots show that the coolest temperatures within the duct are found near the lower wall of the combustor at both the 5 cm and 10 cm axial measurement positions suggesting a quenching effect by the water-cooled floor. The temperature near the floor is roughly 1530 °K at the 5 cm axial position and approximately 1645 °K at the furthest downstream measurement position. Figure 4.31*a* also shows that the temperature near the upper water-cooled wall is only slightly above that near the floor while the profiles at the 0.6 cm and 1.3 cm elevations are some 200 °K greater. The measurement position nearest the dump plane recorded the highest temperatures shown in this figure, averaging approximately 1840 °K.

For the measurement location further downstream at 10 cm, a more uniform temperature profile was found to exist between the 0.6 cm, 1.3 cm, and 1.9 cm elevation levels. This is not surprising because flow visualization has shown the mixing of the fresh reactants with the hot products of combustion to be the most vigorous in the vicinity of the point of impact between the shed vortex and the lower wall. The point of impact is nearly at this axial measurement location. The long-time exposure intensified images of the chemiluminescence, Figure 4.28, have also shown a uniformity of the heat release in this area as well. Here, the mean temperature is roughly 1830 °K $\pm$ 30 °K, a value similar to that obtained nearest the dump plane. Because it has been shown that the combustion propagates upstream beyond the lip of the rearward-facing step, a high temperature reading near the dump plane should be expected.

4.6.2 Expansion Ratio of 12.0

The temperature measurements for the 7.6-cm deep chamber are given in Figures 4.32*a* though *f*. A more extensive investigation was undertaken for this chamber configuration due to the concentration of the heat release downstream of the dump plane, as shown in Figure 4.29, as well as the fact that the greater chamber depth allowed access to a wider variety of measurement locations. It should be noted that the lengths of the thermocouple probes were such that only the lower half of the combustion chamber, up to an elevation of 3.8 cm above the floor, could be examined. There are no access ports for probes along the upper wall of the laboratory dump combustor. The first figure, 4.32*a*, contains temperature measurements made within the recirculation zone just downstream of the dump plane. Successive figures, Figures 4.32*b* through *f*, contain measurements at different elevations above the lower wall for axial positions from 5 cm to 25 cm from the step in increments of 5 cm, respectively.

Examining Figure 4.32*a*, one sees that the lowest recorded temperature readings are made by the probe positioned just under the lip of the step 1.3 cm downstream of the dump plane. Here, the mean temperature is a relatively cool 1230 °K. The four other temperature traces shown in this figure are from thermocouples positioned at the same vertical height of 1.6 cm above the floor but having axial positions of 0.3 cm, 1.3 cm, 2.5 cm, and 3.8 cm from the face of the flame holder. At this level above the lower wall, one sees that the temperature increases from nearly 1290 °K to 1850 °K as the distance from the dump plane increases. Evidently, the recirculation zone in the region near the flame holder is much cooler for this particular combustion chamber configuration than for the smaller depth chamber. This is a conclusion supported by the images of the heat release made by the intensified camera.

The next figure, Figure 4.32*b*, contains temperature measurements 5 cm downstream of the dump plane at 0.3 cm, 1.3 cm, 2.5 cm, and 3.8 cm above the lower wall. This region is well within the recirculation zone of the hot combustion products, as

deduced from the flow visualization images. As was the case for the smaller depth chamber, the lowest temperature readings are found at the lower wall and are comparable to the 2.5-cm deep chamber values. Interestingly, of the three remaining levels, the temperature is found to decrease from 1820 °K at 1.3 cm above the floor to 1640 °K at mid-height, 3.8 cm from the lower wall. The means that the path of the combustion products within the recirculation zone lies primarily in the bottom third of the combustion chamber.

One would expect the temperature readings to increase as the probes are moved downstream to the next several access ports judging from the results of the chemiluminescence imaging, and indeed Figures 4.32*c* and *d* show that there is an elevation in the temperature of the lower half of the chamber at the 10 cm and 15 cm axial positions. A faulty wire connection in the thermocouple positioned 10 cm downstream of the dump plane and 1.3 cm above the floor caused a great deal of scatter in the temperature data for this position in Figure 4.32*c*. The grossly incorrect data points have been omitted from the figure. The centerline temperature, 3.8 cm above the floor, has increased dramatically to a value of 1930 °K at the 15 cm location. The temperature readings remain fairly constant at the elevations of 2.5 cm and 3.8 cm even as the thermocouples are placed 20 cm and 25 cm downstream of the dump plane, as shown in Figures 4.32*e* and *f*, respectively. A significant drop in temperature has occurred along the lower wall, however. One sees from Figure 4.32*f* that the temperature has fallen to approximately 750 °K near the floor, 25 cm from the dump plane.

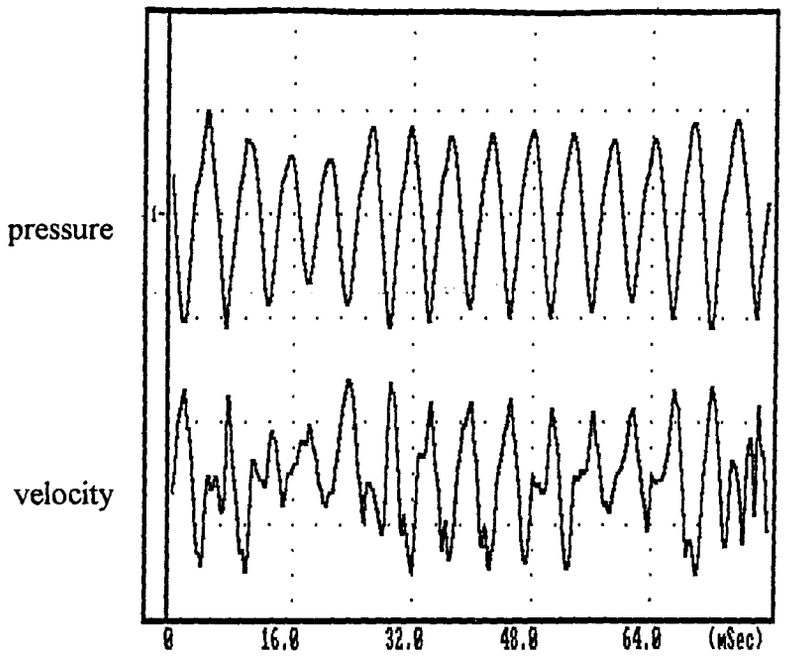

(*a*)

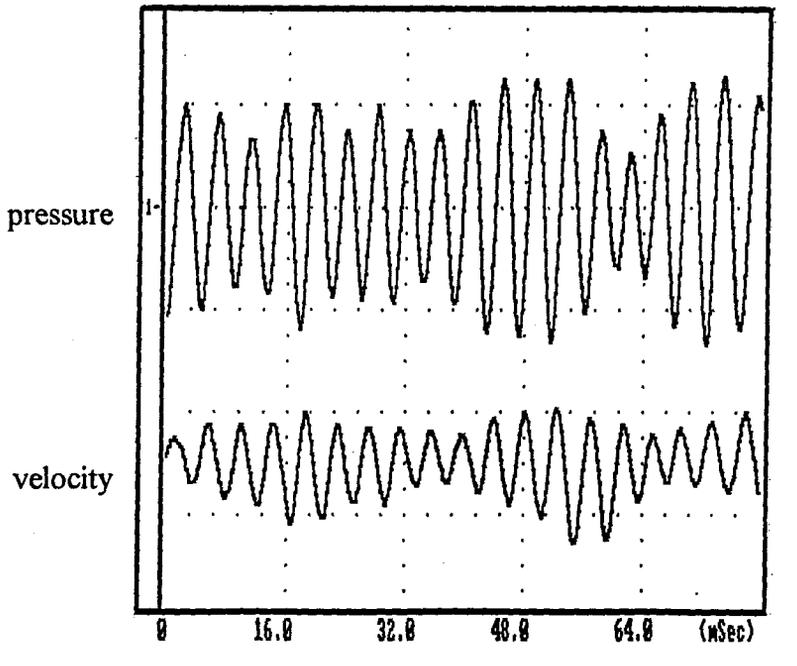

(*b*)

Figure 4.1: Sample raw data traces for (*a*) chamber with expansion ratio of 4.0 and (*b*) chamber with expansion ratio of 12.0.

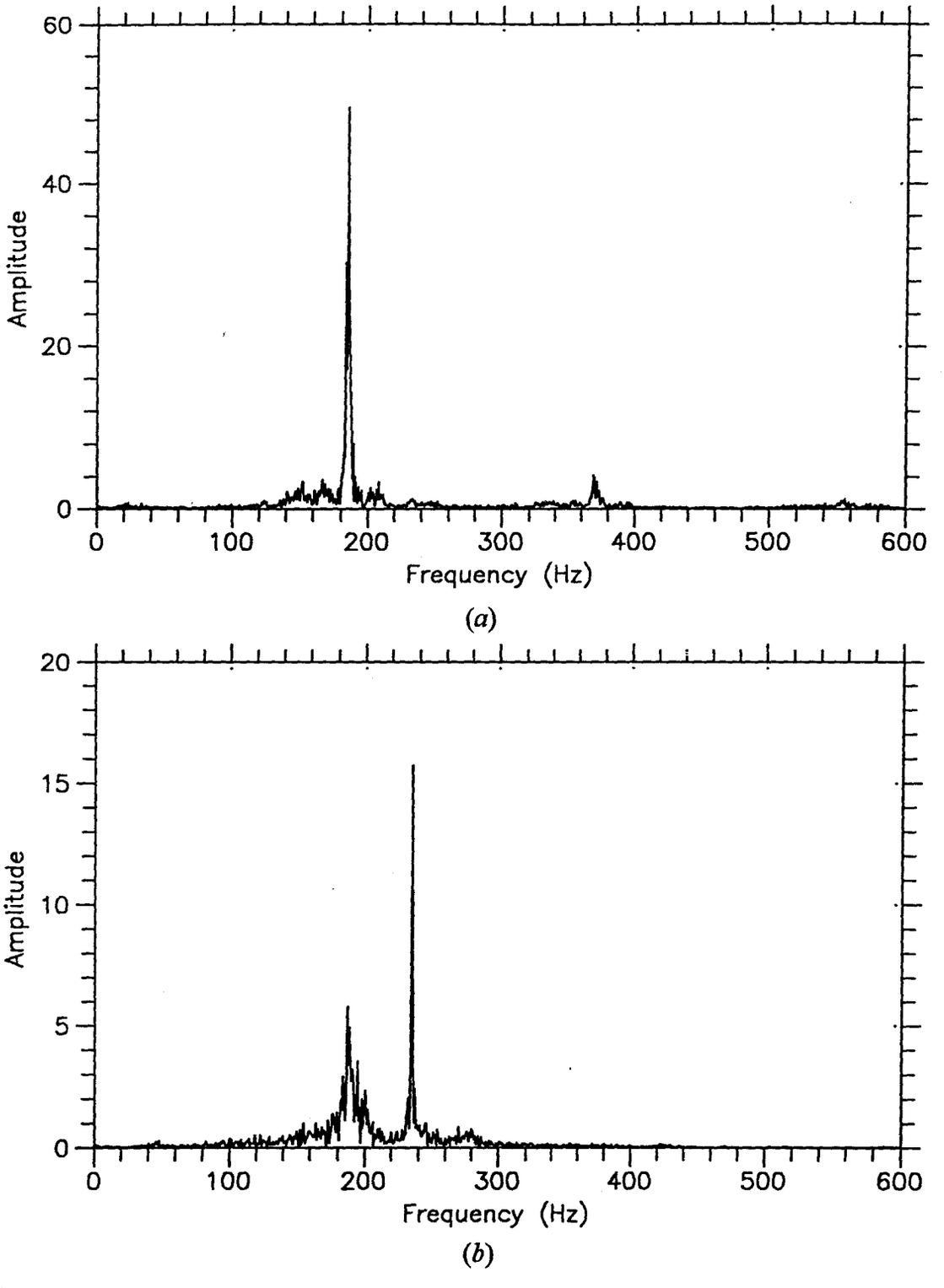

Figure 4.2: Experimental pressure amplitude spectra for (*a*) chamber with expansion ratio of 4.0 and (*b*) chamber with expansion ratio of 12.0.

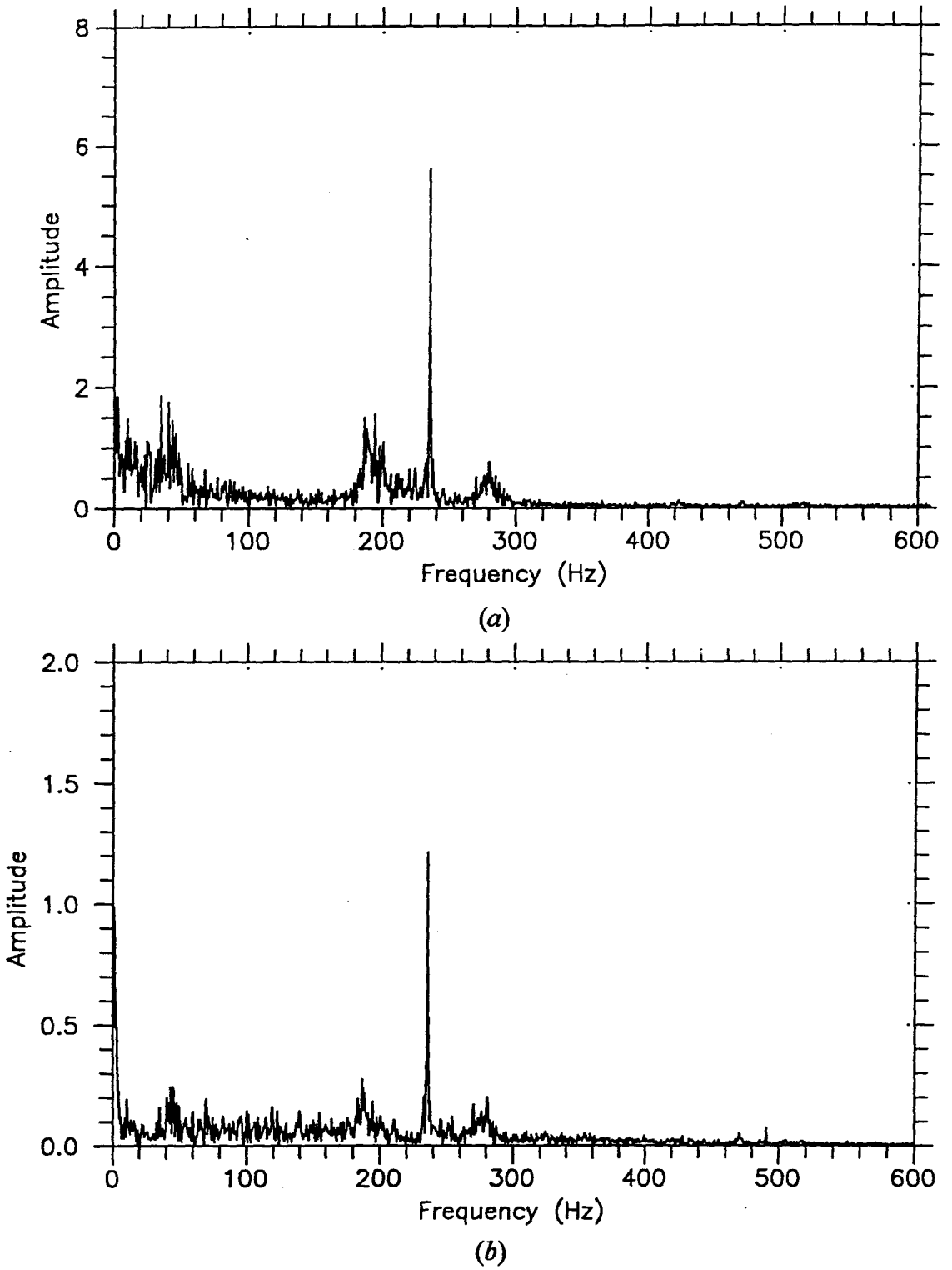

Figure 4.3: Experimental (*a*) velocity and (*b*) total light intensity amplitude spectra for chamber with expansion ratio of 12.0.

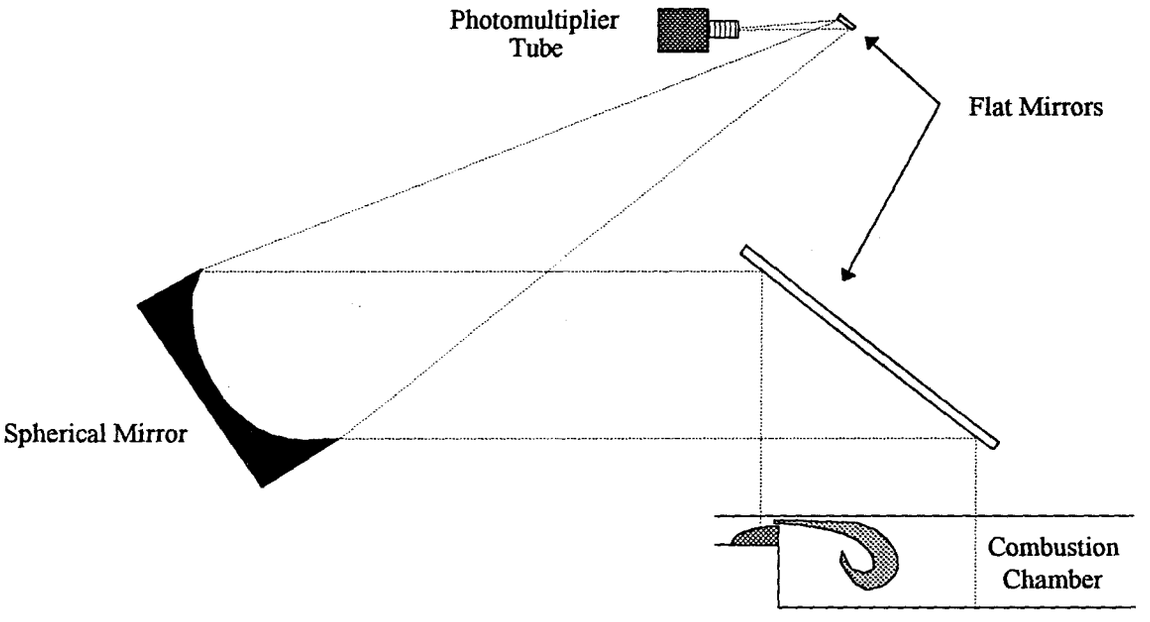

Figure 4.4: Optical arrangement for total light intensity measurement.

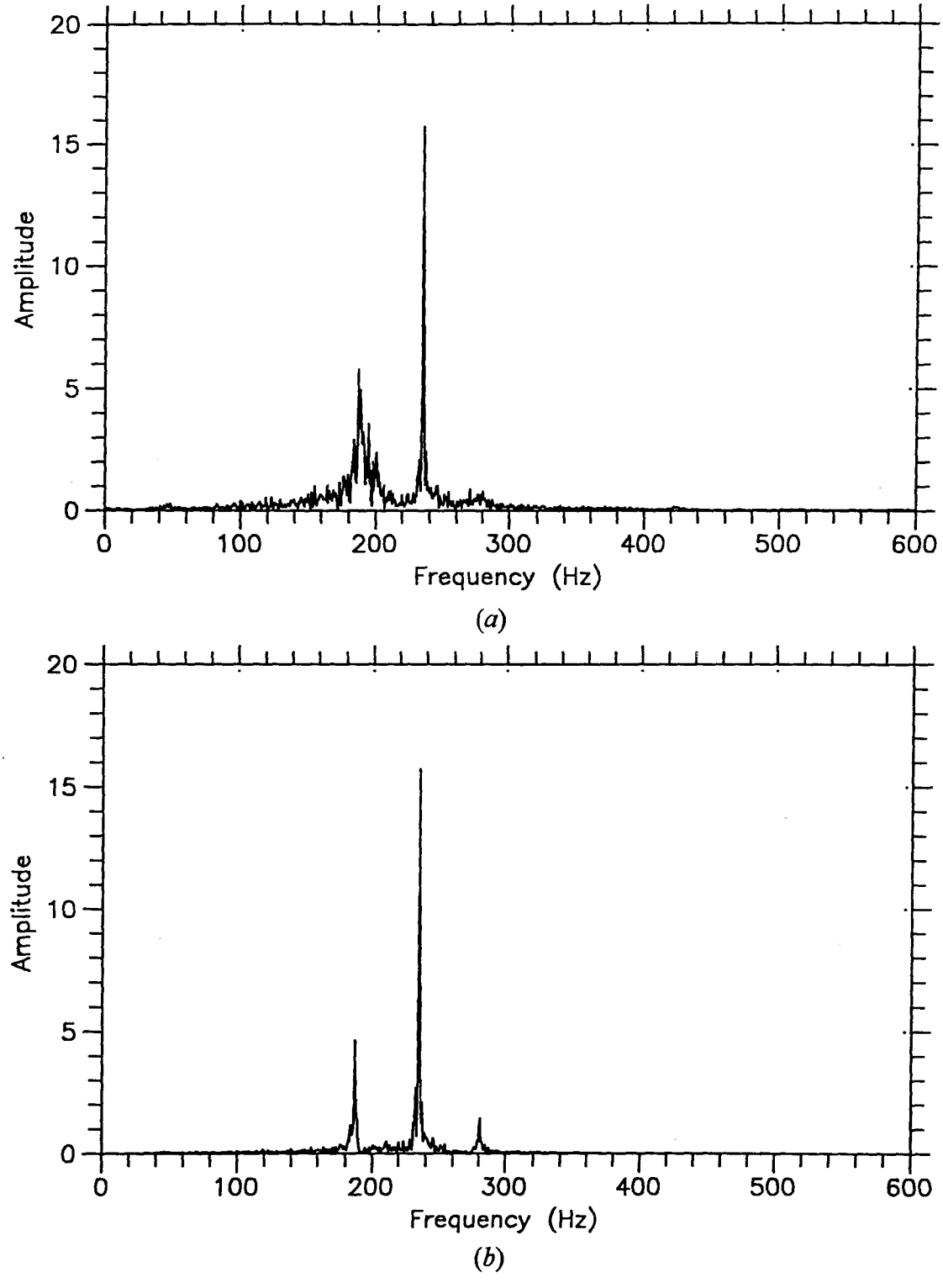

Figure 4.5: Comparison of (*a*) experimental and (*b*) predicted pressure amplitude spectra for chamber with expansion ratio of 12.0.

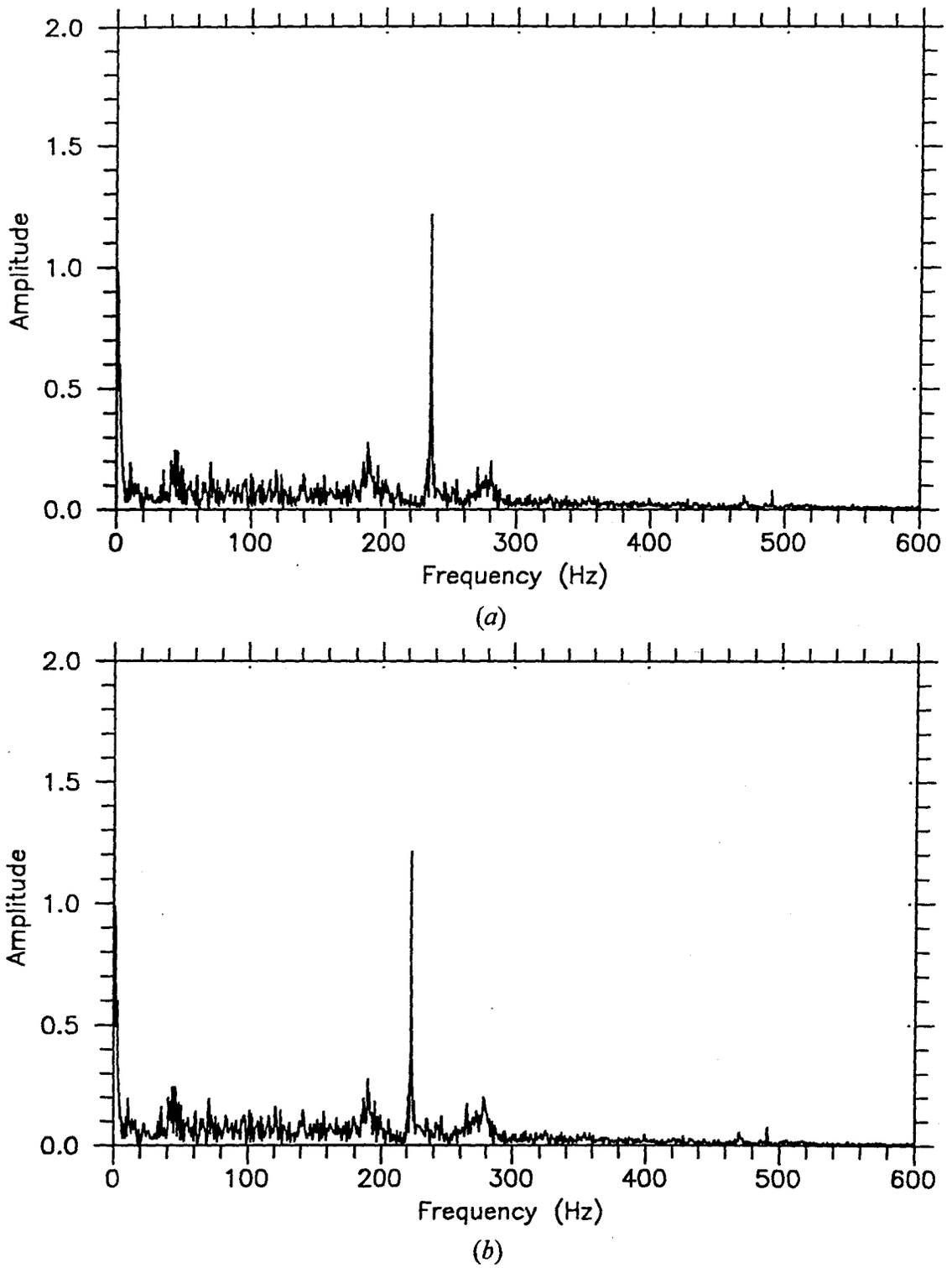

Figure 4.6: Comparison of (*a*) actual experimental and (*b*) frequency-shifted driving amplitude spectra for chamber with expansion ratio of 12.0.

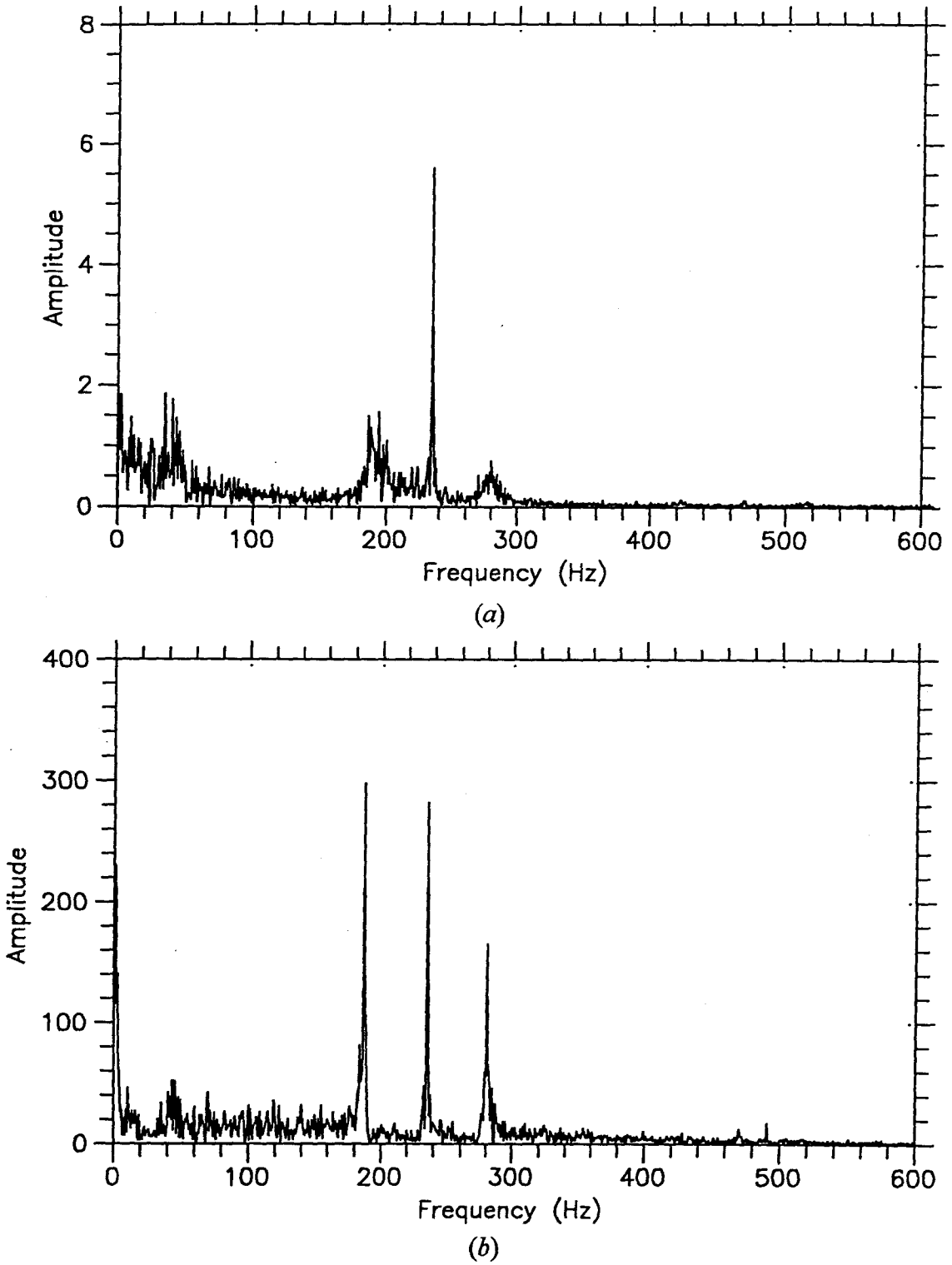

Figure 4.7: Comparison of (*a*) experimental and (*b*) predicted velocity amplitude spectra for chamber with expansion ratio of 12.0.

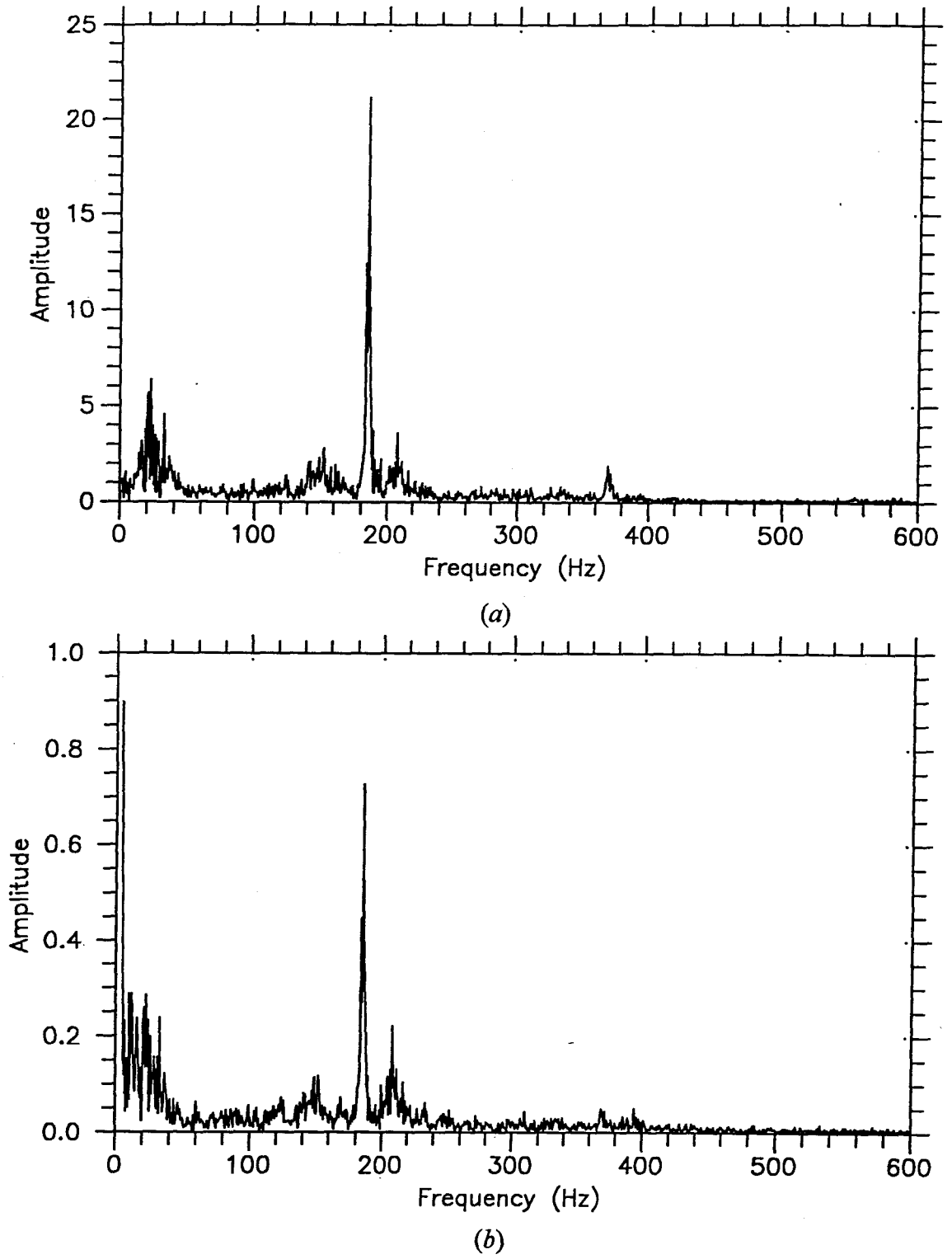

Figure 4.8: Experimental (*a*) velocity and (*b*) total light intensity amplitude spectra for chamber with expansion ratio of 4.0.

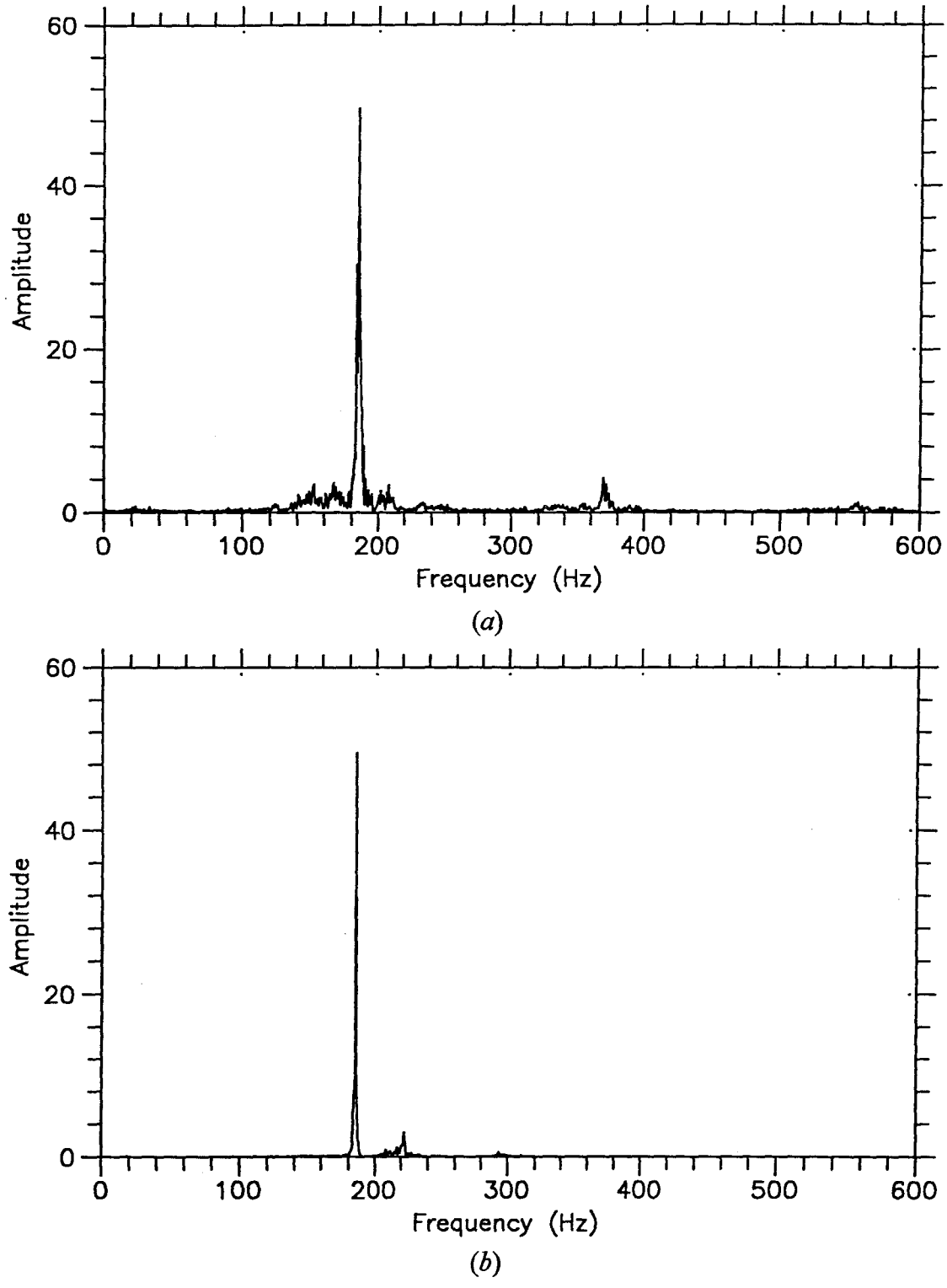

Figure 4.9: Comparison of (*a*) experimental and (*b*) predicted pressure amplitude spectra for chamber with expansion ratio of 4.0.

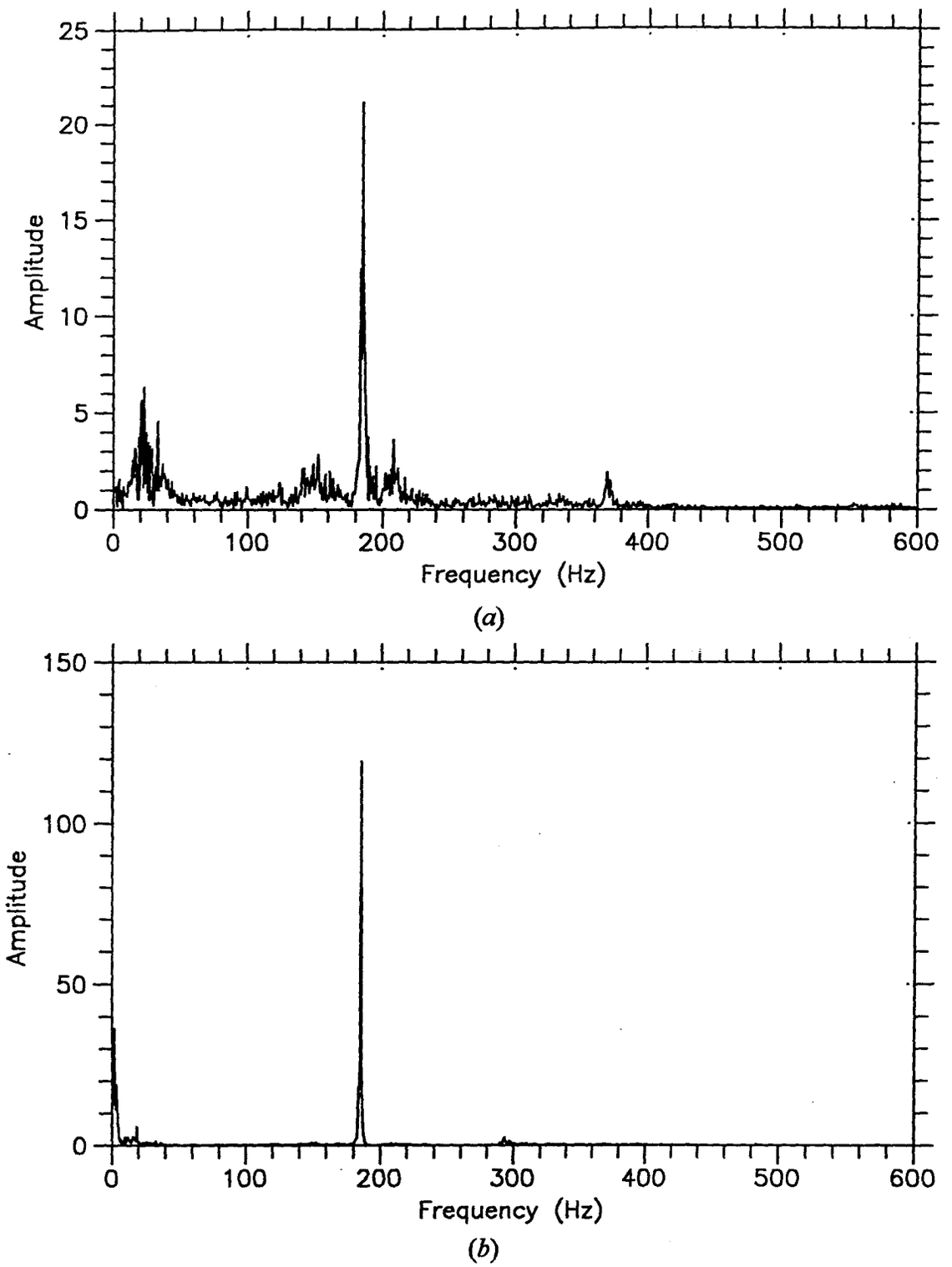

Figure 4.10: Comparison of (*a*) experimental and (*b*) predicted velocity amplitude spectra for chamber with expansion ratio of 4.0.

(*a*) 39 degrees

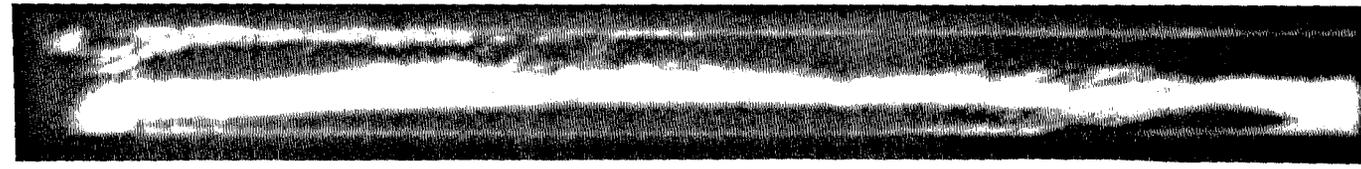

(*b*) 52 degrees

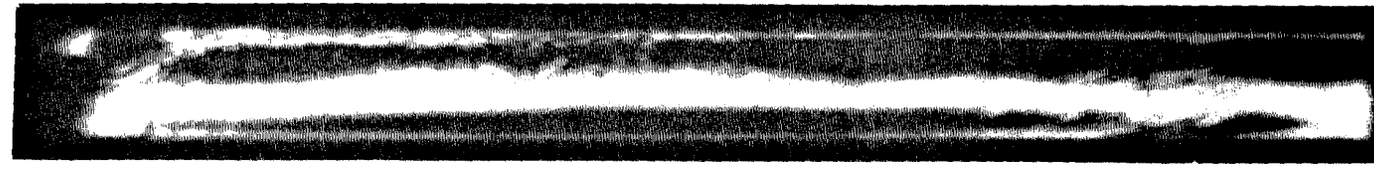

(*c*) 65 degrees

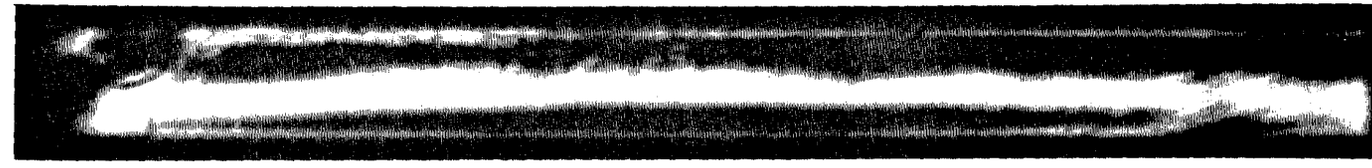

(*d*) 78 degrees

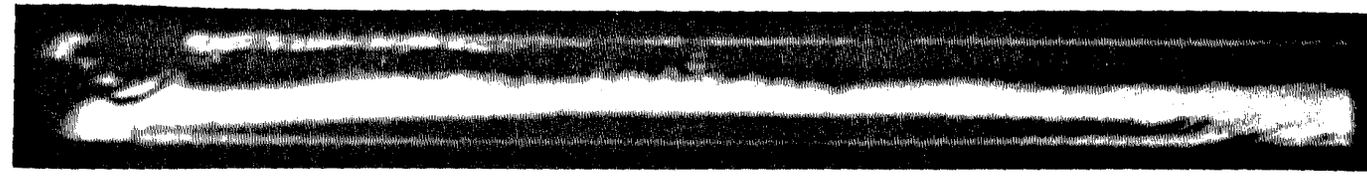

Figure 4.11(*a*) through (*d*): High-speed motion picture shadowgraph sequence for chamber with expansion ratio of 4.0.

(*e*) 91 degrees

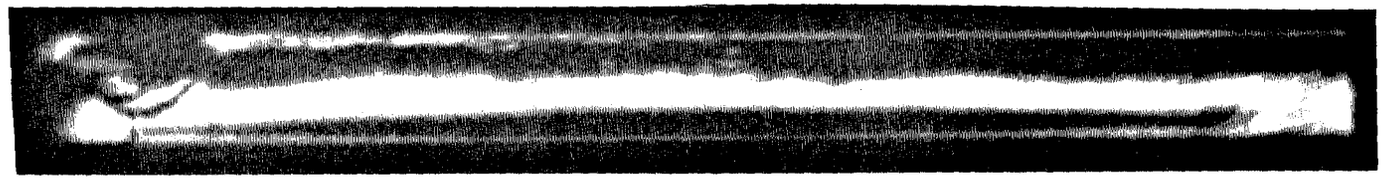

(*f*) 104 degrees

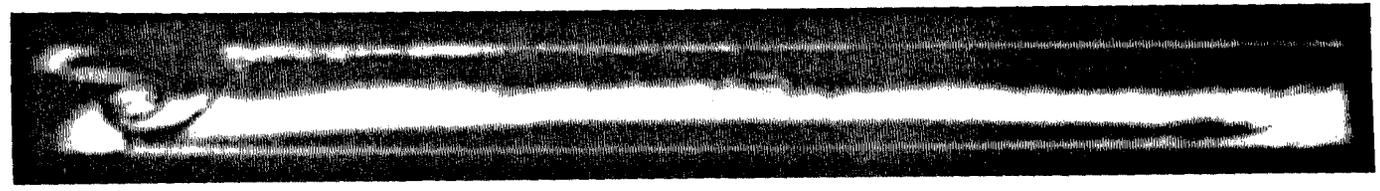

(*g*) 117 degrees

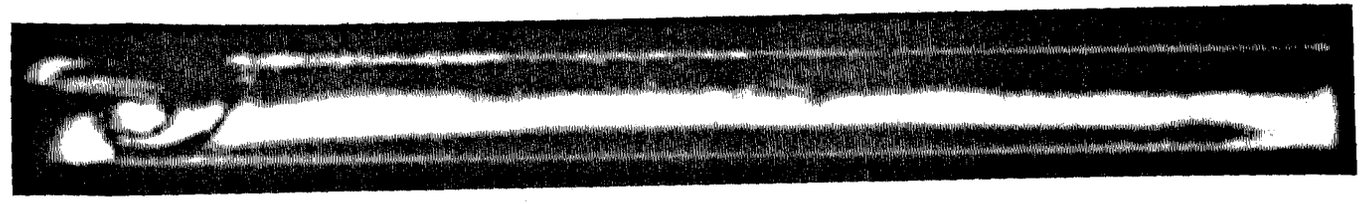

(*h*) 130 degrees

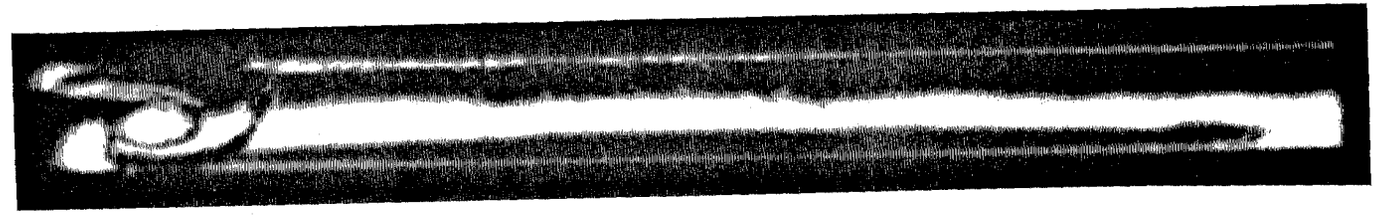

Figure 4.11(*e*) through (*h*): High-speed motion picture shadowgraph sequence for chamber with expansion ratio of 4.0.

(*i*) 143 degrees

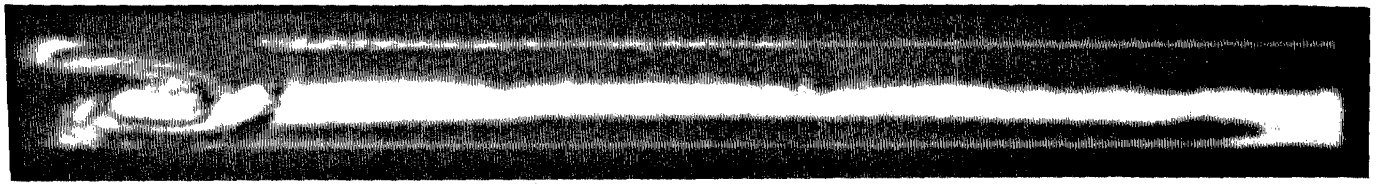

(*j*) 156 degrees

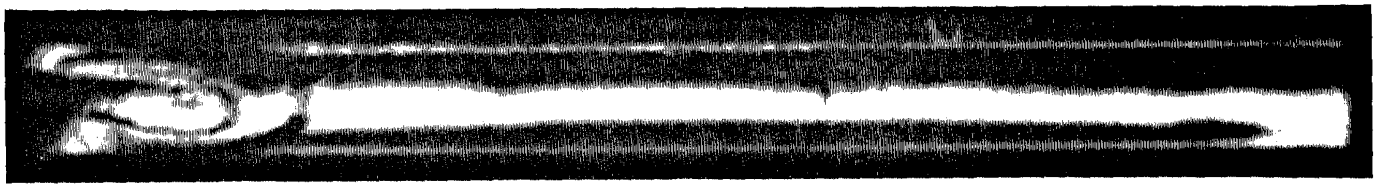

(*k*) 169 degrees

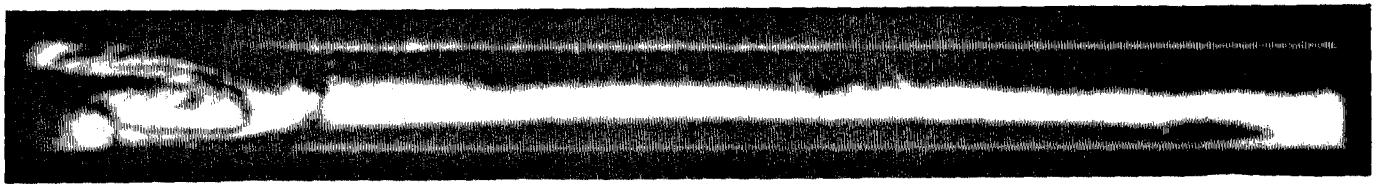

(*l*) 182 degrees

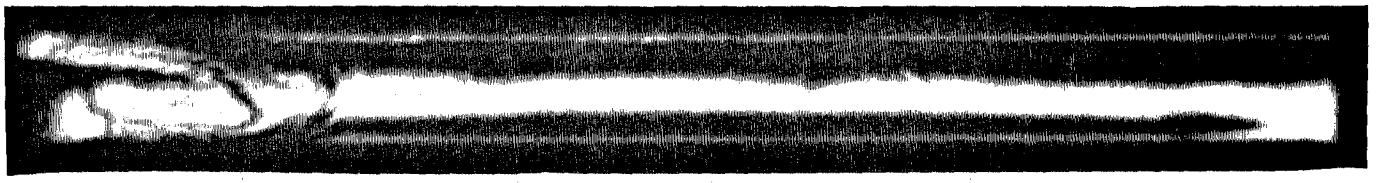

Figure 4.11(*i*) through (*l*): High-speed motion picture shadowgraph sequence for chamber with expansion ratio of 4.0.

(*m*) 195 degrees

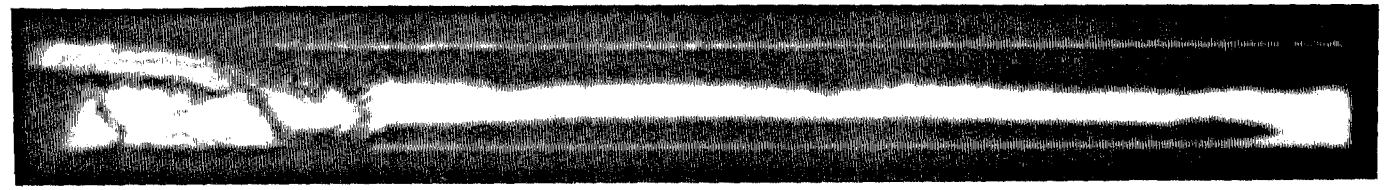

(*n*) 208 degrees

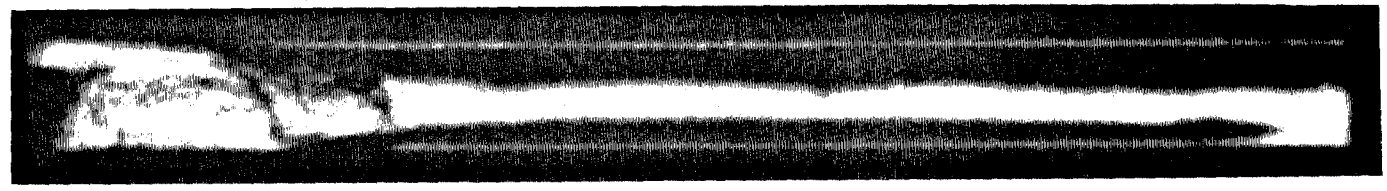

(*o*) 221 degrees

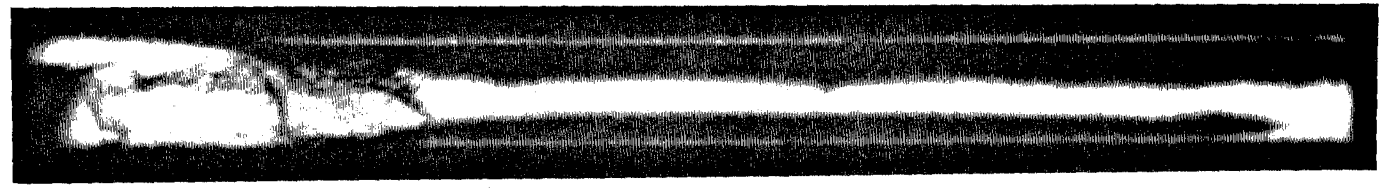

(*p*) 234 degrees

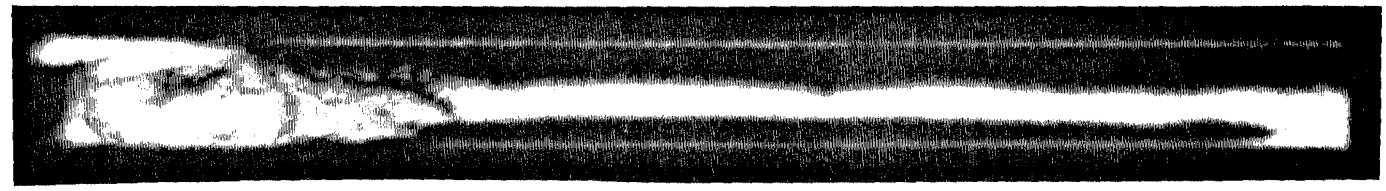

Figure 4.11(*m*) through (*p*): High-speed motion picture shadowgraph sequence for chamber with expansion ratio of 4.0.

(*q*) 247 degrees

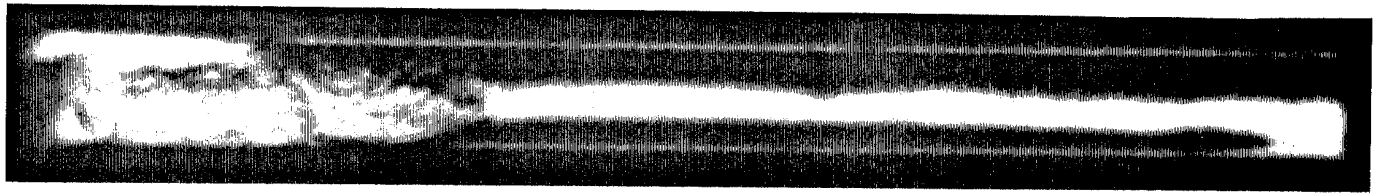

(*r*) 260 degrees

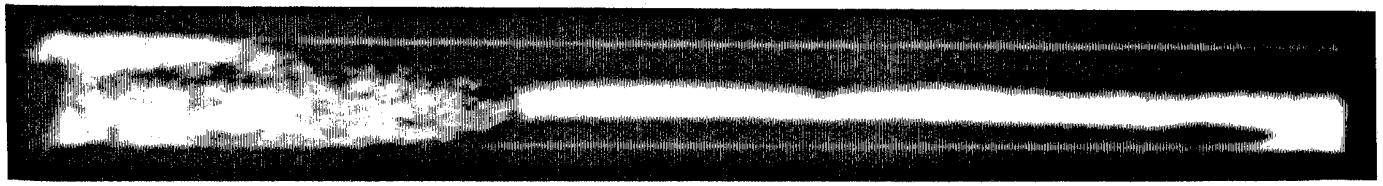

(*s*) 273 degrees

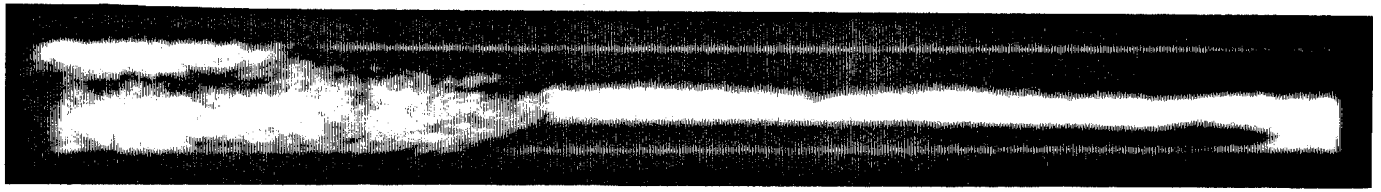

(*t*) 286 degrees

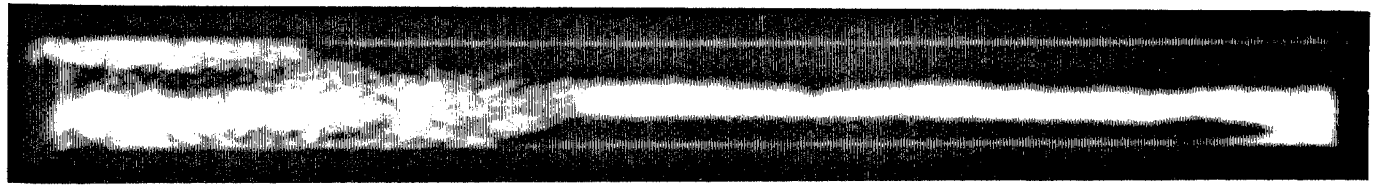

Figure 4.11(*q*) through (*t*): High-speed motion picture shadowgraph sequence for chamber with expansion ratio of 4.0.

(*u*) 299 degrees

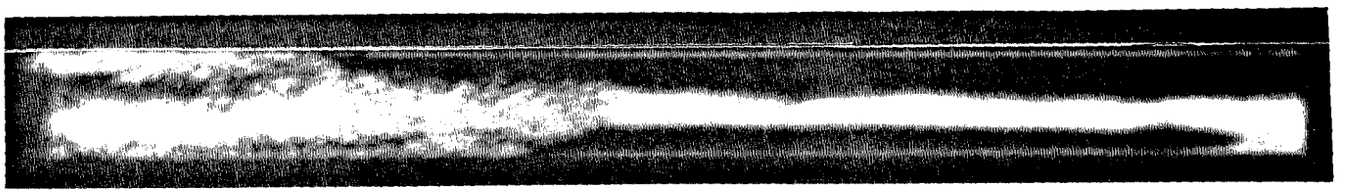

(*v*) 312 degrees

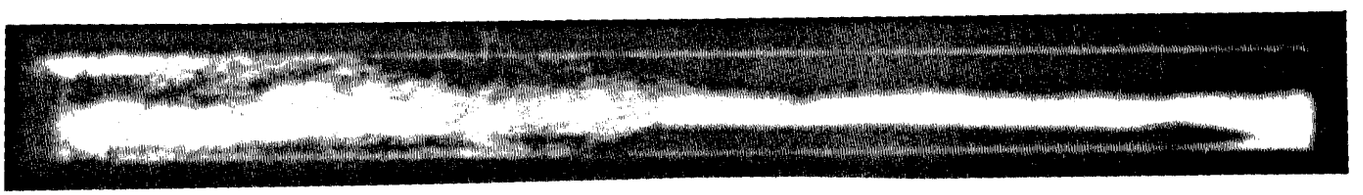

(*w*) 325 degrees

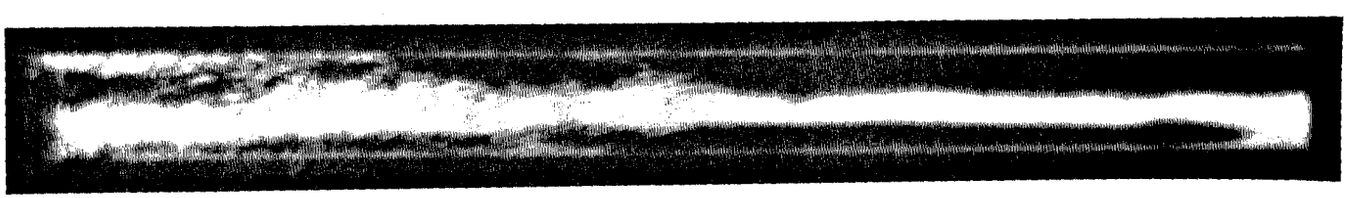

(*x*) 338 degrees

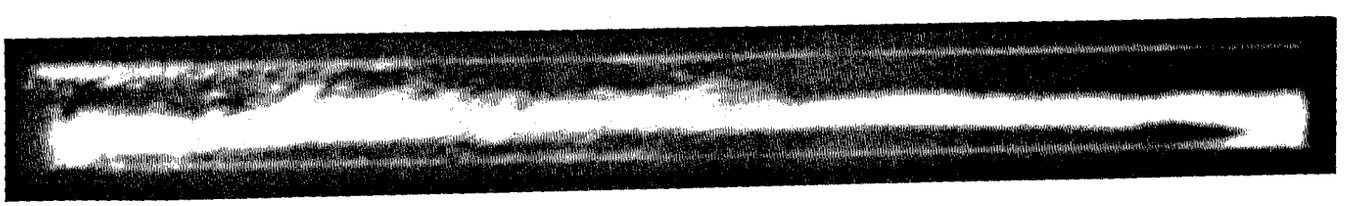

Figure 4.11(*u*) through (*x*): High-speed motion picture shadowgraph sequence for chamber with expansion ratio of 4.0.

(*a*) -48 degrees

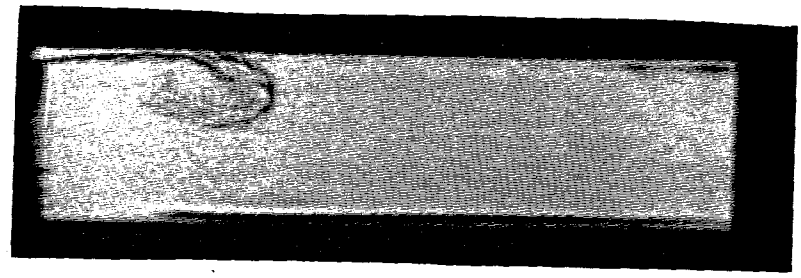

(*b*) -32 degrees

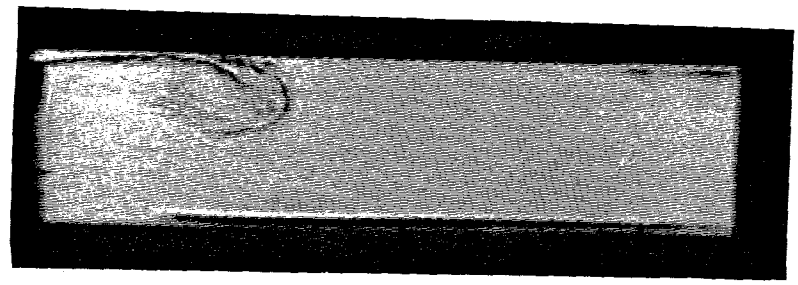

(*c*) -16 degrees

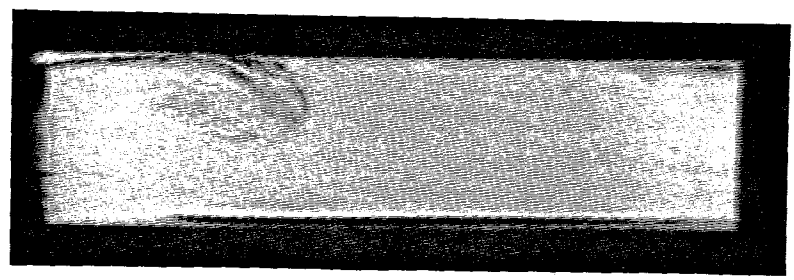

(*d*) 0 degrees

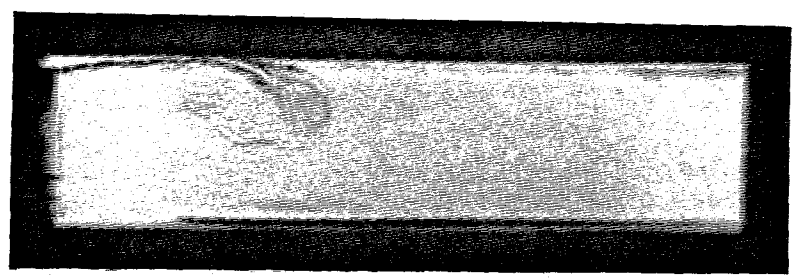

(*e*) 16 degrees

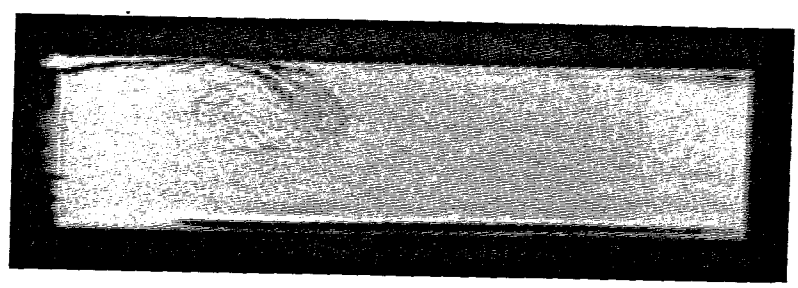

Figure 4.12(*a*) through (*e*): High-speed motion picture shadowgraph sequence for chamber with expansion ratio of 12.0.

(*f*) 32 degrees

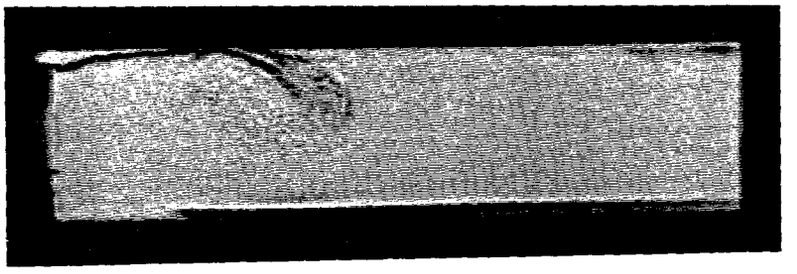

(*g*) 48 degrees

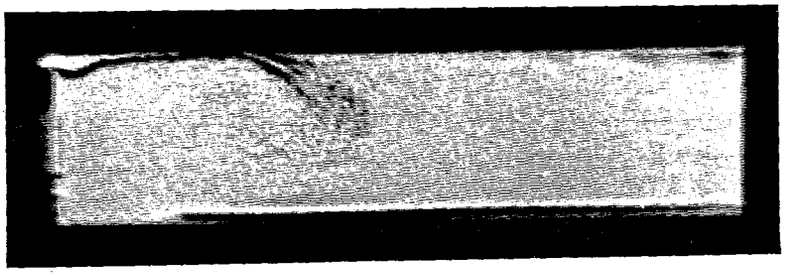

(*h*) 64 degrees

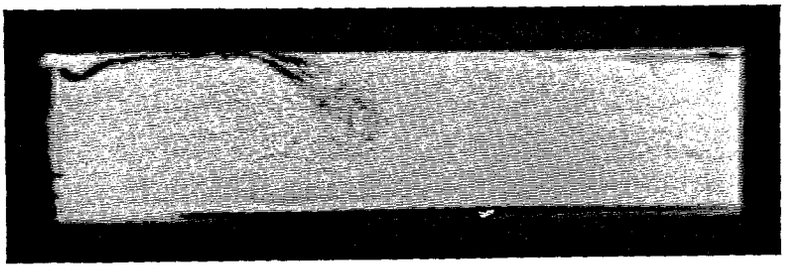

(*i*) 80 degrees

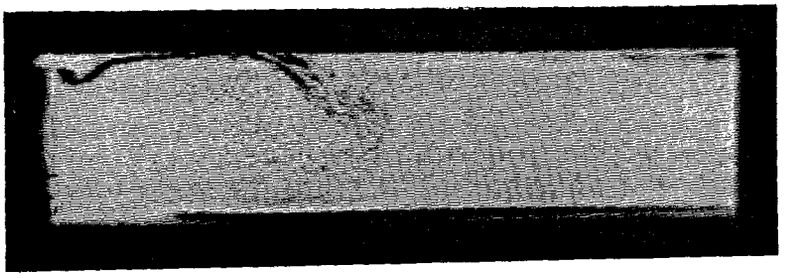

(*j*) 96 degrees

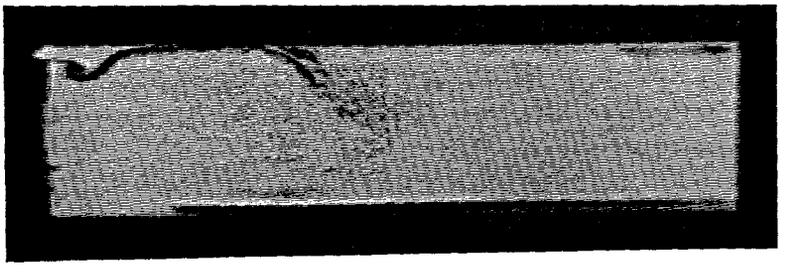

Figure 4.12(*f*) through (*j*): High-speed motion picture shadowgraph sequence for chamber with expansion ratio of 12.0.

(*k*) 112 degrees

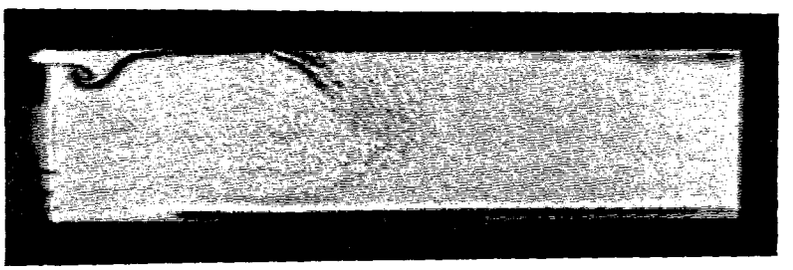

(*l*) 128 degrees

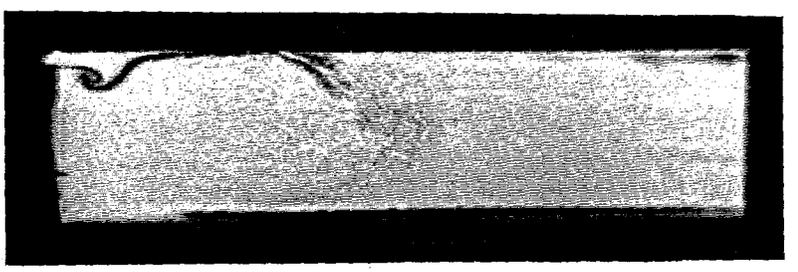

(*m*) 144 degrees

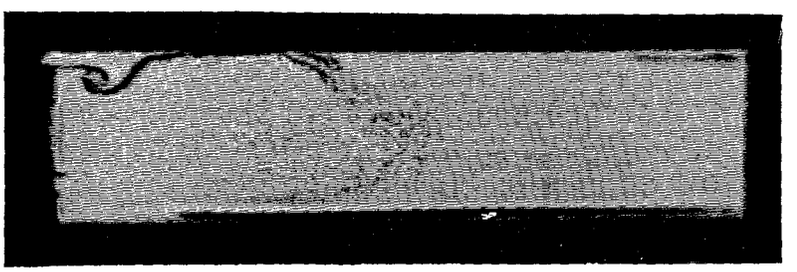

(*n*) 160 degrees

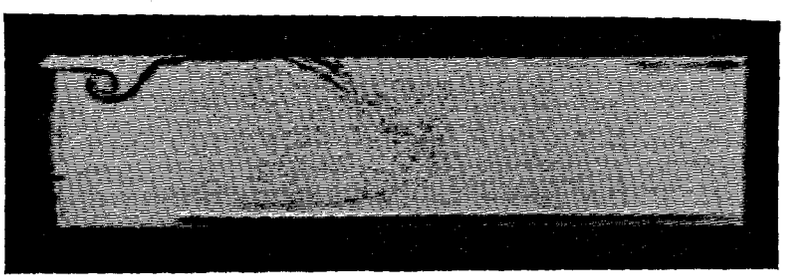

(*o*) 176 degrees

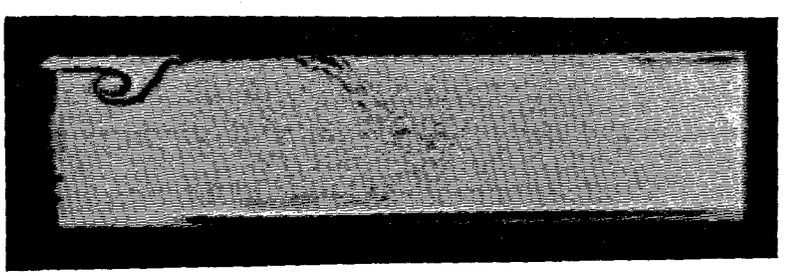

Figure 4.12(*k*) through (*o*): High-speed motion picture shadowgraph sequence for chamber with expansion ratio of 12.0.

(*p*) 192 degrees

(*q*) 208 degrees

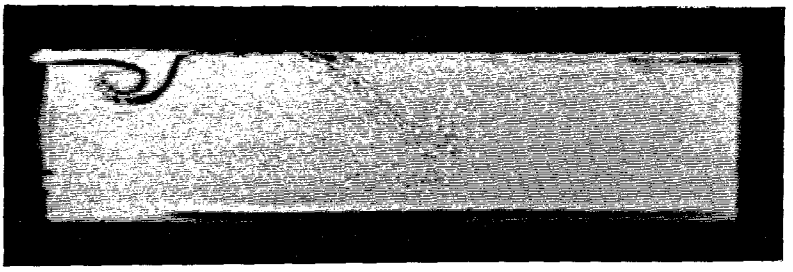

(*r*) 224 degrees

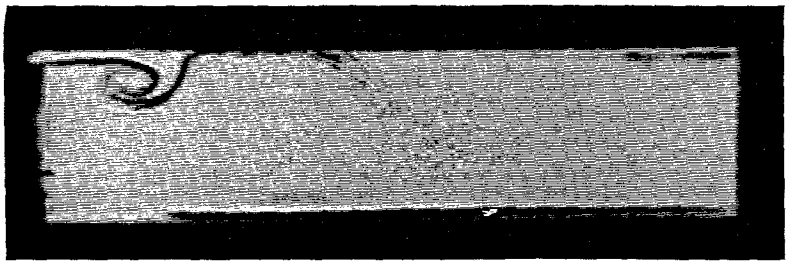

(*s*) 240 degrees

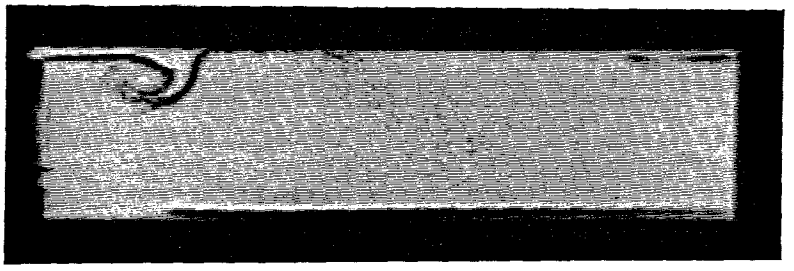

(*t*) 256 degrees

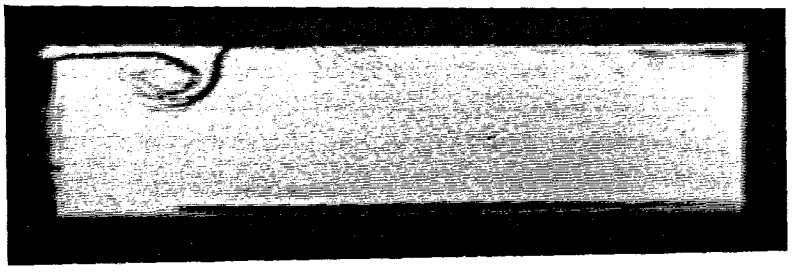

Figure 4.12(*p*) through (*t*): High-speed motion picture shadowgraph sequence for chamber with expansion ratio of 12.0.

(*u*) 272 degrees

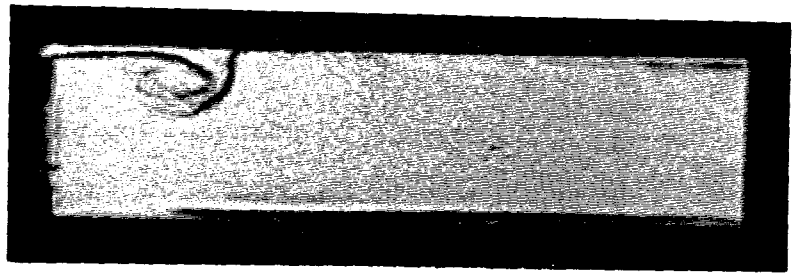

(*v*) 288 degrees

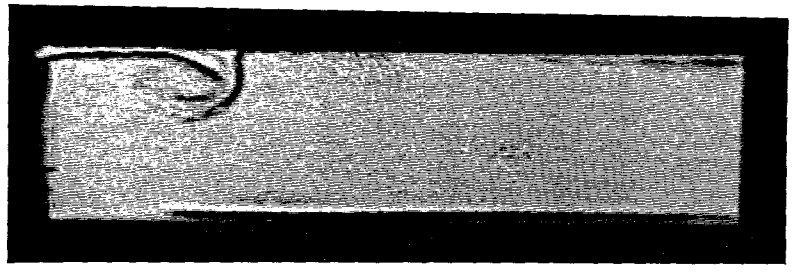

(*w*) 304 degrees

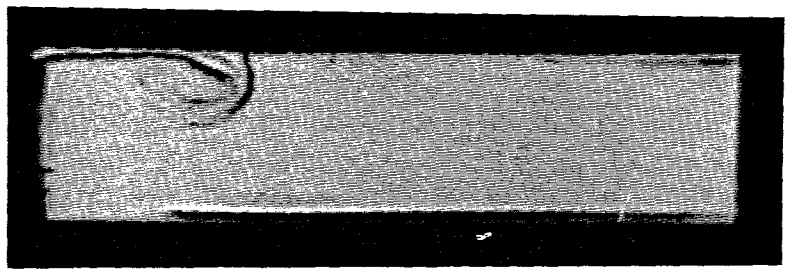

(*x*) 320 degrees

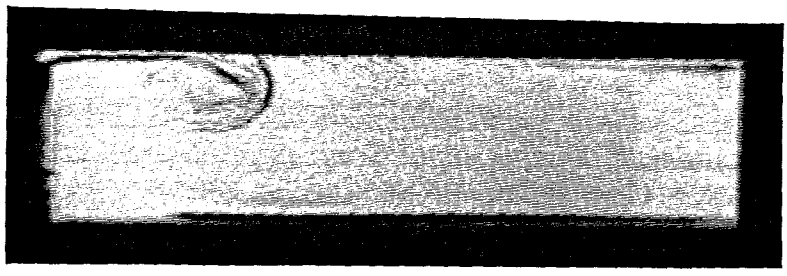

(*y*) 336 degrees

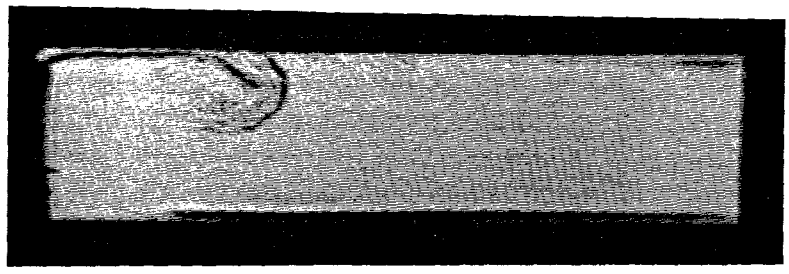

Figure 4.12(*u*) through (*y*): High-speed motion picture shadowgraph sequence for chamber with expansion ratio of 12.0.

(*z*) 352 degrees

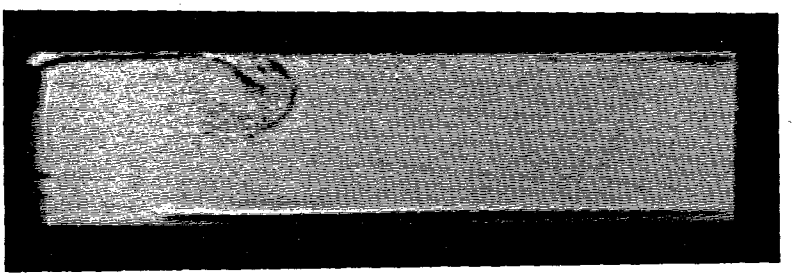

(*aa*) 368 degrees

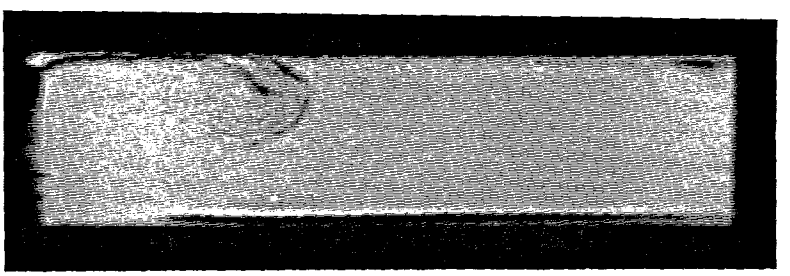

(*bb*) 384 degrees

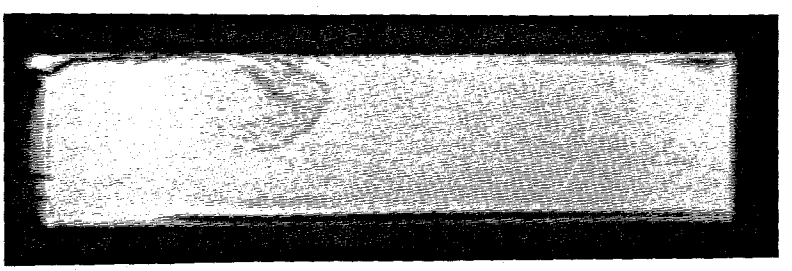

cc) 390 degrees

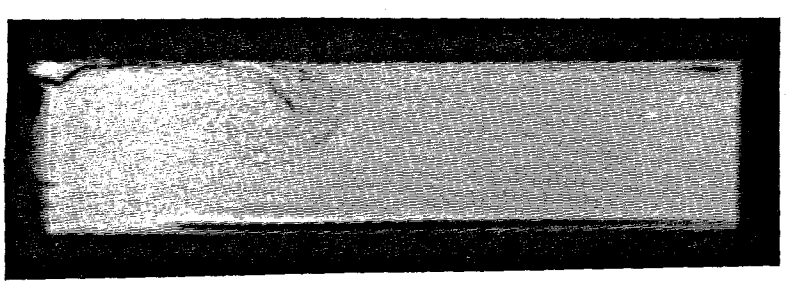

(*dd*) 406 degrees

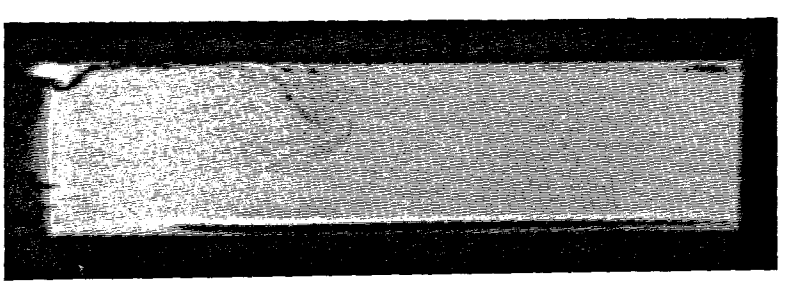

Figure 4.12(*z*) through (*dd*): High-speed motion picture shadowgraph sequence for chamber with expansion ratio of 12.0.

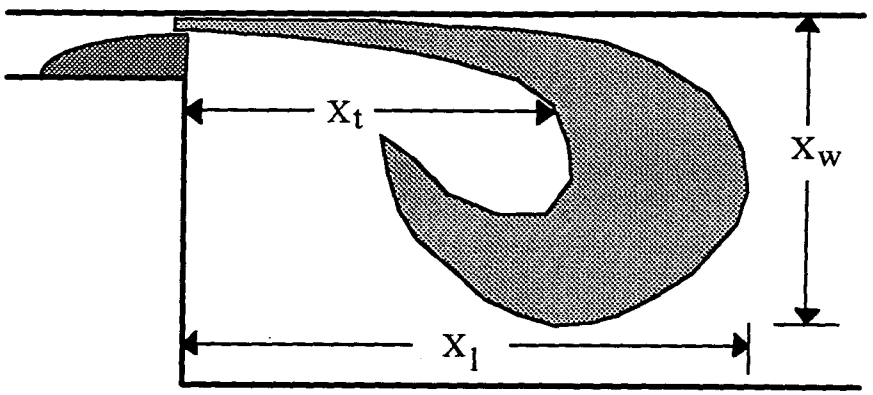

Figure 4.13: Schematic diagram of vortex structure.

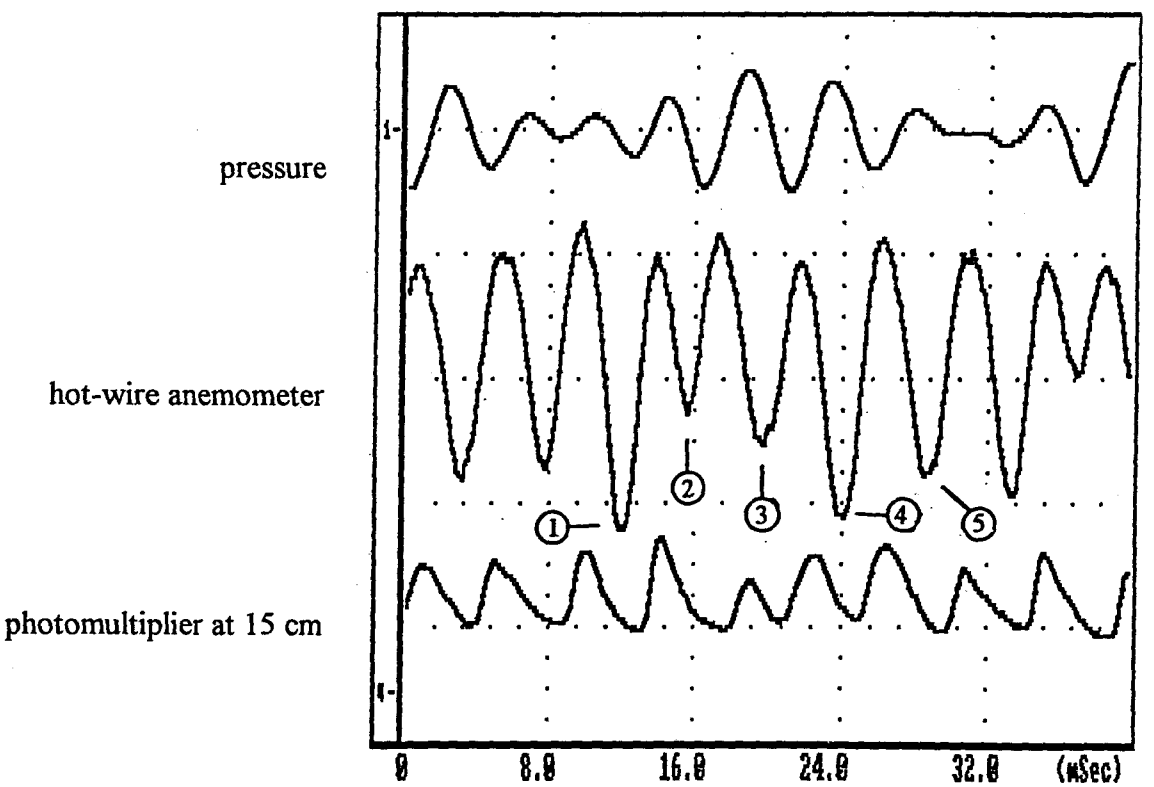

Figure 4.14: Raw data traces of five vortex cycles for chamber with expansion ratio of 12.0.

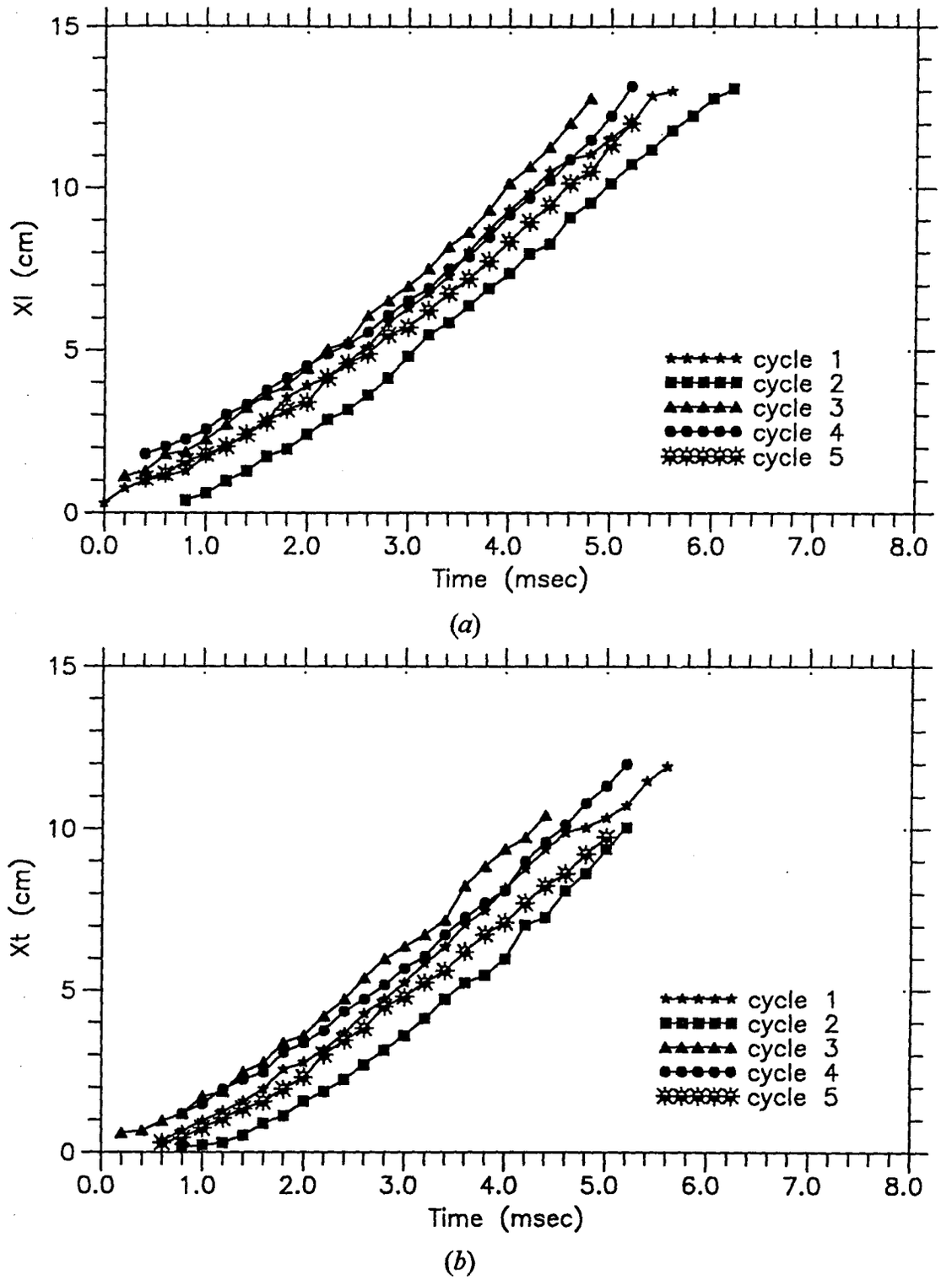

Figure 4.15(*a*) and (*b*): Vortex dimensions (*a*) X_l and (*b*) X_t as functions of time for chamber with expansion ratio of 12.0.

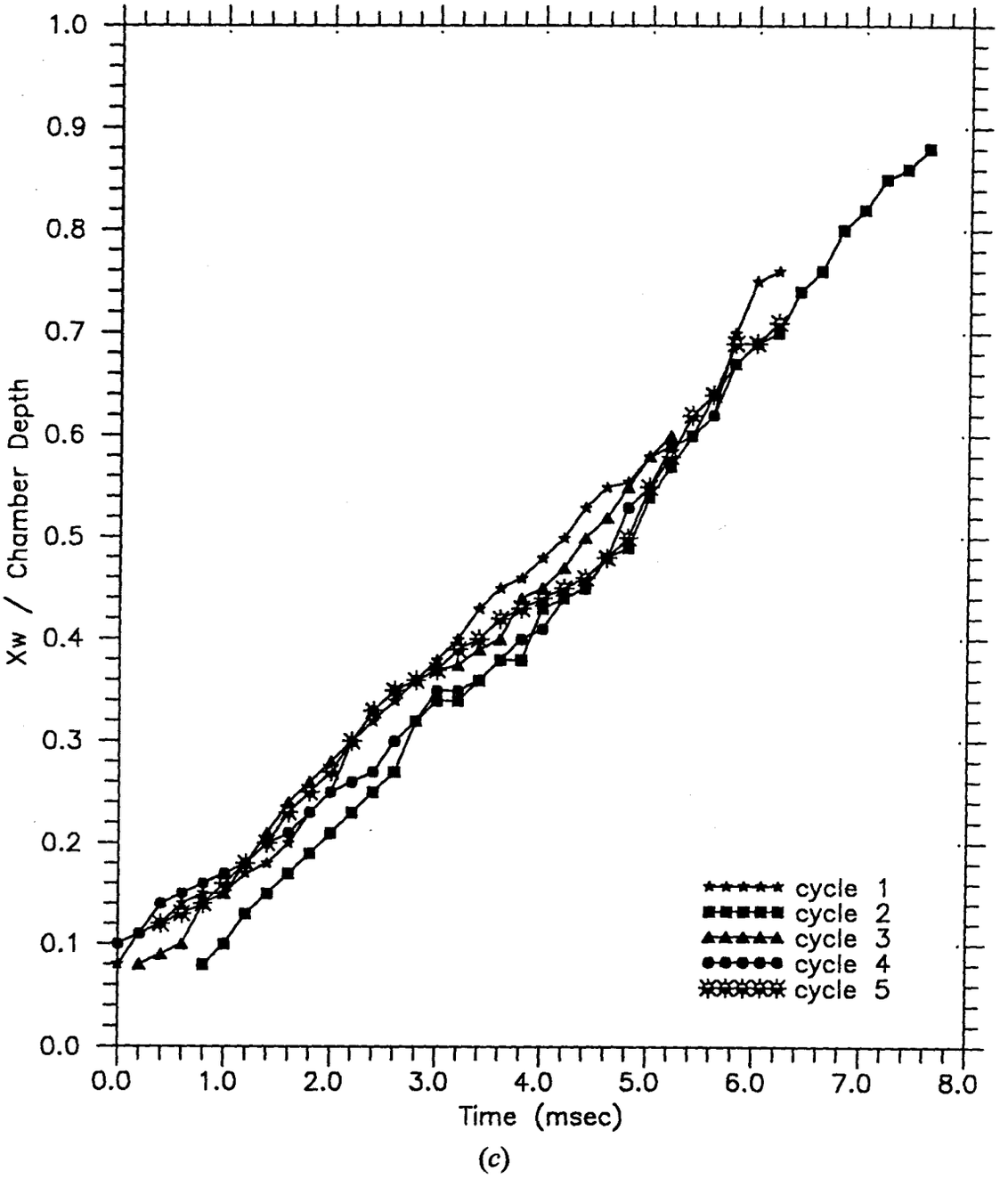

(*c*)

Figure 4.15*c*: Ratio of vortex dimension X_w to chamber depth as a function of time for chamber with expansion ratio of 12.0.

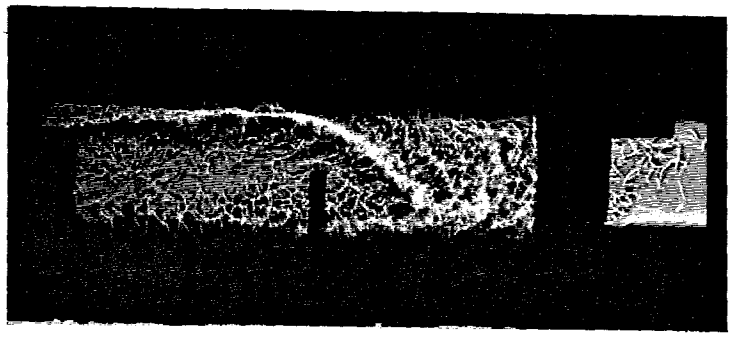

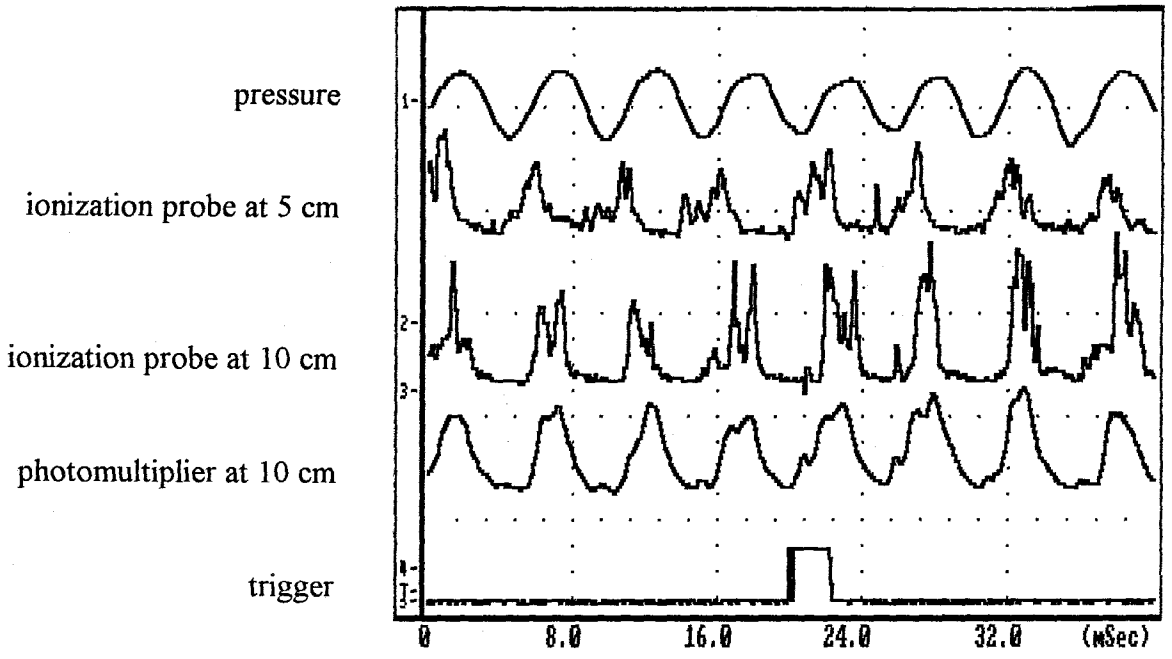

Figure 4.16: Shadowgraph and ionization probe data for chamber with expansion ratio of 4.0.

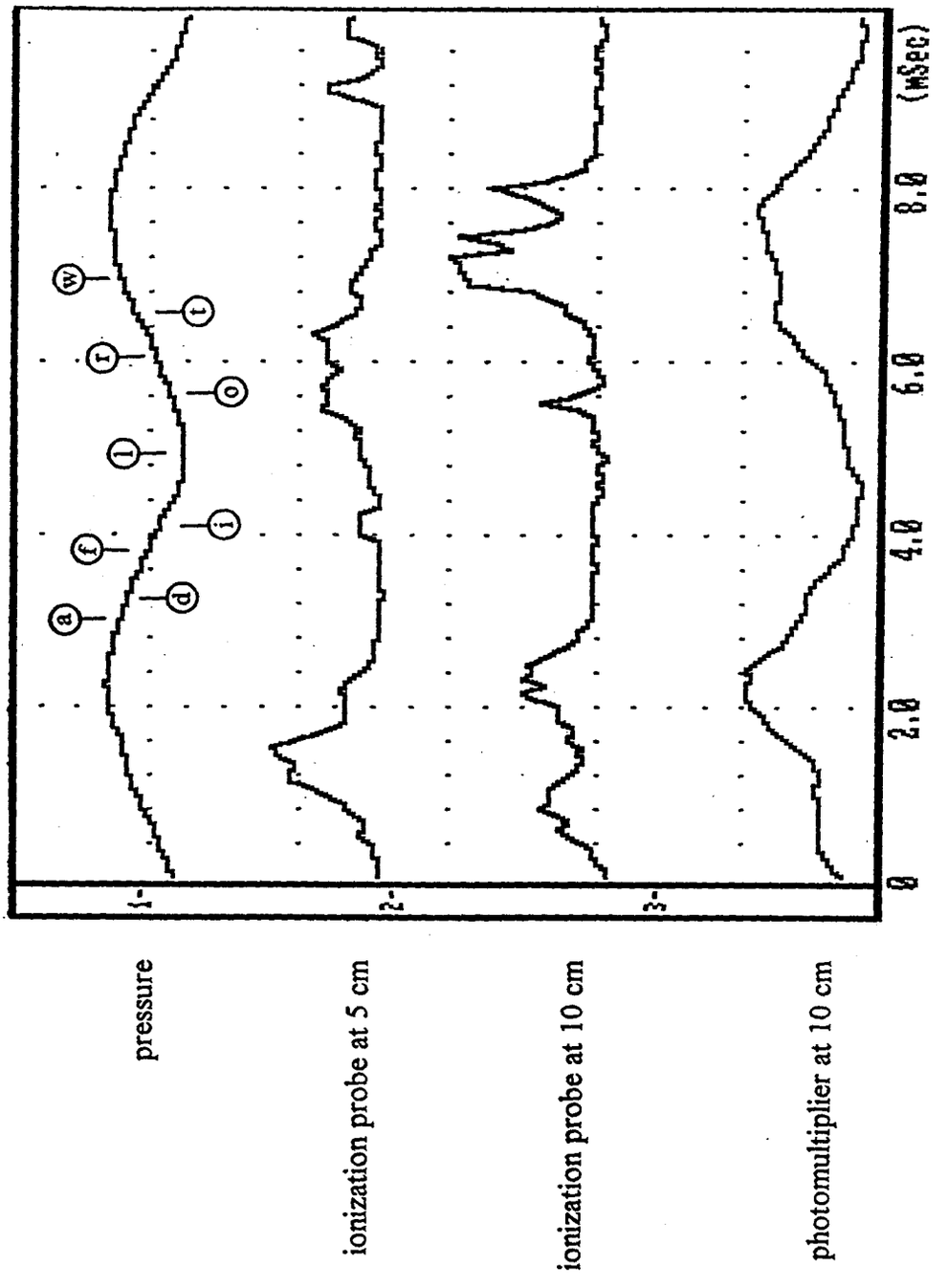

Figure 4.17: Data record containing two ionization probe traces for chamber with expansion ratio of 4.0.

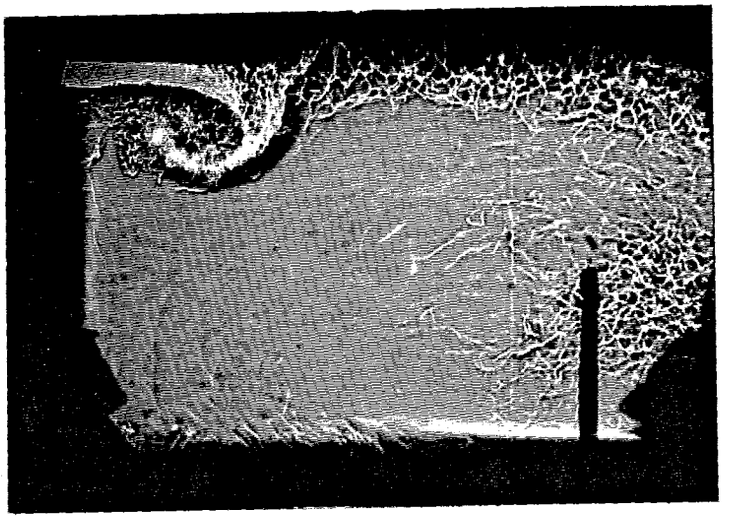

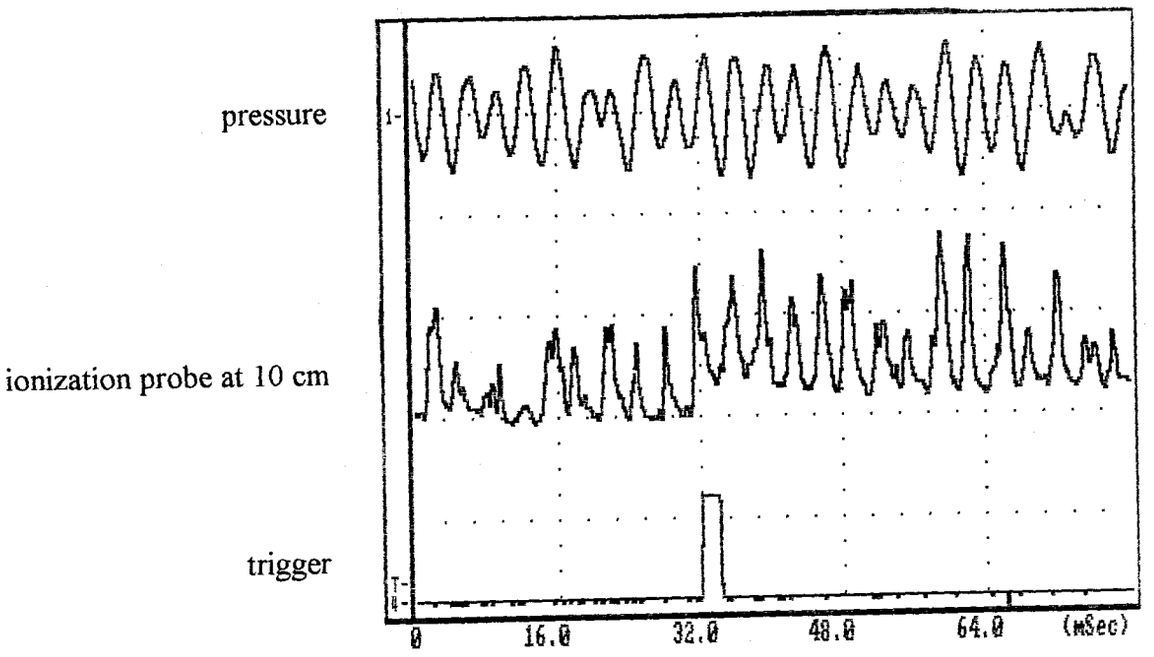

Figure 4.18: Shadowgraph and ionization probe data for chamber with expansion ratio of 12.0.

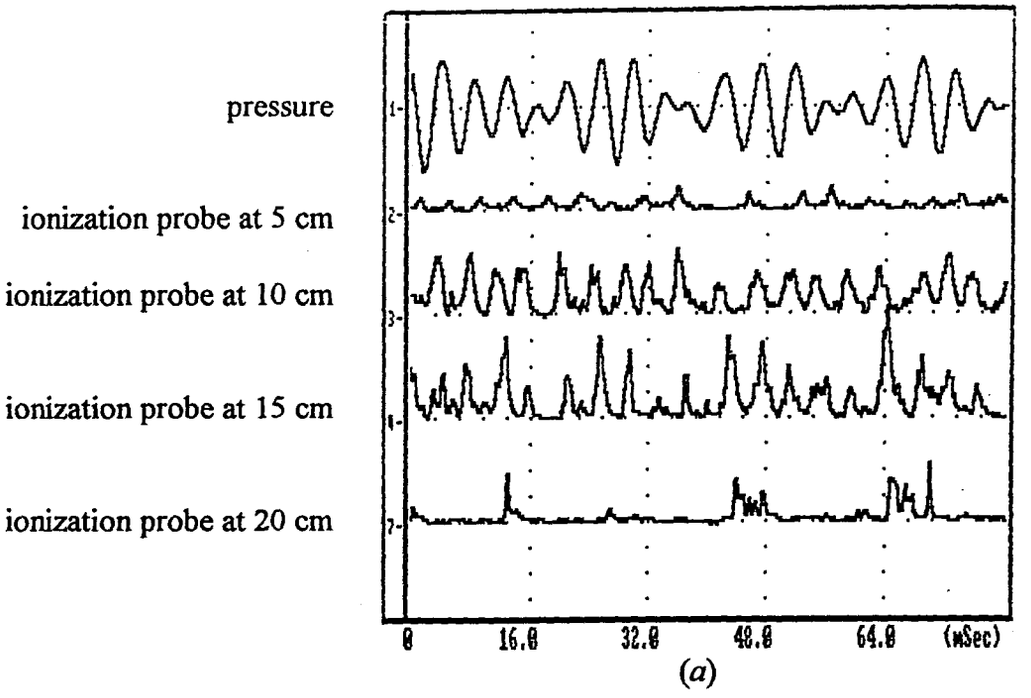

(*a*)

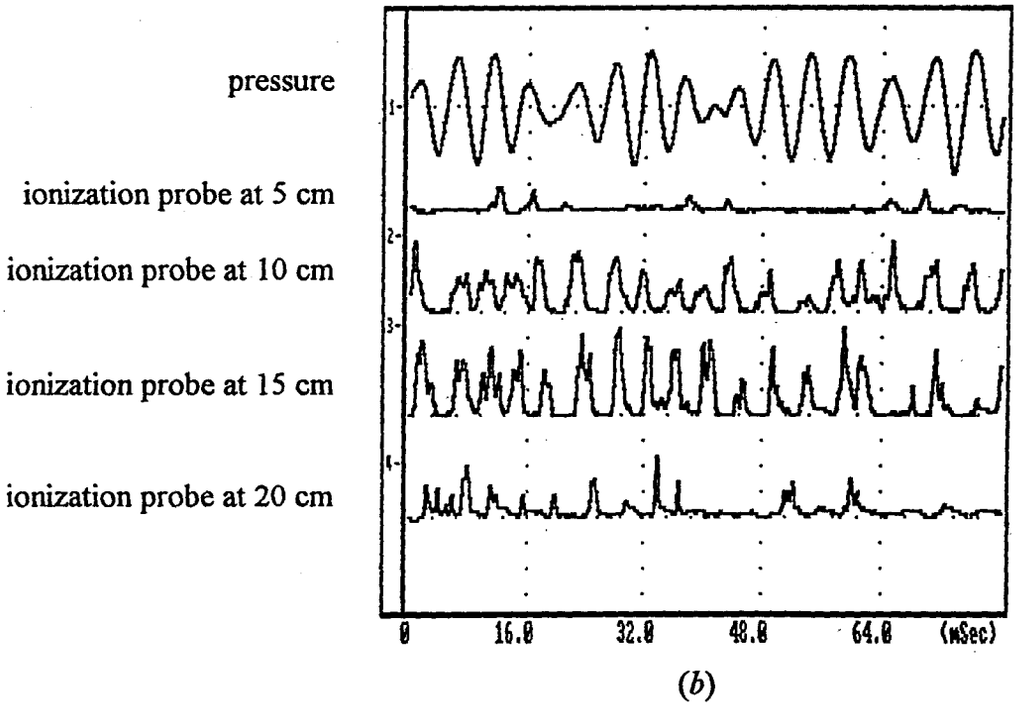

(*b*)

Figure 4.19(*a*) and (*b*): Ionization probe profiles at various axial positions for chamber with expansion ratio of 12.0 at (*a*) 7 cm and (*b*) 5.7 cm above combustor floor.

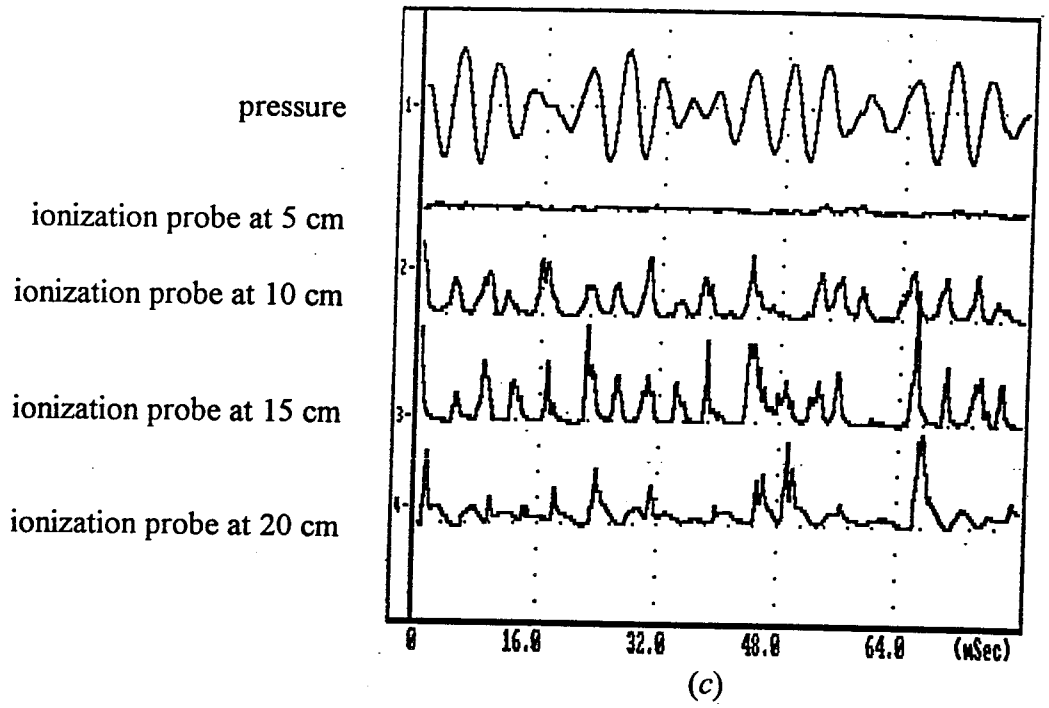

(*c*)

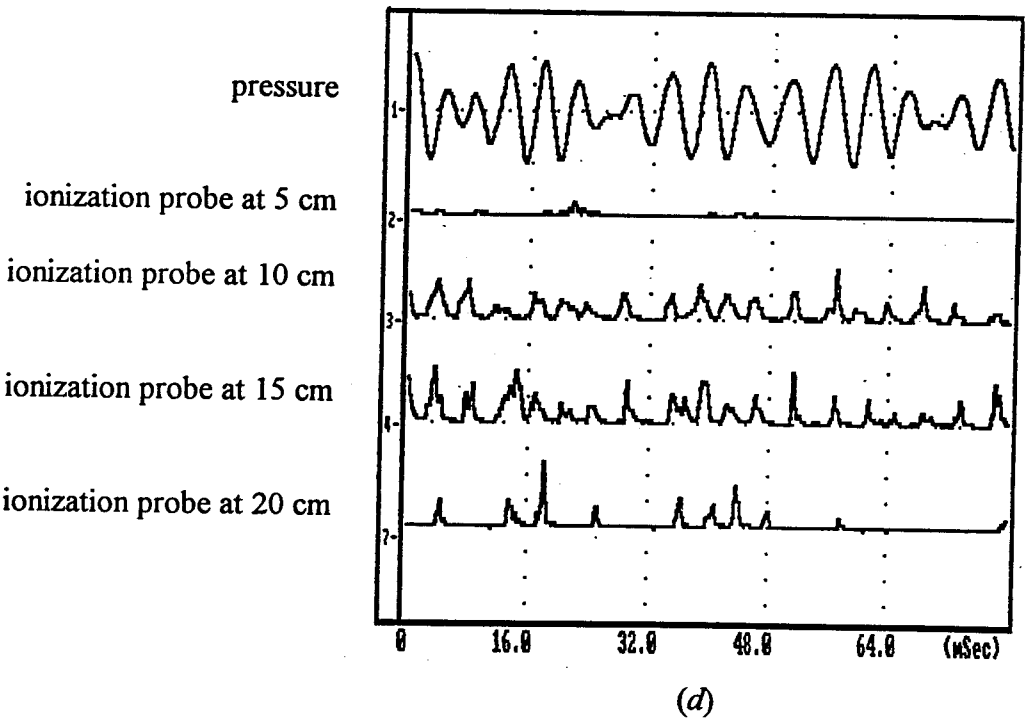

(*d*)

Figure 4.19(*c*) and (*d*): Ionization probe profiles at various axial positions for chamber with expansion ratio of 12.0 at (*c*) 4.4 cm and (*d*) 3.2 cm above combustor floor.

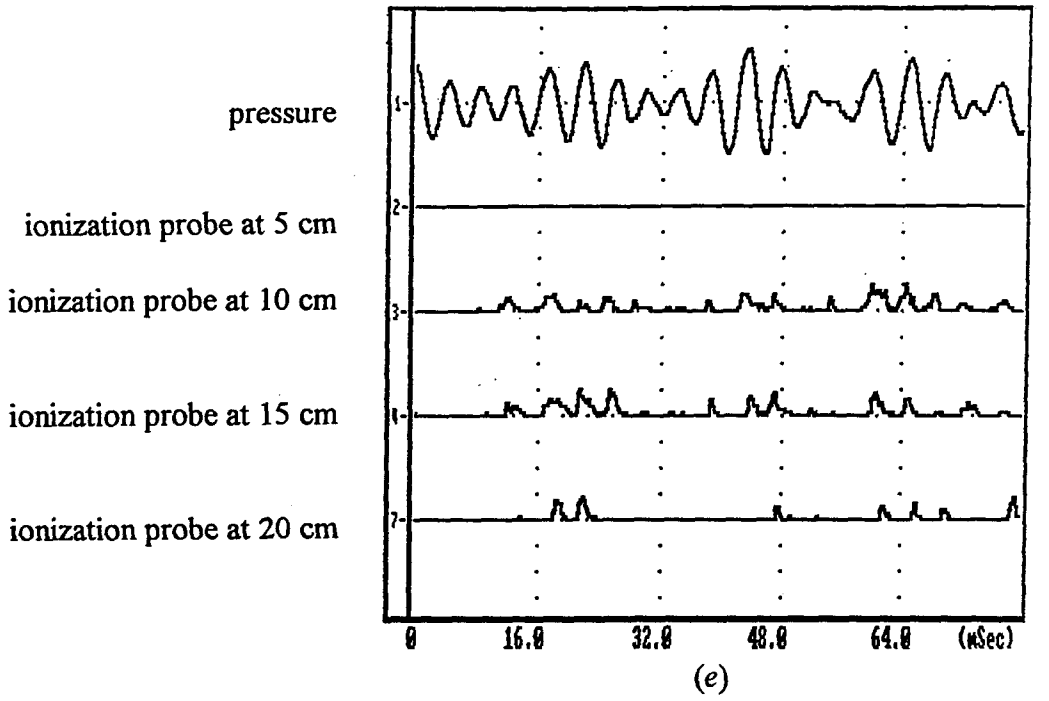

(*e*)

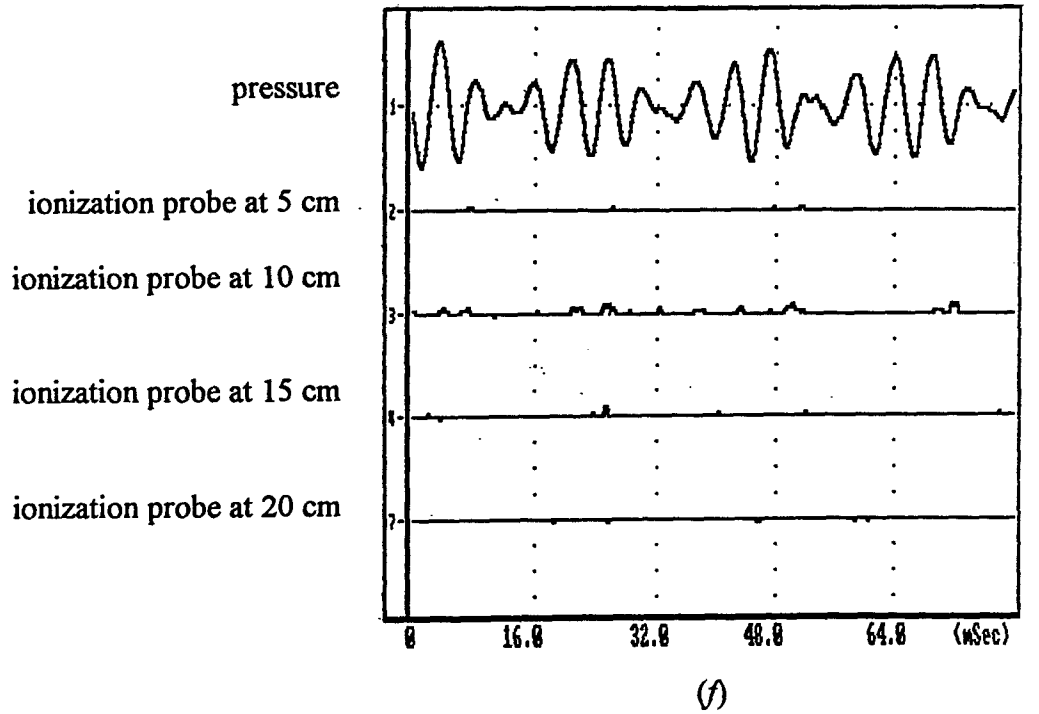

(*f*)

Figure 4.19(*e*) and (*f*): Ionization probe profiles at various axial positions for chamber with expansion ratio of 12.0 at (*e*) 1.9 cm and (*f*) 0.6 cm above combustor floor.

(*a*)

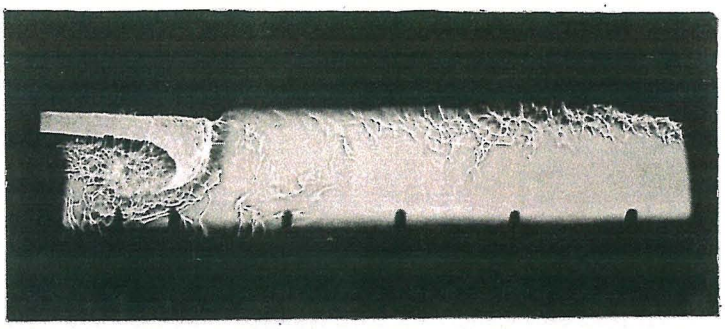

(*b*)

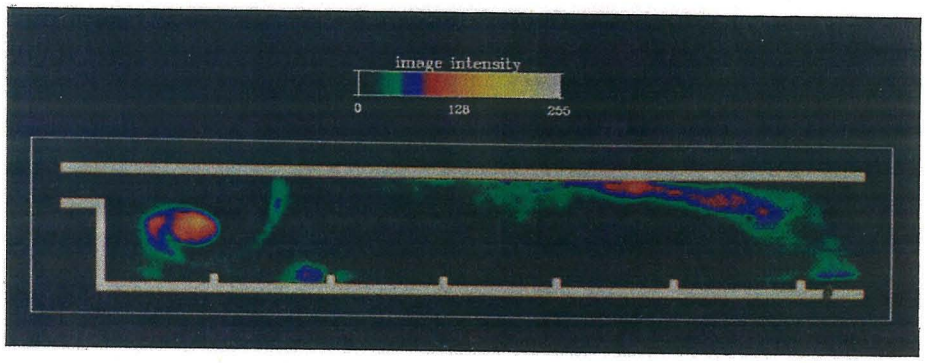

Figure 4.20: Simultaneous (*a*) shadowgraph and (*b*) chemiluminescence images at 81 degrees in pressure cycle for chamber with expansion ratio of 4.0.

(*a*)

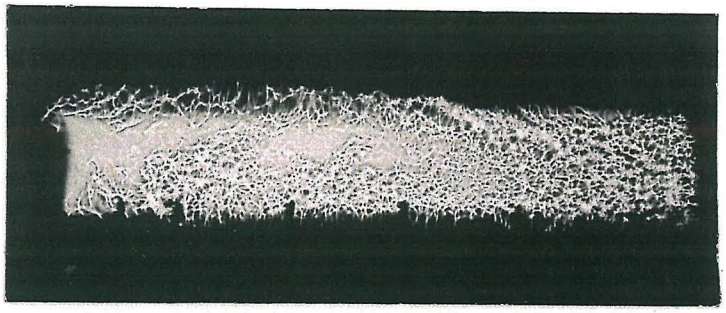

(*b*)

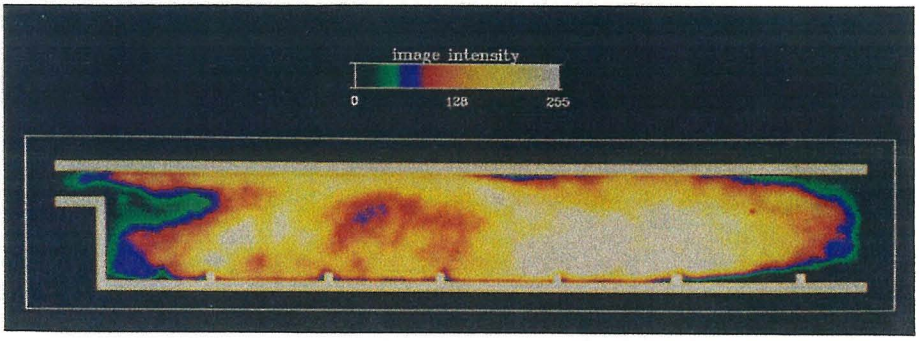

Figure 4.21: Simultaneous (*a*) shadowgraph and (*b*) chemiluminescence images at 142 degrees in pressure cycle for chamber with expansion ratio of 4.0.

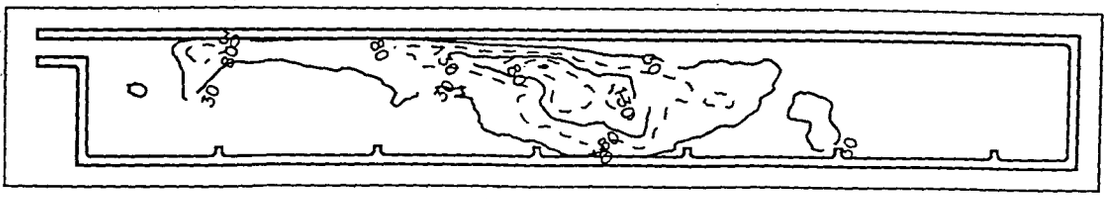

(*a*) 11 degrees

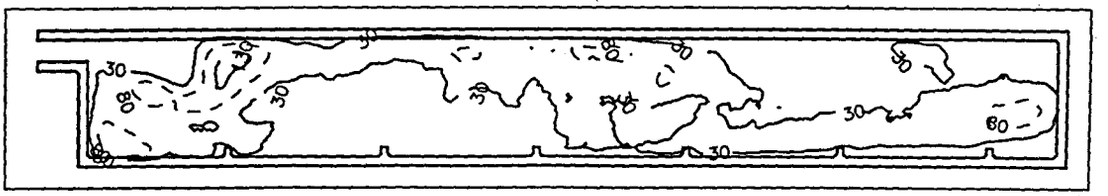

(*b*) 26 degrees

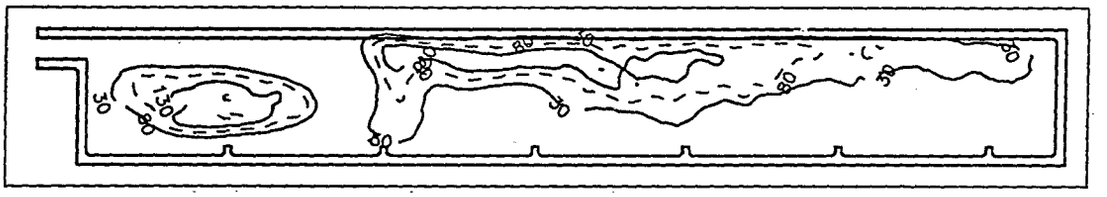

(*c*) 209 degrees

(*d*) 349 degrees

Figure 4.22(*a*) through (*d*): Contour plots of chemiluminescence images for chamber with expansion ratio of 4.0 at various phases in cycle.

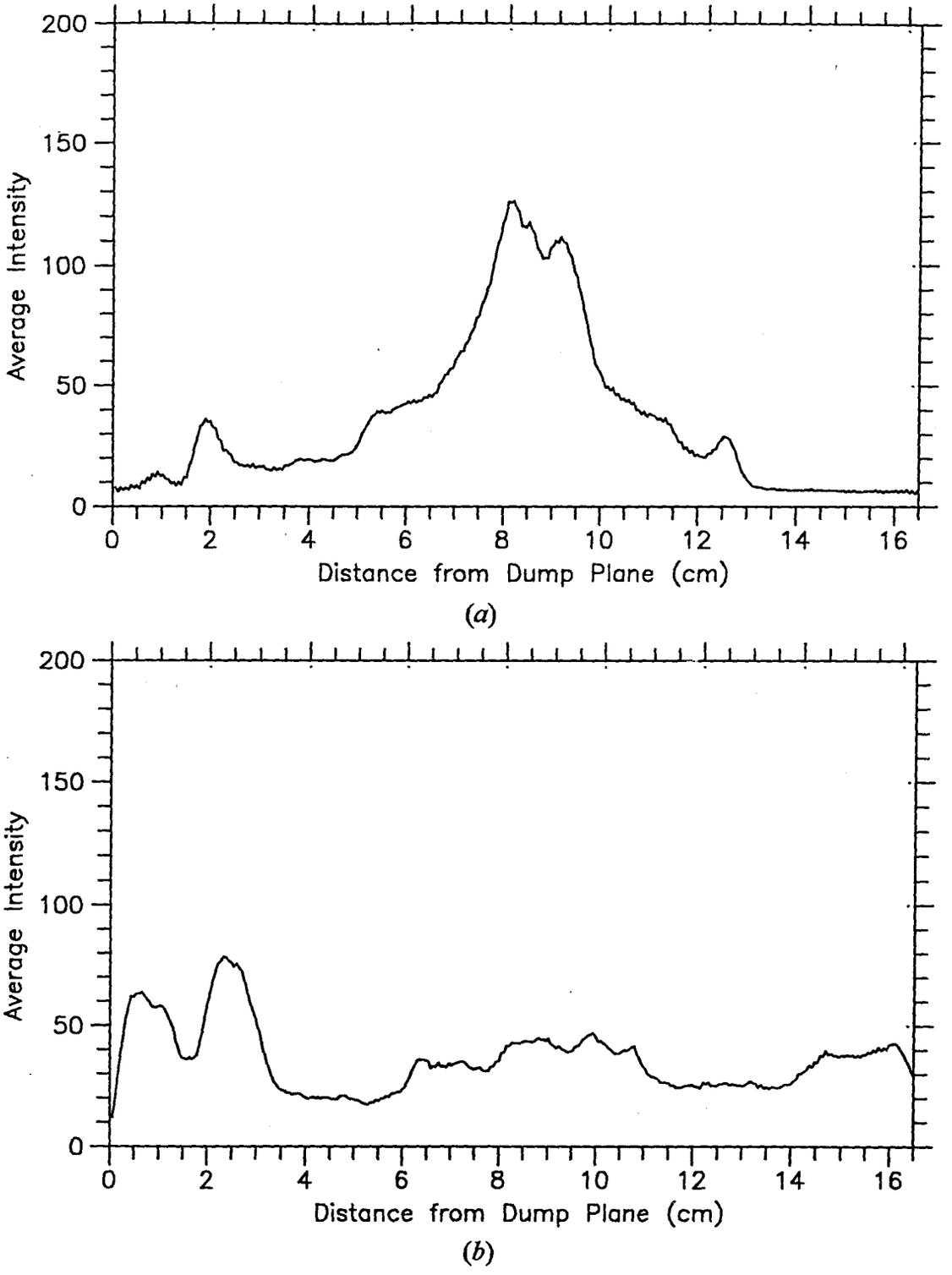

Figure 4.23: Average light intensity as a function of axial position for chamber with expansion ratio of 4.0 at (*a*) 11 degrees and (*b*) 26 degrees in cycle.

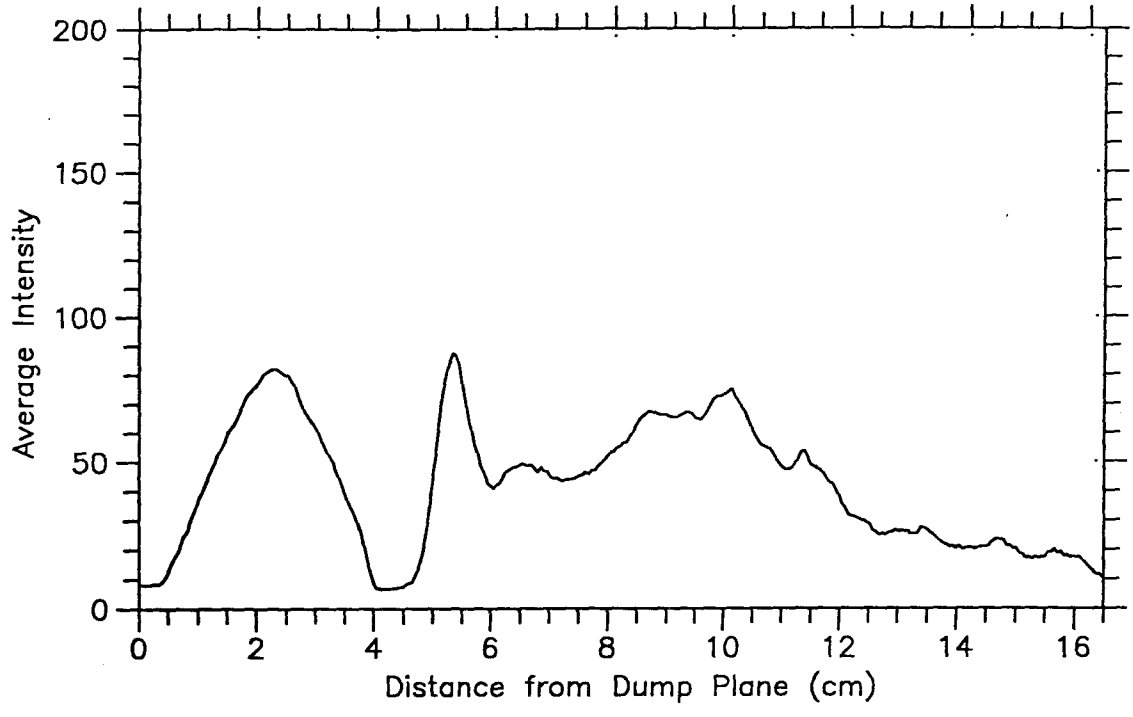

(*c*)

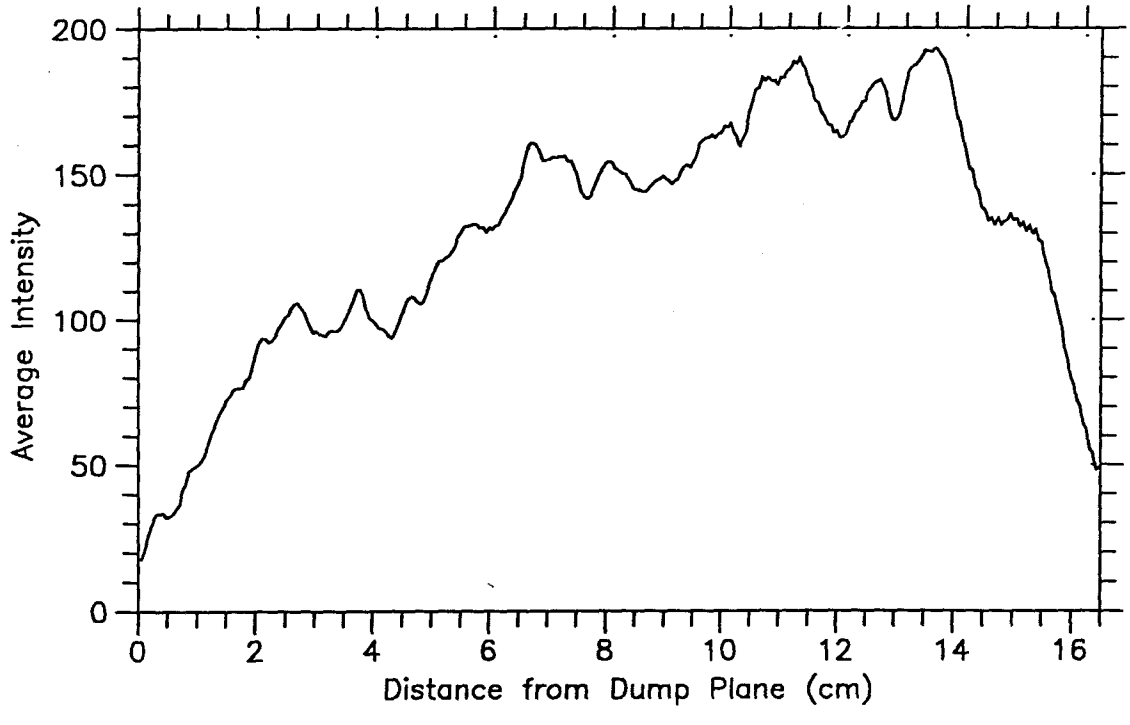

(*d*)

Figure 4.23: Average light intensity as a function of axial position for chamber with expansion ratio of 4.0 at (*c*) 209 degrees and (*d*) 349 degrees in cycle.

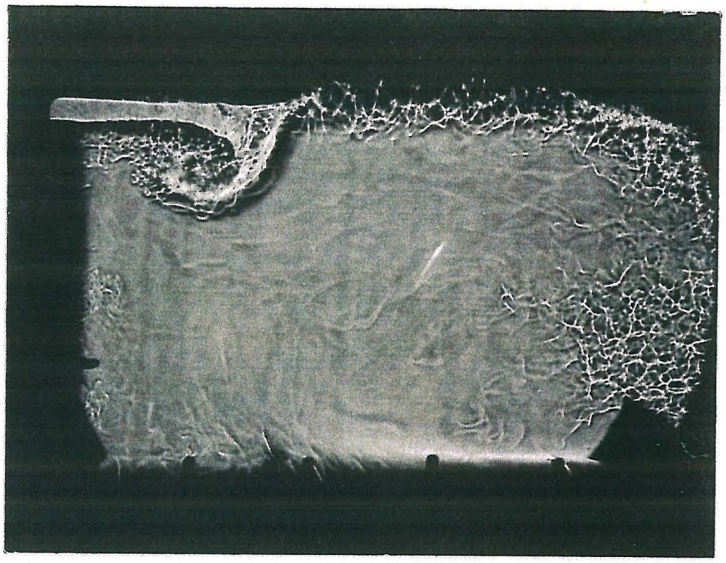

(*a*)

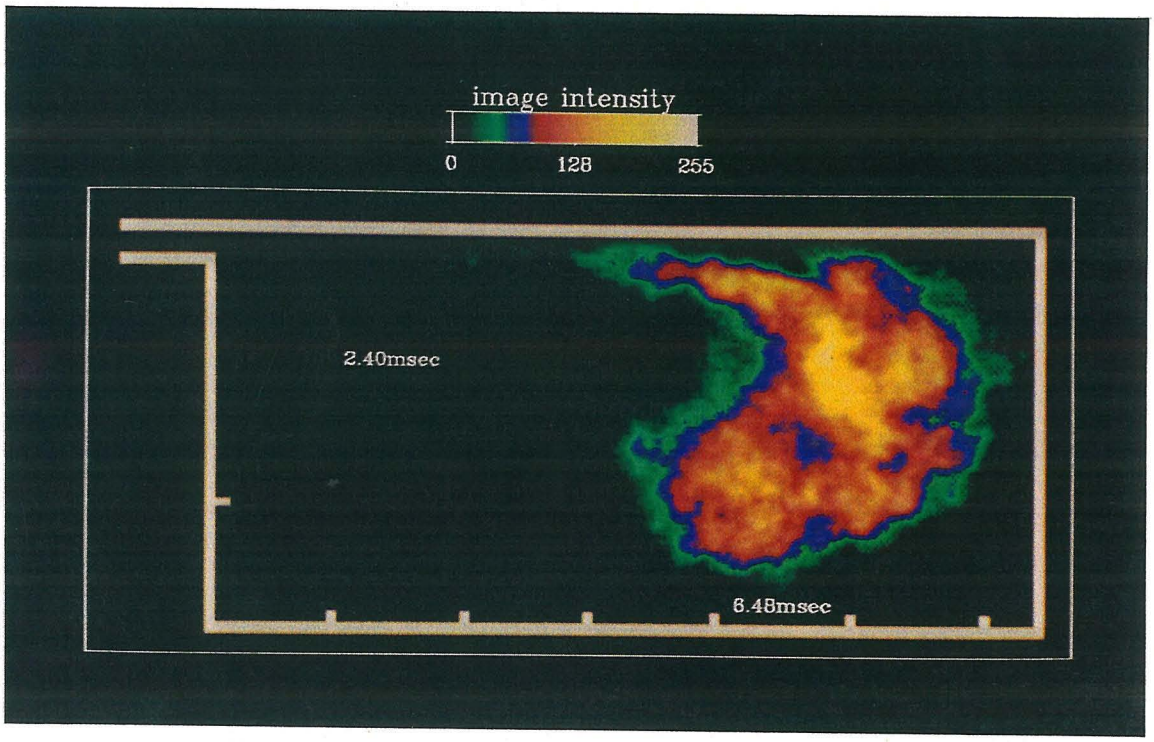

(*b*)

Figure 4.24: Simultaneous (*a*) shadowgraph and (*b*) chemiluminescence images at 203 degrees in pressure cycle for chamber with expansion ratio of 12.0.

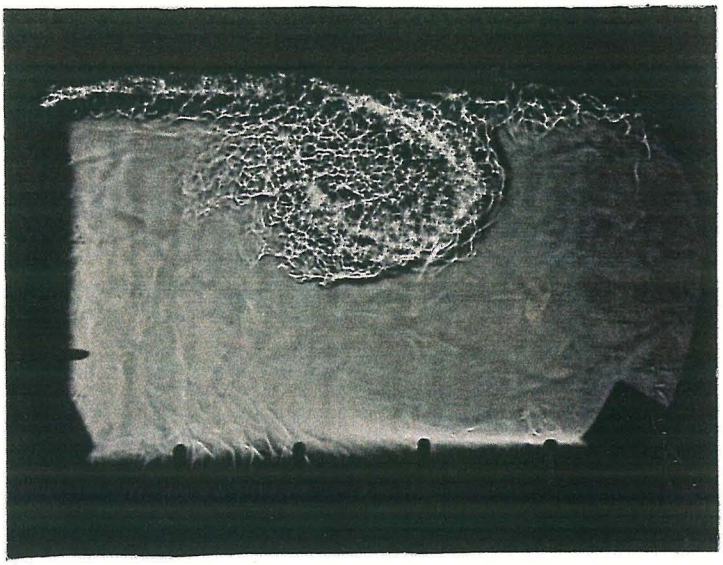

(*a*)

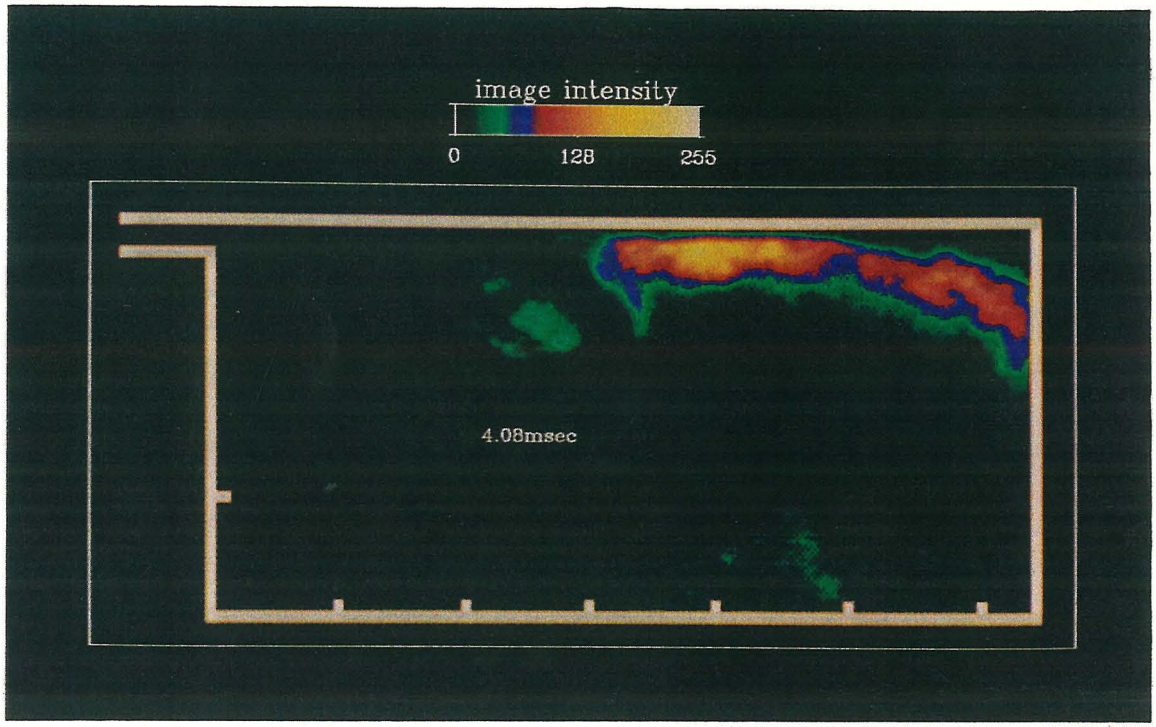

(*b*)

Figure 4.25: Simultaneous (*a*) shadowgraph and (*b*) chemiluminescence images at 345 degrees in pressure cycle for chamber with expansion ratio of 12.0.

(*a*) 129 degrees

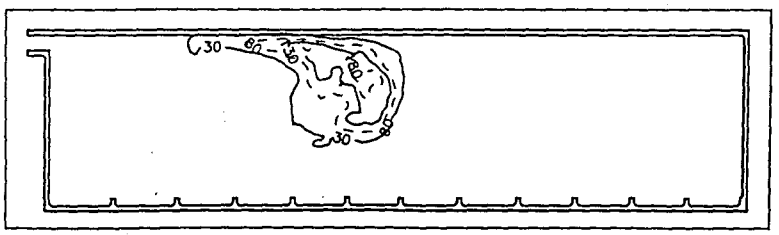

(*b*) 169 degrees

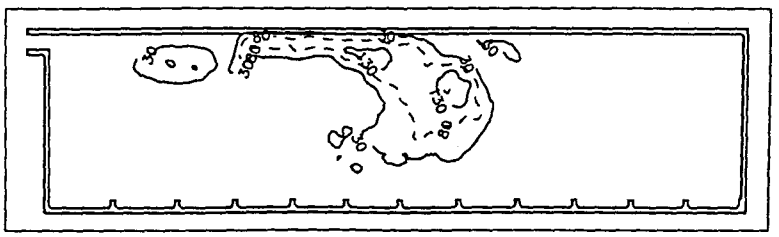

(*c*) 331 degrees

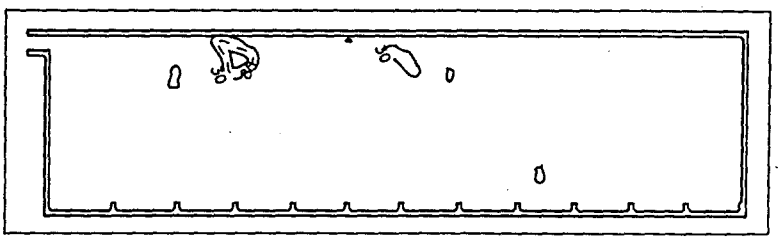

(*d*) 352 degrees

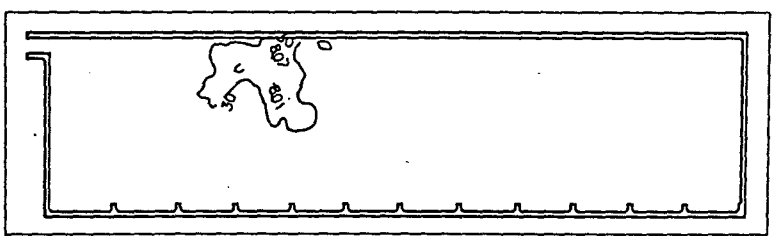

(*e*) 439 degrees

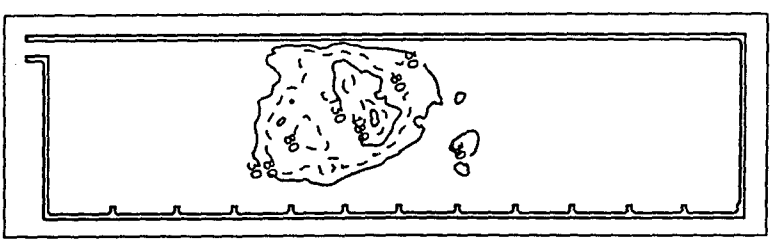

(*f*) 642 degrees

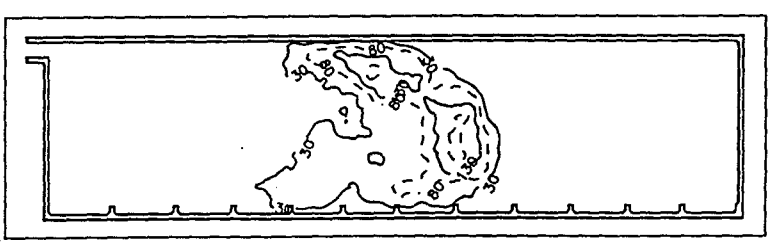

Figure 4.26(*a*) through (*f*): Contour plots of chemiluminescence images for chamber with expansion ratio of 12.0 at various phases in cycle.

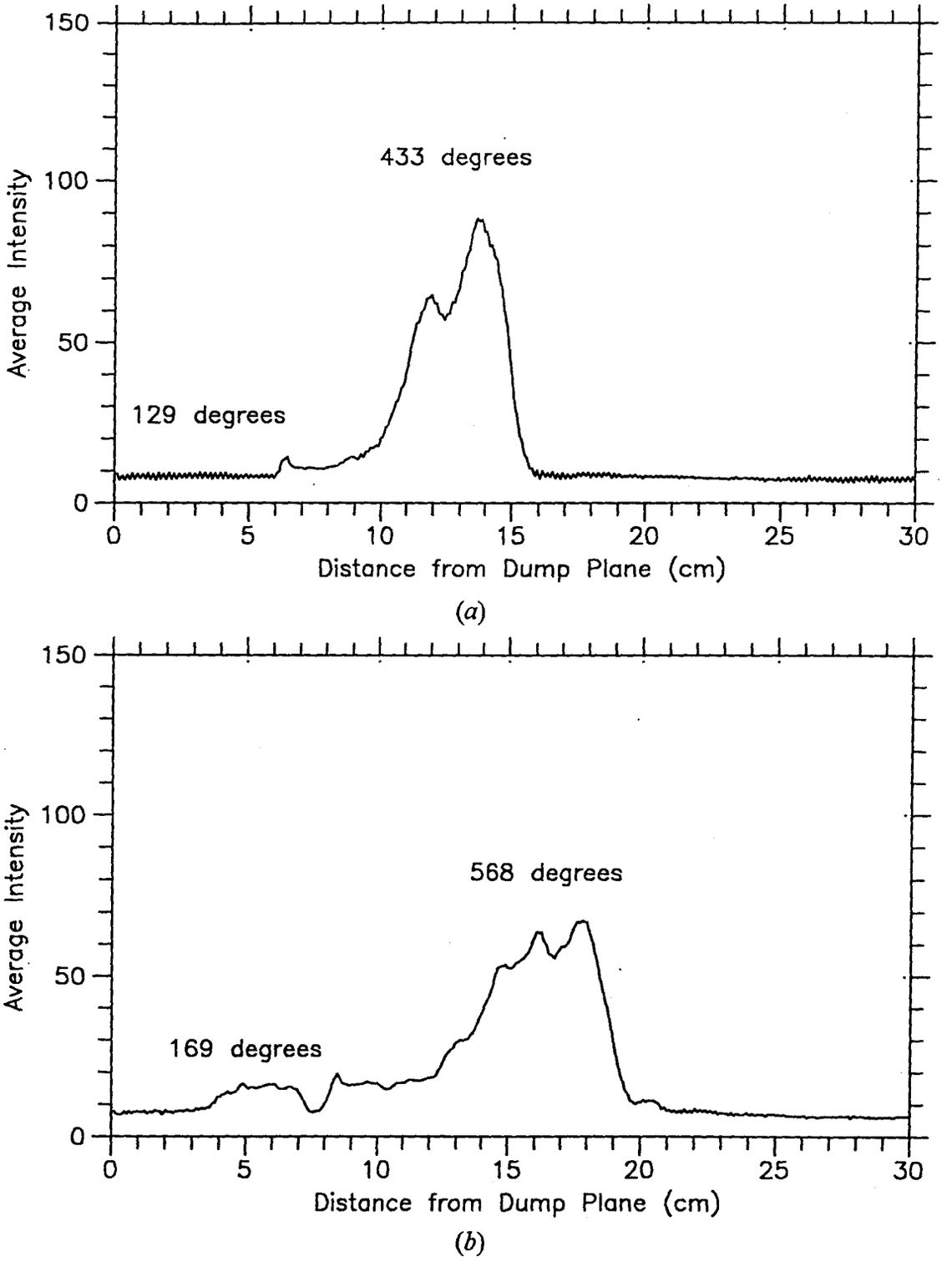

Figure 4.27(*a*) and (*b*): Average light intensity as a function of axial position for chamber with expansion ratio of 12.0 at various phases in cycle.

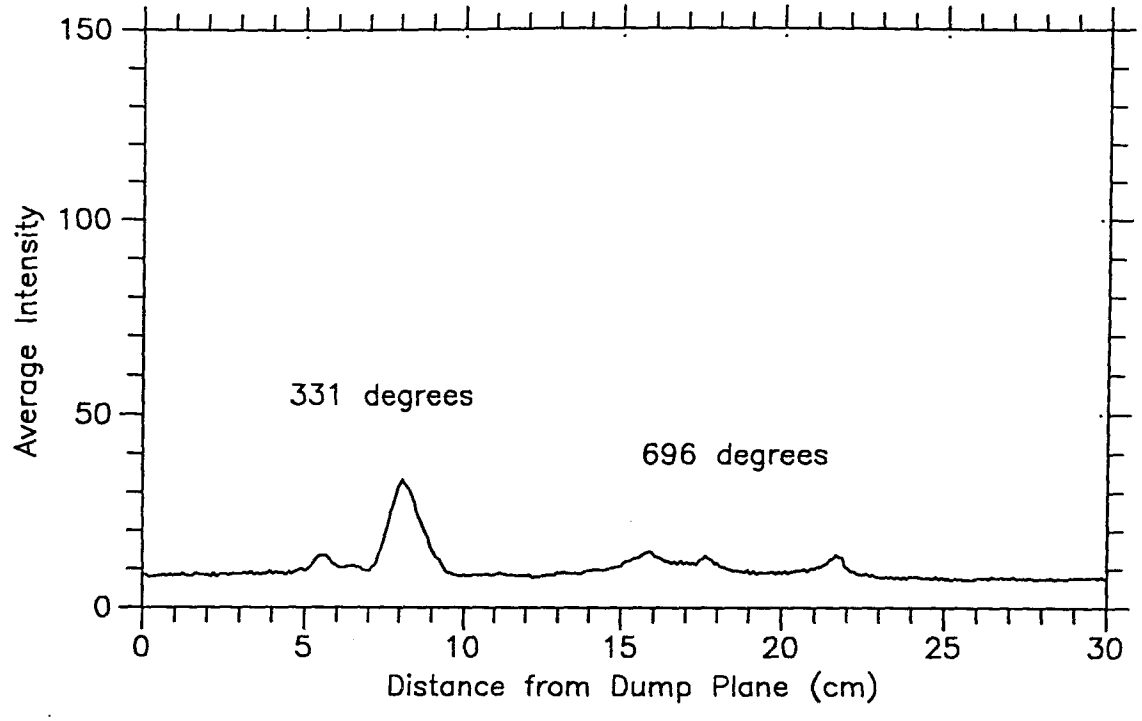

(*c*)

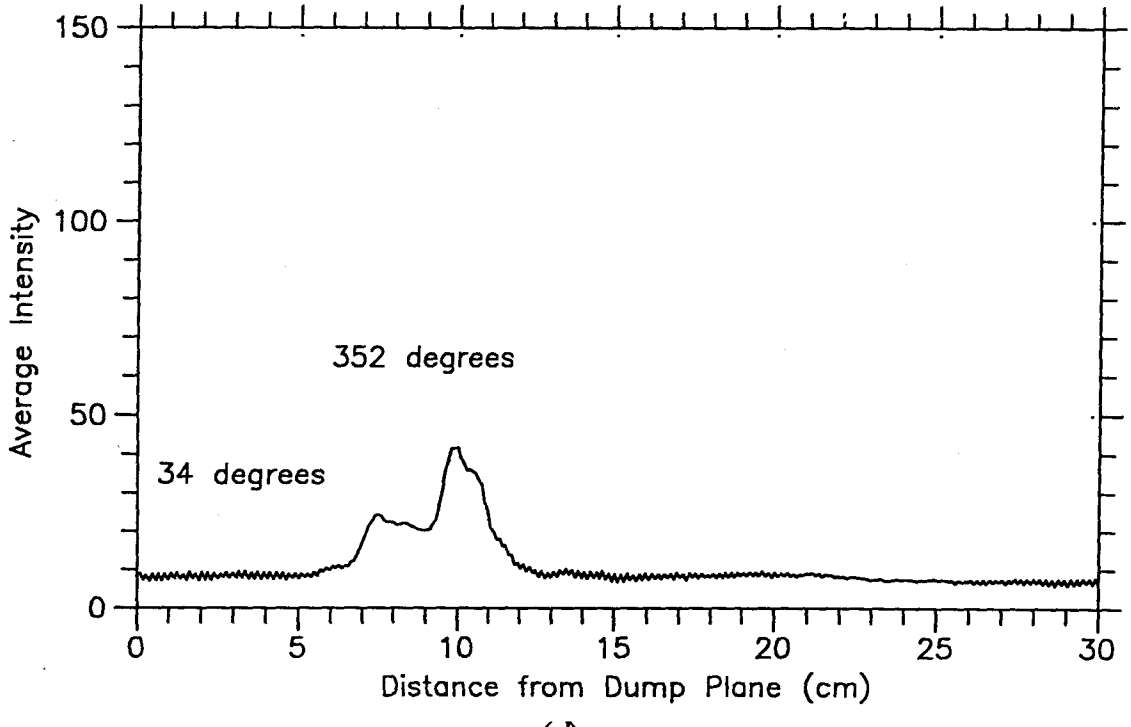

(*d*)

Figure 4.27(*c*) and (*d*): Average light intensity as a function of axial position for chamber with expansion ratio of 12.0 at various phases in cycle.

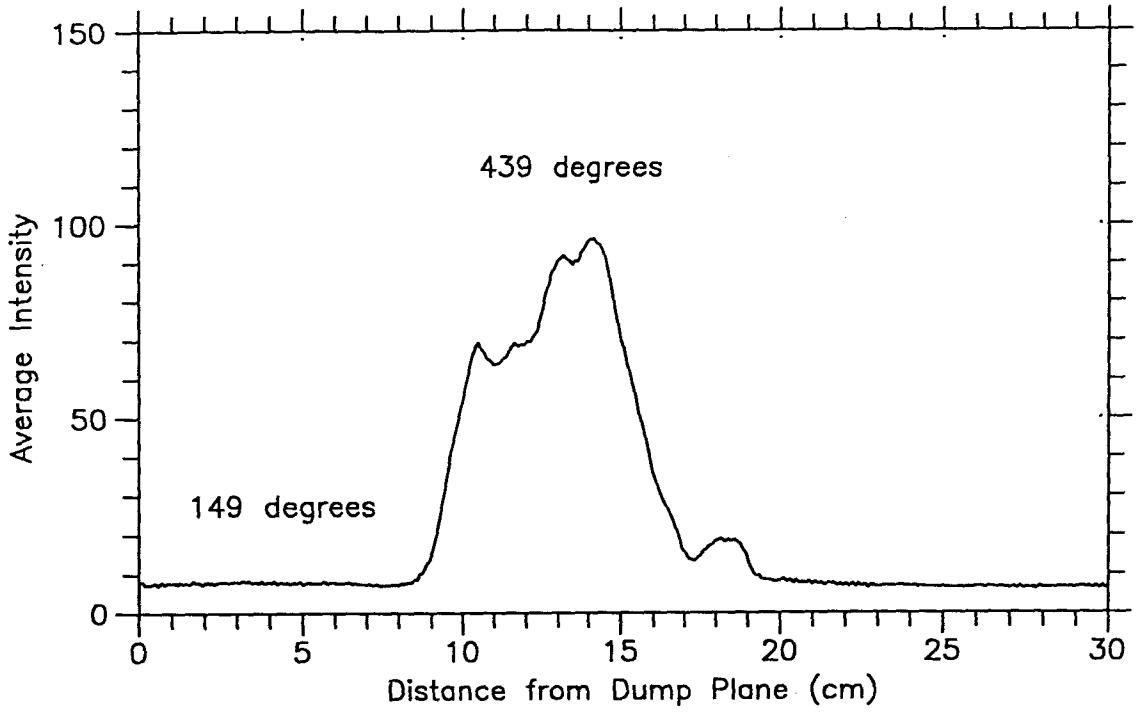

(*e*)

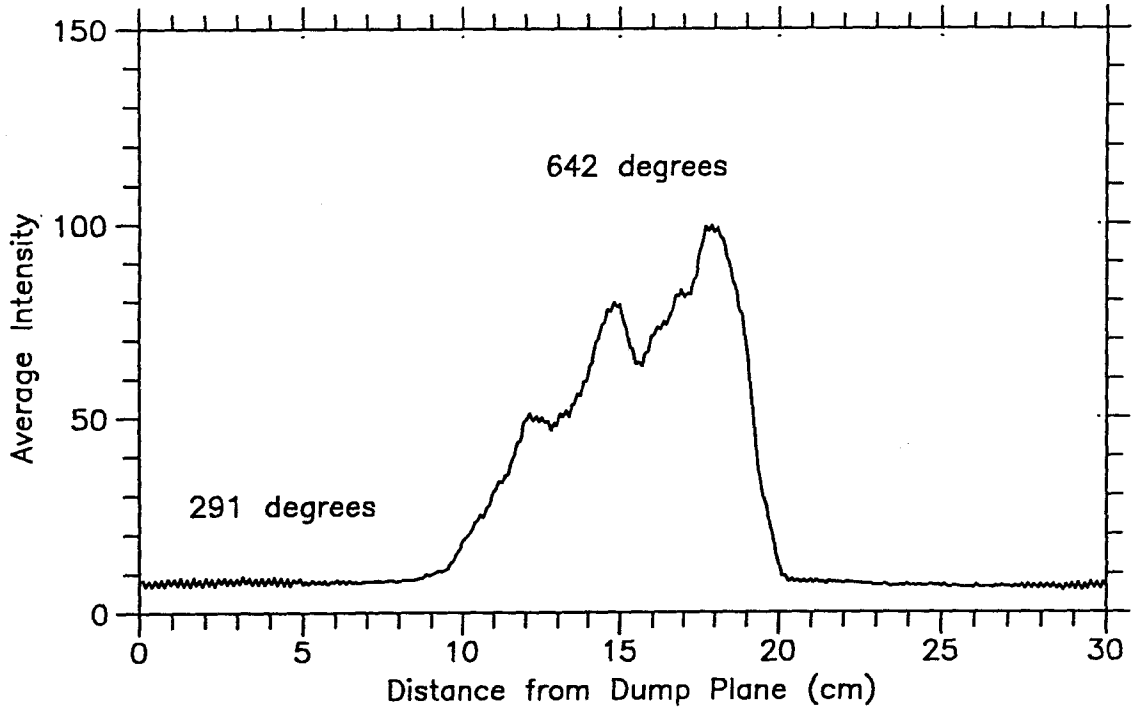

(*f*)

Figure 4.27(*e*) and (*f*): Average light intensity as a function of axial position for chamber with expansion ratio of 12.0 at various phases in cycle.

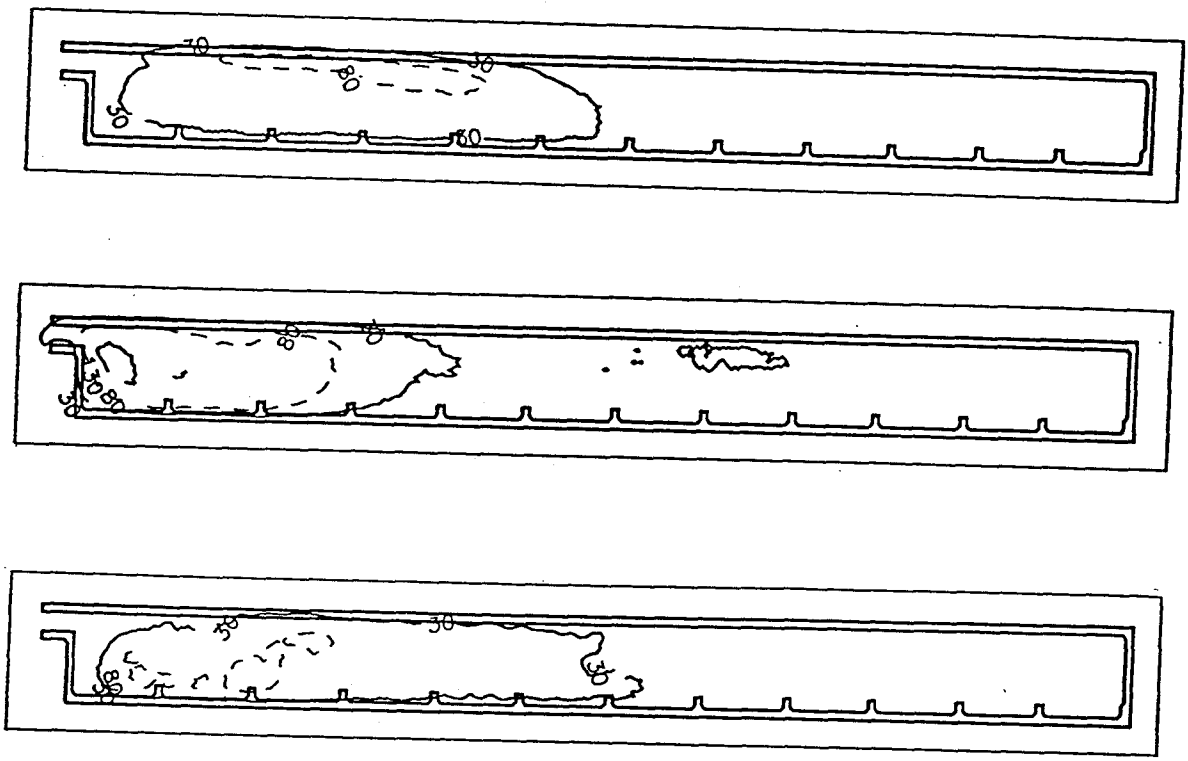

Figure 4.28: Contour plots of long-time exposure chemiluminescence images for chamber with expansion ratio of 4.0.

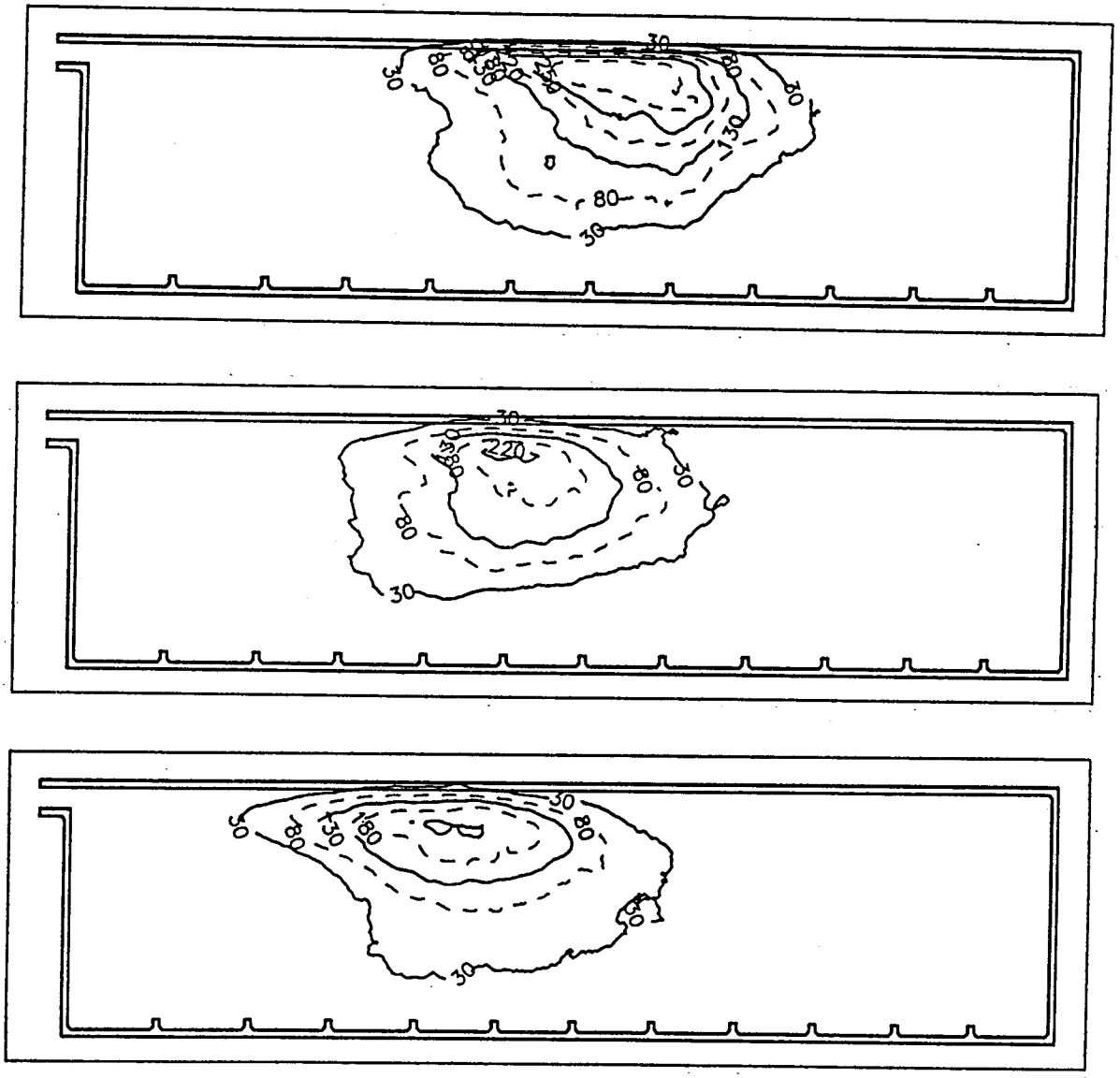

Figure 4.29: Contour plots of long-time exposure chemiluminescence images for chamber with expansion ratio of 12.0.

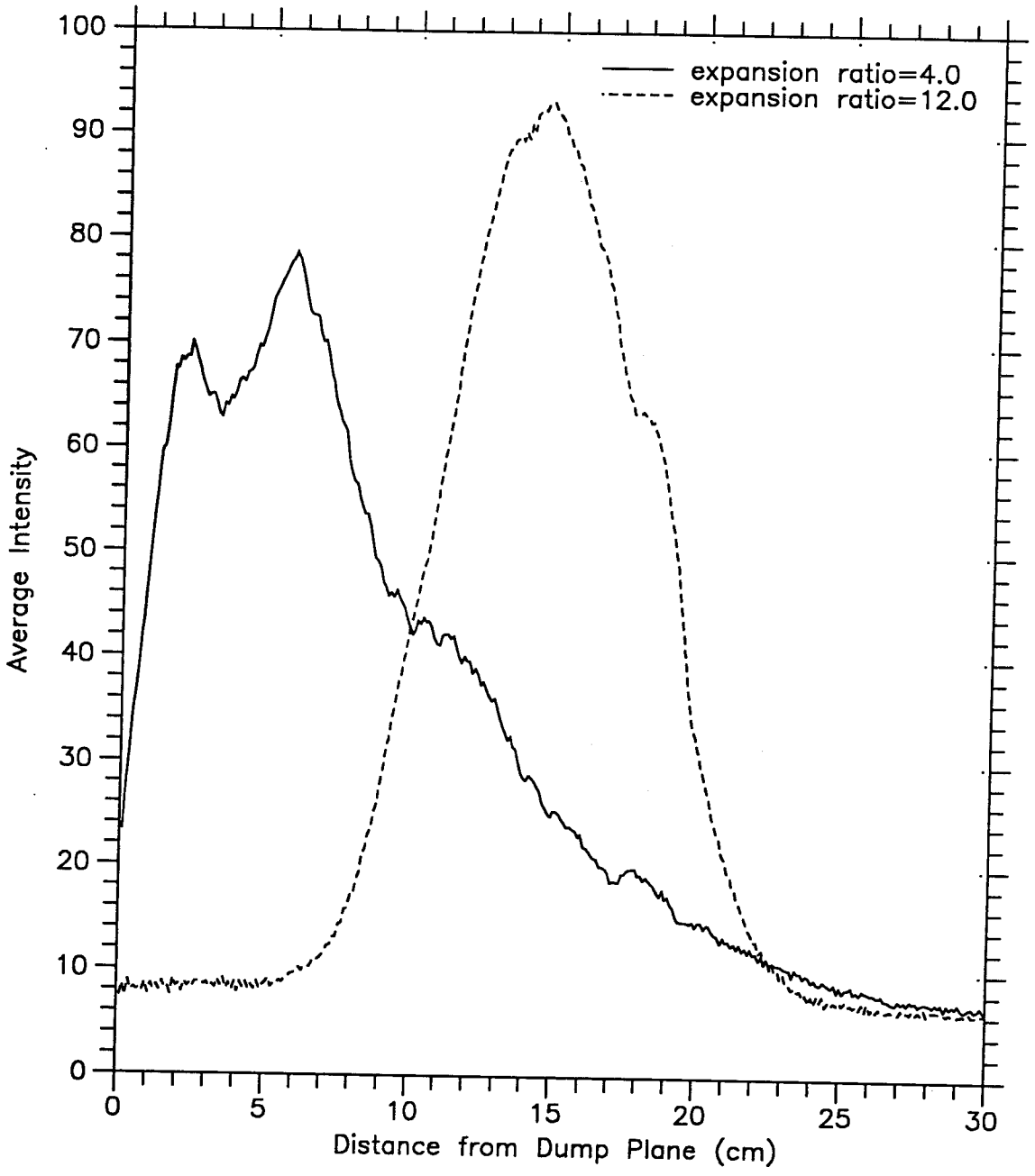

Figure 4.30: Average light intensity versus axial position for the long-time exposure chemiluminescence images for chambers with expansion ratios of 4.0 and 12.0.

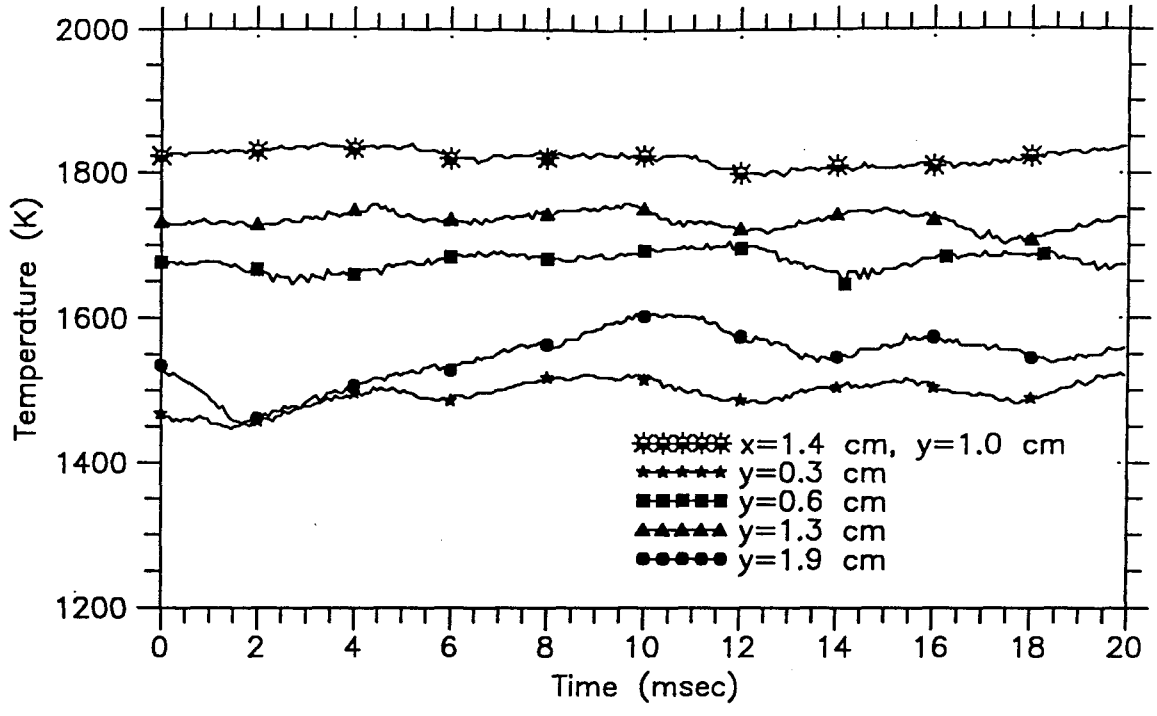

(*a*)

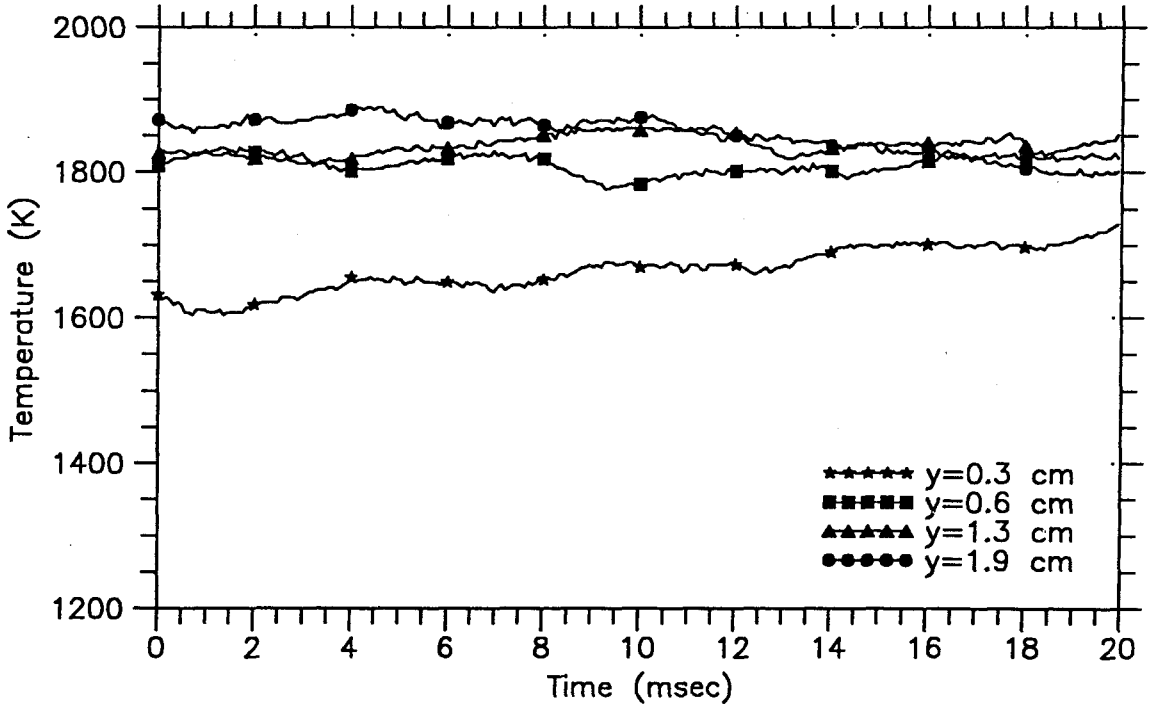

(*b*)

Figure 4.31: Temperature measurements at various elevations within chamber with expansion ratio of 4.0 at axial positions (*a*) 5 cm and (*b*) 10 cm downstream of dump plane.

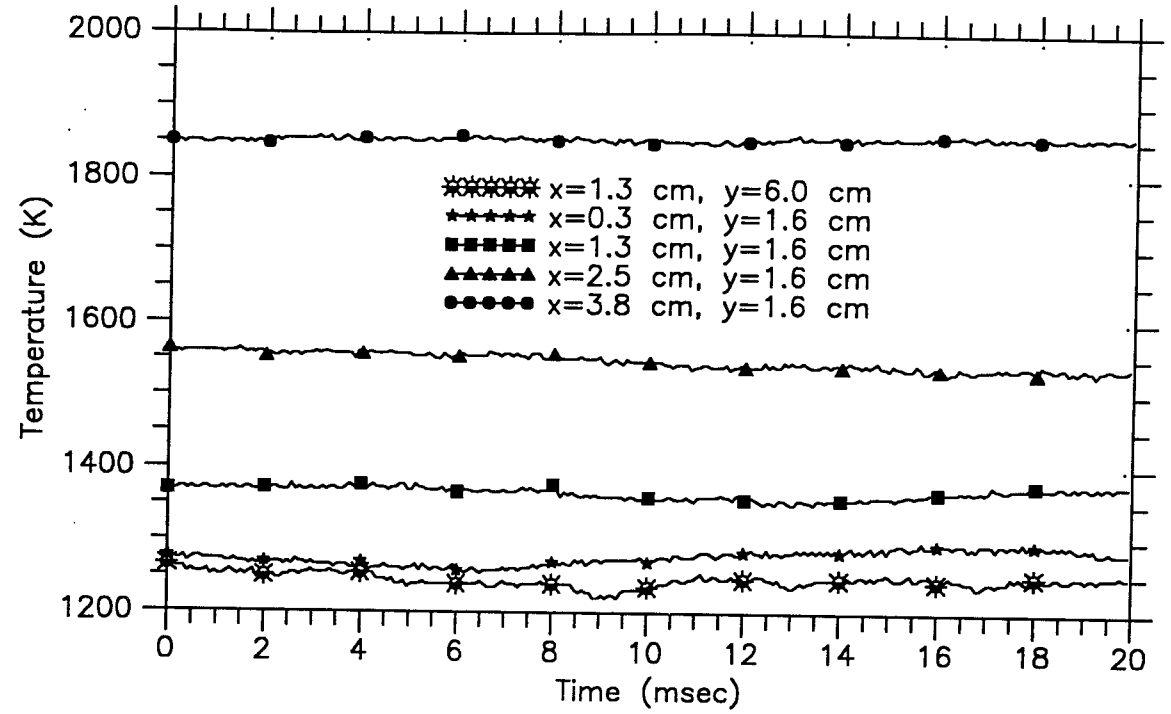

(*a*)

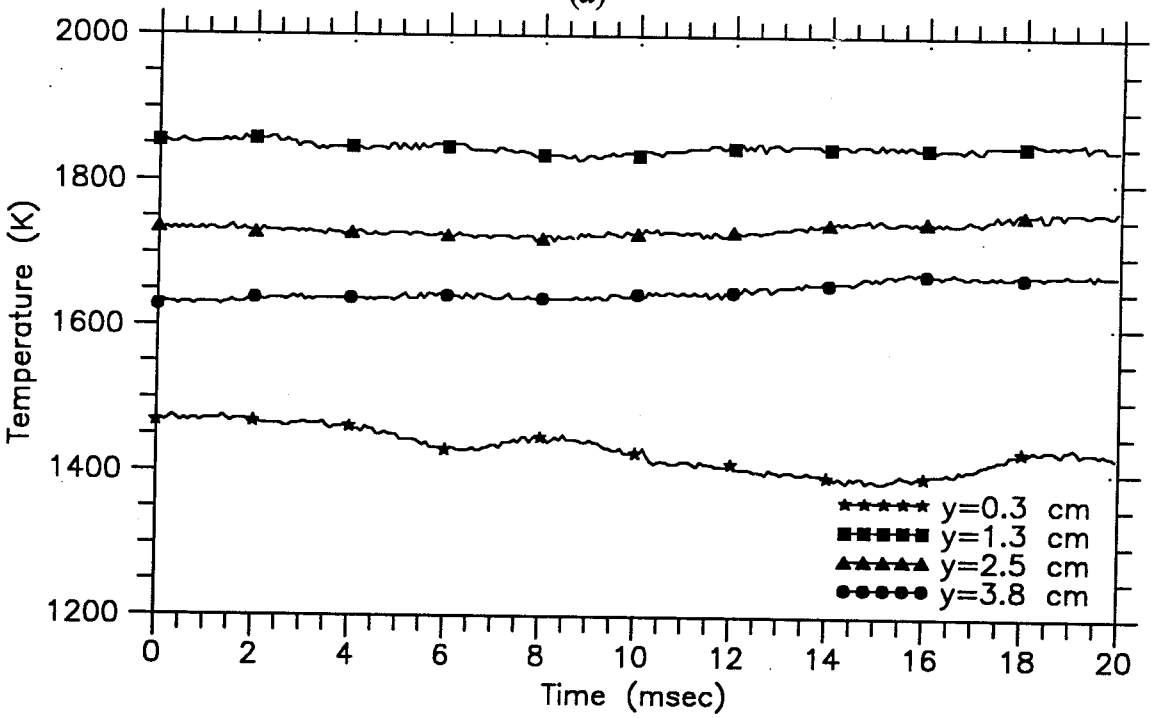

(*b*)

Figure 4.32(*a*) and (*b*): Temperature measurements at various elevations within chamber with expansion ratio of 12.0 at axial positions (*a*) near dump plane and (*b*) 5 cm downstream of dump plane.

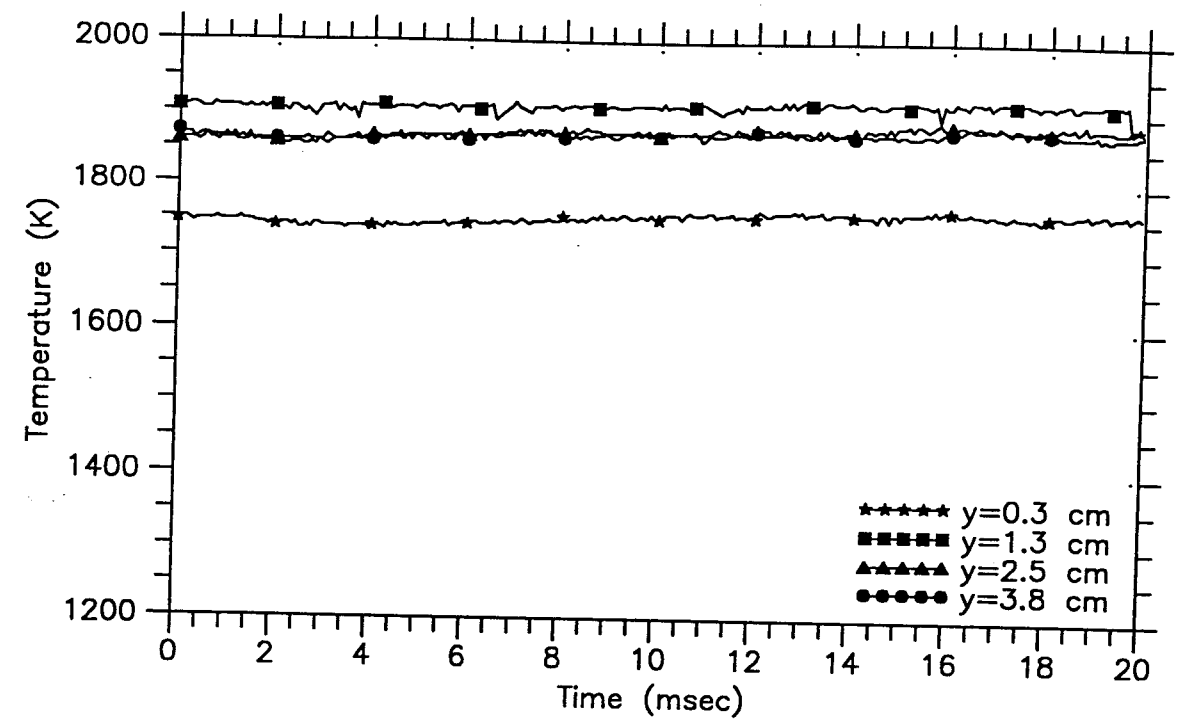

(*c*)

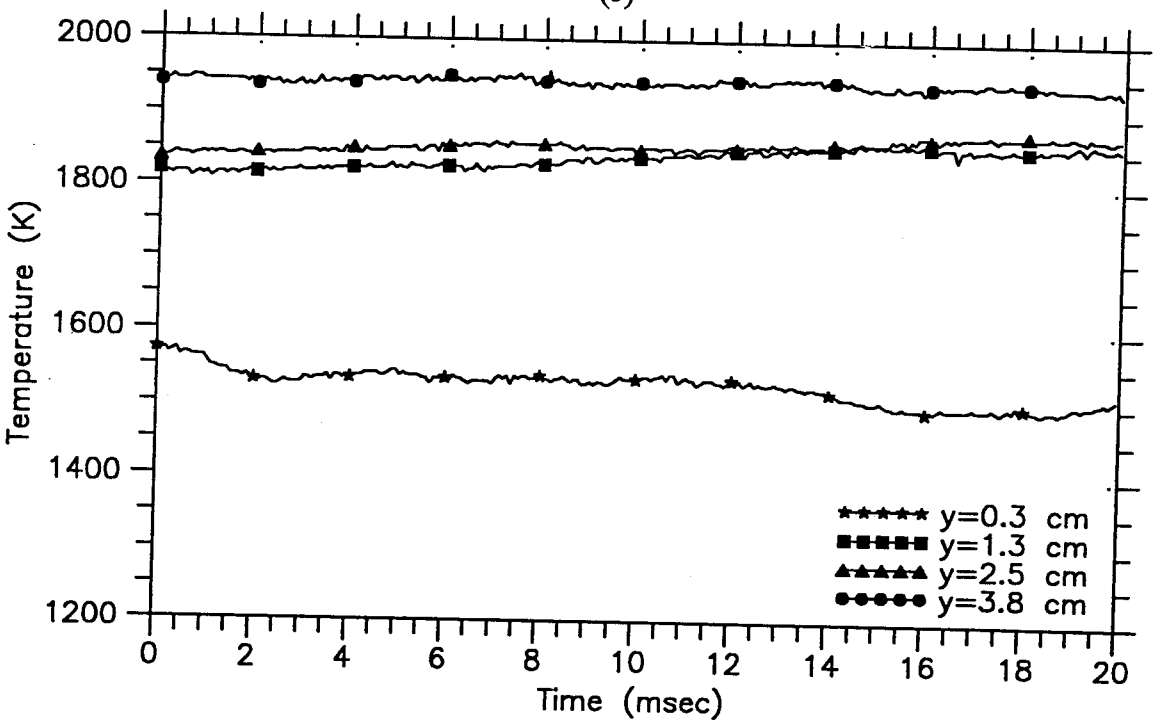

(*d*)

Figure 4.32(*c*) and (*d*): Temperature measurements at various elevations within chamber with expansion ratio of 12.0 at axial positions (*c*) 10 cm and (*d*) 15 cm downstream of dump plane.

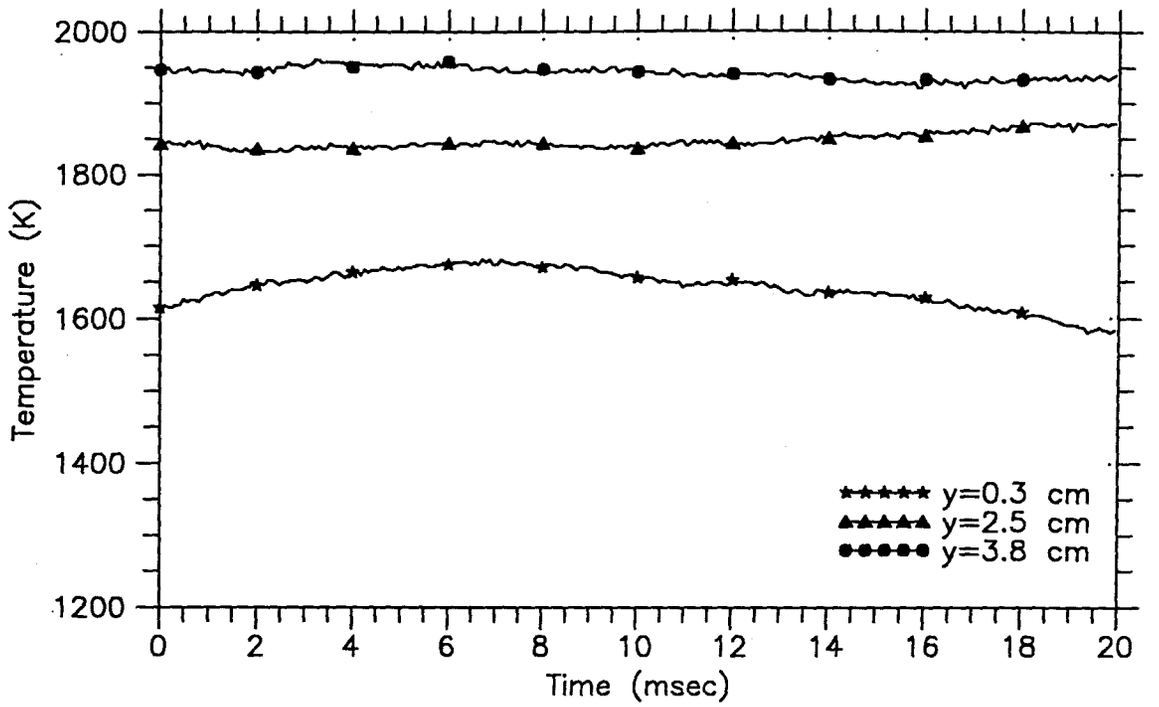

(*e*)

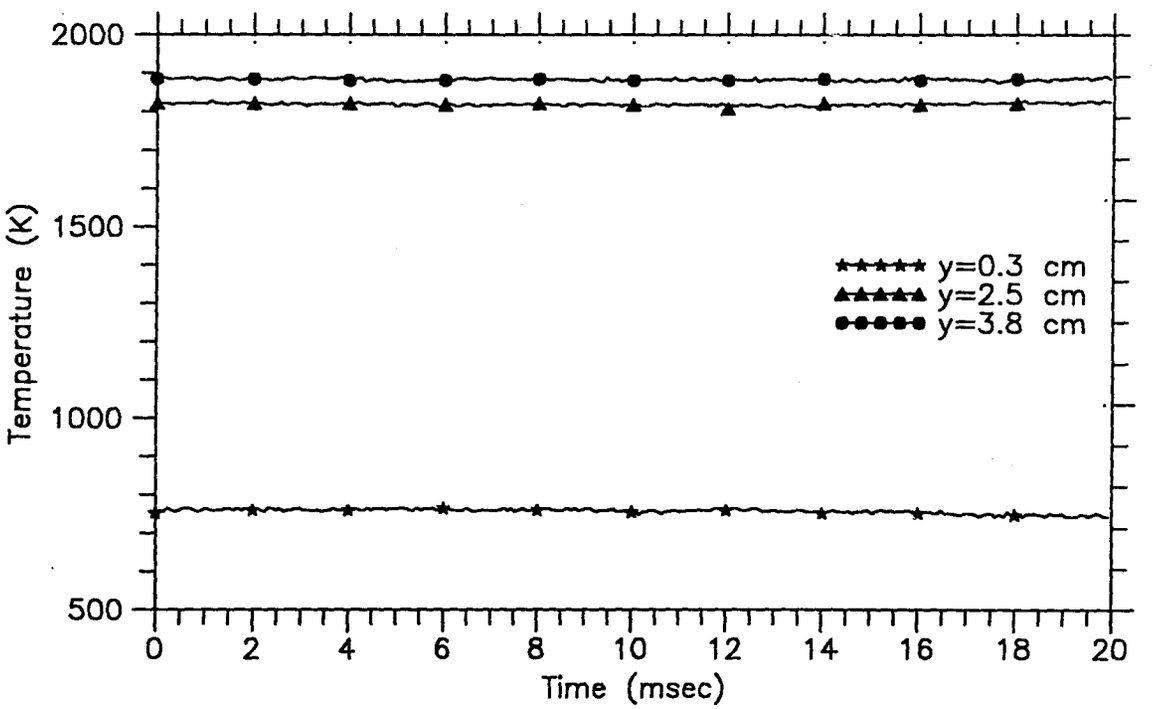

(*f*)

Figure 4.32(*e*) and (*f*): Temperature measurements at various elevations within chamber with expansion ratio of 12.0 at axial positions (*e*) 20 cm and (*f*) 25 cm downstream of dump plane.

Chapter Five
Concluding Remarks

An investigation of the reacting vortex structures associated with pulse combustion has been performed using a laboratory dump combustor in which vortices are shed from the lip of a rearward-facing step flame holder at frequencies equal to natural longitudinal acoustic modes of the system. A fuel-rich methane and air mixture is used as the premixed fuel for the study which focuses on the ignition and burning characteristics of the vortex structures for dump combustor expansion ratios of 4.0 and 12.0. The dump plane velocity in all cases is 21 m/sec. Several diagnostic techniques, such as ionization probes and chemiluminescence imaging using a solid-state intensified camera, are introduced to the experimental program, and the merits of planar acoustic wave theory are demonstrated in a simple model of the system. The results of the model will be discussed first.

One-dimensional linear acoustics is used to model the experimental apparatus and successfully predicts the resonant frequencies and corresponding mode shapes of the system for either combustor configuration. Within the model, the heat addition due to combustion is represented as an oscillatory volumetric mass source placed at any location along the length of the combustion chamber. The primary acoustic modes are tabulated in Table 5.1 for the two expansion ratios under cold- and hot-flow conditions.

Various temperatures within the combustion chamber are investigated within the model, and it is shown that the lowest acoustic mode for either of the hot-flow cases results from a migration of the lowest cold-flow acoustic mode to its higher hot-flow value. The two other hot-flow resonant frequencies arise from excitations of acoustic modes that are very sensitive to the conditions within the combustion chamber.

Table 5.1: Acoustic resonant modes for two combustion chamber expansion ratios.

EXPANSION RATIO = 4.0		EXPANSION RATIO = 12.0	
COLD-FLOW	**HOT-FLOW**	**COLD-FLOW**	**HOT-FLOW**
123 Hz	185 Hz	110 Hz	190 Hz
249 Hz	222 Hz	258 Hz	222 Hz
334 Hz	294 Hz	316 Hz	278 Hz
507 Hz		501 Hz	

The location of the mass source in the duct was found to have very little effect on the values of the resonant acoustic modes. It is also demonstrated that a distributed heat source can be modeled as the sum of a number of compact mass sources.

The true test of the acoustic model is how well it predicts the pressure amplitude spectra of the two chamber configurations. As long as a known heat release amplitude spectrum is used as the driving for the system, there is remarkable accuracy in the relative responses of the combustor pressure at the frequencies of interest as compared to the experimentally determined values. It is found that as the expansion ratio increases, the relative strength of the 'organ pipe mode' of the combustion chamber increases as well so that a beating exists between the lower, 'plenum chamber mode' and this 'organ pipe mode' of the combustor. There is little doubt that one-dimensional acoustics is a viable alternative to more elaborate computational schemes used for the prediction of dump combustor characteristics for different expansion ratios.

The experimental program is designed to provide insight into the controlling physical and chemical processes present during the burning of vortex structures associated with combustion instabilities. Any experimental data regarding the histories of the vortices from the moment that they are shed from the rearward-facing step to the time that

they burn themselves out would be beneficial to an analytical program attempting to reproduce the reacting flow. Several questions need to be addressed. These include:

1. How does the flow field change as the expansion ratio is increased?
2. How do the shadowgraph images relate to the actual combustion taking place?
3. Do the vortex structures ignite in the same manner for different combustor configurations?
4. Does the distribution of heat release throughout the chamber change as the expansion ratio changes?
5. How important is the presence of the lower wall?

The first question is answered with the aid of high-speed motion picture shadowgraphy. It is revealed that, as one would expect, the greater the expansion, the greater the opportunity for the shed structures to grow and develop as they progress down the length of the combustion chamber. The vortices are in fact formed at minimum velocity over the flame holder, and grow in a linear manner with time provided they are unobstructed by the lower wall of the combustion chamber.

The introduction of ionization probes to the experimental program provides a convenient and simple method of tracking the combustion activity within the combustor. Quenching of the combustion by the water-cooled walls is observed, and it is determined that the fine-scale structure present in the shadowgraph images is indicative of combustion activity and not merely residual combustion remaining on the sides of the duct. Perhaps the most important contribution to the program by the ionization probes is the agreement between the highly localized data of the ionization probes with the line-of-sight integrations of the chemiluminescence by the photomultiplier tube supporting the assumption of the existence of two-dimensional flow within the combustion chamber.

The answers to the third and fourth questions above are provided by the data acquired by the intensified camera. The camera is the single most important diagnostic tool that is added to the study of the reacting vortex structures, for it enables the experimenter to capture very short exposure images of the chemiluminescence occurring

as a result of the burning of the structures. These images show that both the ignition of the vortices and the distribution of heat within the combustion chamber are vastly different for the dump combustor expansion ratios examined.

Combustion activity is concentrated in the vicinity of the dump plane and even propagates upstream of the lip of the flame holder for the smaller expansion ratio configuration. The combustion which moves upstream of the dump plane provides a source of ignition for the premixed vortex structures forming at the step. The lower wall, being in close proximity to the lip of the rearward-facing step flame holder for the smaller depth chamber, is impinged upon by the shed structure just a few centimeters downstream of the dump plane. The collision and subsequent vigorous mixing of fresh reactants with hot combustion products leads to a burst in the heat release that is distributed over the first 20 cm to 30 cm of the chamber with the most intense combustion occurring between the dump plane and the point of impact of the shed vortex with the floor of the chamber.

The analysis of the images obtained by the intensified camera of the visible radiation emitted by the reacting vortex structures of the chamber having an expansion ratio of 12.0 shows that there exists a lack of combustion activity in the immediate vicinity of the dump plane. That is, there is very little, if any, upstream propagation of the flame beyond the edge of the flame holder. Ignition of the vortices is seen to take place approximately 5 cm to 8 cm downstream of the dump plane, and their primary source of ignition is the residual combustion of the previous burning vortex which lingers along the ceiling of the duct. Intense burning of the shed structure does not take place until the vortex has been in the chamber for roughly a length of time 50% longer than the period of its shedding frequency. This combustion is unaided by a collision with the lower wall of the chamber. The collision with the lower wall does enhance the combustion process for the smaller depth combustor. Finally, temperature measurements reveal that the recirculation zone of the larger duct is at a much lower temperature than its counterpart of the smaller depth chamber by several hundred degrees kelvin.

The study shows that the lower wall of the combustion chamber exerts a great deal of influence on the burning of the shed vortex structures when the expansion ratio of the dump combustor is 4.0 and negligibly affects the combustion for an expansion ratio of 12.0 because the floor is just too far below the lip of the step flame holder. Experiments not reported here show that when the expansion ratio is equal to 8.0, the vortices impinge upon the lower wall in much the same manner as in the case of the smaller expansion ratio of 4.0. Ignition and subsequent burning of the structures, therefore, are nearly the same as for the 4.0 expansion case. When the expansion ratio is greater than 12.0, one expects the same ignition and burning characteristics as for the 12.0 expansion ratio case, and experiments performed for an expansion ratio of 16.0 bear that out. Changing the fuel type to mixtures of 15% hydrogen or 30% hydrogen in methane merely resulted in a greater excitation of the highest acoustic mode of the system at a frequency near 280 Hz. The plenum and combustor modes are still dominant, however.

The material presented in this investigation will prove beneficial to the concurrent computational program, for a unique data base has been acquired regarding the reacting vortex structures associated with pulse combustion. Modelers are now able to compare their analytical results with those obtained experimentally in the laboratory dump combustor.

REFERENCES

Abouseif G., Keklak, J.A. & Toong, T. 1984 Ramjet Rumble: The Low-Frequency Instability Mechanism in Coaxial Dump Combustors. *Combustion Science and Technology* **36**, 83-108.

Barr, P.K. & Keller, J.O. 1991 Pulse Combustion: The Importance of Flame Extinction by Fluid Dynamic Strain. *Proceedings of the International Symposium on Pulsating Combustion* **1**, August 1991, Paper D-5.

Bee'r, J.M. & Chigier, N.A. 1983 *Combustion Aerodynamics*, Krieger Publishing Company, Malabar, FL, 1983.

Bradley, D. & Matthews, K.J. 1968 Measurement of High Gas Temperatures with Fine Wire Thermocouples. *Journal of Mechanical Engineering Science* **10**, 299-305.

Bulewicz, E.M. 1967 Some Observations on Chemiluminescence and Chemiionization in Flames. *Combustion and Flame* **11**, 297-308.

Calcote, H.F. 1963 Ion and Electron Profiles in Flames. *Ninth Symposium (International) on Combustion.* The Combustion Institute, Pittsburgh, PA, 1963, 184-189.

Carbon, M.W., Kutsch, H.J. & Hawkins, G.A. 1950 The Response of Thermocouples to Rapid Gas-Temperature Changes. *Transactions of the ASME* **July 1950**, 655-657.

Chomiak, J. 1972 Application of Chemiluminescence Measurement to the Study of Turbulent Flame Structure. *Combustion and Flame* **18**, 429-433.

Chomiak, J. 1990 *Combustion: A Study in Theory, Fact and Applications.* Abacus Press/Gordon and Breach Science Publishers, New York City, 1990.

Clark, T.P. & Bittker, D.A. 1954 A Study of the Radiation from Laminar and Turbulent Open Propane-Air Flames as a Function of Flame Area, Equivalence Ratio, and Fuel Flow Rate. *NACA Research Memorandum*, RM E54F29.

Currie, I.G. 1974 *Fundamental Mechanics of Fluids.* McGraw-Hill Publishing Company, New York City, 1974.

Diederichsen, J. & Gould, R.D. 1965 Combustion Instability: Radiation from Premixed Flames of Variable Burning Velocity. *Combustion and Flame* **9**, 25-31.

Ganji, A.T. & Sawyer, R.F. 1980 Turbulence, Combustion, Pollutant, and Stability Characterization of a Premixed, Step Combustor. *NASA Contractor Report Number 3230.*

General Electric Company, 1983 *Solid State CID Surveillance Camera User's Manual.*

Hegde, U.G., Ross, H.D. & Facca, L.T. 1991 Longitudinal Mode Instabilities of Particle Cloud Combustors in a Low Gravity Environment. *Proceedings of the International Symposium on Pulsating Combustion* **1**, August 1991, Paper D-2.

Hendricks, G.J., 1986 Two Mechanisms of Vorticity Generation in Combusting Flow Fields. *Ph.D. Thesis*, Daniel and Florence Guggenheim Jet Propulsion Center, California Institute of Technology, Pasadena, CA.

John, R.B. & Summerfield, M. 1957 Effect of Turbulence on Radiation Intensity from Propane-Air Flames. *Jet Propulsion* **27**, 169-179.

Karlovitz, B., Denniston, D.W., Knapschaefer, D. & Wells, F. 1953 Studies on Turbulent Flames. *Fourth Symposium (International) on Combustion*, The Williams and Wilkins Company, 1953, 613-619.

Keller, J.O., Bramlette, T.T., Westbrook, C.K. & Dec, J.E. 1990 Pulse Combustion: The Quantification of Characteristic Times. *Combustion and Flame* **79**, 151-161.

Keller, J.O. & Barr, P.K. 1991 Premixed Combustion in an Oscillating/Resonant Flow Field. An Investigation of the Fine-Scale Velocity Fluctuations. *Proceedings of the International Symposium on Pulsating Combustion* **1**, August 1991, Paper D-6.

Mahan, J.R., Cline, J.G. & Jones, J.D. 1984 A Temperature correlation for the radiation resistance of a thick-walled circular duct exhausting a hot gas. *Journal of the Acoustical Society of America* **75 (1)**, 63-71.

Rayleigh, J.W.S. 1878 *Nature* **18**, 319; also *The Theory of Sound*. Dover Publications, New York City **2**, 1945.

Rogers, D.E. & Marble, F.M. 1956 A Mechanism for High-Frequency Oscillation in Ramjet Combustors and Afterburners. *Jet Propulsion* **June 1956**, 456-462.

Samaniego, J. M., Yip, B., Poinsot, T. & Candel, S. 1991 Combustion Instabilities in a Side-Dump Model Ramjet Combustor. *Proceedings of the International Symposium on Pulsating Combustion* **1**, August 1991, Paper D-8.

Schadow, K.C., Gutmark, E., Parr, T.P., Parr, D.M.,Wilson, K.J. & Crump, J.E. 1989 Large-Scale Coherent Structures as Drivers of Combustion Instability. *Combustion Science and Technology* **64**,167-186.

Smith, D.A. 1985*a* An Experimental Study of Acoustically Excited, Vortex Driven, Combustion Instability within a Rearward Facing Step Combustor. *Ph.D. Thesis*, Daniel and Florence Guggenheim Jet Propulsion Center, California Institute of Technology, Pasadena, CA.

Smith, D.A. & Zukoski, E.E. 1985*b* *Combustion Instability Sustained by Unsteady Vortex Combustion.* AIAA/SAE/ASME/ASEE 21st Joint Propulsion Conference, 1985, AIAA-85-1248.

Smy, P.R. 1976 The Use of Langmuir Probes in the Study of High Pressure Plasmas. *Advances in Physics* **25**, 5, 517-553.

Sobota, T.H. 1987 An Experimental and Numerical Investigation of Swirling Flows in a Rectangular Nozzle. *Ph.D. Thesis*, Daniel and Florence Guggenheim Jet Propulsion Center, California Institute of Technology, Pasadena, CA.

Sterling, J.D. 1987*a* Longitudinal Mode Combustion Instabilities in Air Breathing Engines, *Ph.D. Thesis*, Daniel and Florence Guggenheim Jet Propulsion Center, California Institute of Technology, Pasadena, CA.

Sterling, J.D. & Zukoski, E.E. 1987*b* Longitudinal Mode Combustion Instabilities in a Dump Combustor. *AIAA 25th Aerospace Sciences Meeting*, January 1987, AIAA-87-0220.

Suzuki, T., Hirano, T. & Tsuji, H. 1979 Flame Front Movements of a Turbulent Premixed Flame. *Seventeenth Symposium (International) on Combustion*, The Combustion Institute, Pittsburgh, PA, 1979, 289-298.

Tang, J.M., Daniel, B.R., Jagoda, J.I. & Zinn, B.T. 1991 Interaction Between Flow Field and Flame Spread in a Helmholtz Type Pulse Combustor. *Proceedings of the International Symposium on Pulsating Combustion* **1**, August 1991, Paper D-4.

Travers, B. & Williams, H. 1965 The Use of Electrical Probes in Flame Plasmas. *Tenth Symposium (International) on Combustion*, The Combustion Institute, Pittsburgh, PA, 1965, 657-672.

Ventura, J.M.P. 1981 An Experimental Study of the Transition to Turbulence in Propane Flames. *Ph.D. Thesis*, University of Sheffield, Sheffield, England.

Willis, J.W., Lee, A.R., Karagozian, A.R. & Smith, O.I. 1991 Acoustic Mode Alteration in a Dump Combustor Arising from Halon Addition. *Proceedings of the International Symposium on Pulsating Combustion* **1**, August 1991, Paper B-1.

Zsak, T.W., Kendrick, D.W., Sterling, J.D. & Zukoski, E.E. 1991 An Investigation of Reacting Vortex Structures Associated with Pulse Combustion. *Proceedings of the International Symposium on Pulsating Combustion* **1**, August 1991, Paper D-7.